UTS UNIVERSITY OF TECHNOLOGY SYDNEY

Metal Organic Framework-Derived Transition Metal-Based Catalysts for Electrochemical Water splitting and Carbon Dioxide Reduction

by Minghong Huang

Thesis submitted in fulfilment of the requirements for the degree of

Doctor of Philosophy

under the supervision of Prof Zhenguo Huang and Prof John Zhou

University of Technology Sydney
Faculty of Engineering and Information Technology

August 2023

CERTIFICATE OF ORIGINAL AUTHORSHIP

I, Minghong Huang, declare that this thesis is submitted in fulfilment of the requirements for the award of Doctor of Philosophy, in the School of Civil and Environmental Engineering, Faculty of Engineering and Information Technology at the University of Technology Sydney.

This thesis is wholly my own work unless otherwise referenced or acknowledged. In addition, I certify that all information sources and literature used are indicated in the thesis.

This document has not been submitted for qualifications at any other academic institution.

This research is supported by the Australian Government Research Training Program.

Signature:

Production Note:
Signature removed prior to publication.

Date:

11/08/2023

Acknowledgement

Firstly, I would like to express my deepest acknowledgment to my principal supervisor Prof. Zhenguo Huang, for his unreserved support during my Ph.D. study. I am unable to accomplish my Ph.D. study without his guidance for my research.

Secondly, I deeply appreciate Prof. Qi-Long Zhu as the host during my visit in Fujian Institute of Research on the Structure of Matter, Chinese Academy of Sciences. Without his great support in laboratory and equipment, I can hardly accomplish my Ph.D. study during Covid. I thank him for his invaluable advice.

I would like to extend my sincere thanks to the kind support from my research collaborators: Dr. Daniel Morrison, for his help in my early research work; Prof. John Zhou, for his input on research and candidacy assessment along the way.

I appreciate all the assistance and support from my lab colleagues, Lei Ding, Guojin Zhang, Yan Dai, Xuefei Wang, Feng Liu, Rui Han, Zhimei Xu, Dr. Changsheng Cao, Dr. Dongdong Ma, Dr. Xiaofang Li, Wenbo Wei, Shenghua Zhou, Maoyin Ran, Dr. Min Zhang, Dr. Chengbin Hong, Qing Li, Liu Li, Yingchun He, and Lei Jiao (in no particular order).

Finally, I must express the deepest gratitude for the support and love from my family and friends, including my parents Mr. S-H. Huang and Ms. H-X. Chen, my sister Ms. L-Z. Huang and L-F. Huang, my brother R-M. Huang, J-L. Huang, J-H. Huang and J-M. Huang, as well as my friend Y-X. Lu. Their selfless love is always my powerful backing. Without their unwavering understanding, support, and encouragement, I would not have been able to achieve my goals during my doctoral work.

Table of contents

CERTIFICATE OF ORIGINAL AUTHORSHIP ..... **i**

Acknowledgement ..... **ii**

Table of contents ..... **iii**

Research Publications ..... **vi**

List of Tables ..... **vii**

List of Figures ..... **viii**

List of Abbreviations and Notations ..... **xvii**

Abstract ..... **xx**

CHAPTER 1 Introduction **1**

1.1. Research background 1

1.2. Research objectives 2

1.3. Research significance 3

1.4. Arrangement of the thesis 3

CHAPTER 2 Literature Review **6**

2.1. Electrocatalysis 6

2.1.1. Oxygen evolution reaction 8

2.1.2. Hydrogen evolution reaction 18

2.1.3. Overall water splitting 20

2.2. Electrochemical CO_2 reduction 22

2.2.1. The fundamentals of CO_2 electroreduction 22

2.2.2. MOF-derived electrocatalysts for CO_2RR to CO 26

2.3. Summary and gap identification 31

2.4. Aims and objectives 32

CHAPTER 3 Experimental details **33**

3.1. Chemicals 33

3.2. Catalyst preparation 34

3.3. Materials characterization 34

X-ray diffraction 34
Scanning electron microscopy 34
Transmission electron microscopy 35
Raman spectroscopy 35
N_2 sorption-desorption measurement 35
Fourier transform infrared spectroscopy (FTIR) 35
Nuclear magnetic resonance (NMR) spectroscopy 36
Gas chromatography 36
3.4. Electrochemical studies 36
3.4.1. Preparation of the working electrode 36
3.4.2. Cyclic voltammetry 37
3.4.3. Linear sweep voltammetry 37
3.4.4. Other measurements 37
3.4.5. Computational details 38

CHAPTER 4 MOF-Derived Hollow and Yolk-Shell Nanocages for Water Oxidation and Selective Ethylene Glycol Reformation 39

4.1. Introduction 39
4.2. Experimental section 42
4.2.1. Catalyst synthesis 42
4.3. Results and discussion 43
4.4. Conclusion 71

CHAPTER 5 MoC-Fe Heterojunctions Encapsulated in N-doped Carbon Nanotubes for Water Splitting 72

5.1. Introduction 72
5.2. Experimental section 75
5.2.1. Catalyst synthesis 75
5.3. Results and discussion 76
5.4. Conclusion 95

CHAPTER 6 Iron-Selenium Dual-Single-Atom Electrocatalysts for CO_2 Reduction 97

6.1. Introduction 97
6.2. Experimental section 99

6.2.1. Catalyst synthesis 99
6.2.2. Electrochemical measurement 100
6.2.3. Rechargeable Zn-CO_2 battery measurement 101
6.3. Results and discussion 101
6.4. Conclusion 118

CHAPTER 7 Conclusions and outlooks 120

7.1. Conclusion 120
7.2. Outlooks 122

References 124

Research Publications

Publication included in this thesis

M. Huang, C. Cao, L. Liu, W. Wei, Q. -L. Zhu, Z. Huang, "Controlled synthesis of MOF-derived hollow and yolk–shell nanocages for improved water oxidation and selective ethylene glycol reformation", *eScience*, 2023, 100118.

M. Huang, S. Zhou, D. Ma, W. Wei, Q. -L. Zhu, Z. Huang, "MOF-Derived MoC-Fe Heterojunctions Encapsulated in N-doped Carbon Nanotubes for Water Splitting", *Chemical Engineering Journal*, 2023, 145170.

Other publication during the candidature

Han, R., Liu, F., Wang, X., **Huang, M.**, Li, W., Yamauchi, Y., ... & Huang, Z. (2020). Functionalised hexagonal boron nitride for energy conversion and storage. *Journal of Materials Chemistry A*, *8*(29), 14384-14399.

List of Tables

Table 2.1. Reaction pathways for different products of electrochemical CO_2 reduction [62]. 24

Table 3.1 Reagents used in the experiments. 33

Table 4.1. Comparison of the OER performance of h-CoFe-LDH NCs and other Co-based electrocatalysts reported. 59

Table 4.2. Performance comparison of overall water splitting (HER||OER) and hybrid electrolysis coupled with small organic molecule oxidation reactions in recent reports and this work. 70

Table 5.1. Comparison of OER and HER activities in 1.0 M KOH between MoC-Fe@NCNTs and reported MoC_x-based electrocatalysts. 89

Table 5.2. Comparison of the bifunctional water-splitting activity in 1.0 M KOH between MoC-Fe@NCNTs and other electrocatalysts. 92

Table 6.1. Content of elements in the as-synthesized samples obtained from ICP-OES. 109

Table 6.2. Comparison of the electrocatalytic CO_2RR performance in H-type cell of FeSe-NC with other carbon-based single-atom electrocatalysts. 115

List of Figures

Figure 2.1. Schematics of a sustainable energy future of electrochemical conversion [1]. 6

Figure 2.2. Schematics of the electrochemical alkaline water splitting. 7

Figure 2.3. The OER mechanism in alkaline medium. 8

Figure 2.4. Preparation and characterization of M-MNS-1.0. (a) Schematic illustration of the 2D oxide sacrifice approach (2dOSA) for the conversion of M-ONS with H4dobdc ligand to form M-MNS. (b–g) TEM images of Co-MNS, Ni-MNS, Cu-MNS, FeCo-MNS, NiFe-MNS, and CoCu-MNS. (h) XRD patterns of the synthesized MOF-74 nanosheets. (i) OER polarization curves of FeCo-ONS, FeCo-MNS-1.0, FeCo-MB, and Co-MNS in 0.1 M KOH. (j) The C.N. for the Co-ligand and Fe-ligand of FeCo-MNS-1.0 and FeCo-MB. (k) OER curves of FeCo-MNS-1.0, FeCo-ONS, and RuO_2 loaded on Ni foam with a loading of 2.0 mg cm^{-2} in 0.1 M KOH. [15]. 10

Figure 2.5. Schematic illustration of the synthesis of NC@Co-NGC DSNCs. (a) *iR*-corrected OER polarization curves of NC, Co-NGC, NC@Co-NGC, Pt/C, and RuO_2 catalyst in O_2-saturated 0.1 M KOH solution and (b) Tafel plots of NC, Co-NGC, NC@Co-NGC, Pt/C, and RuO_2 catalyst[19]. 12

Figure 2.6. (a) Synthesis and OER performance of the a-NiCo/NC [21] and (b) Scheme for the synthesis, characterization and OER performance of CoNi-SAs/NC [22].). 14

Figure 2.7. (a) Schematic illustration of the synthesis of $Co_{0.85}Se_{1-x}$@C nanocages, (b) TEM image of ZIF-1h, (c) TEM image of ZIF-1h-550 and (d) OER LSV curves of ZIF-1h-550, ZIF-1h, and RuO_2 [32]. 15

Figure 2.8. (a) Schematic illustration depicting the conversion process of a core-shell ZIF NP into a shell-in-shell LDH nanocage [42], (b) illustration for the synthesis of Ru SAs/AC-FeCoNi, (c) AC HAADF-STEM image, (d) HAADF-STEM image and corresponding elemental mappings of Ru SAs/AC-FeCoNi, and (e) OER LSV curves of RuO_2, AC-FeCoNi, Ru SAs/AC-FeCoNi, and Ru SAs/C-FeCoNi [40]. 17

Figure 2.9. Scheme for the syntheses of (a) porous MoC_x nano-octahedra [49] and (b) MC-M_2C/PNCDs [52]..... 20

Figure 2.10. Scheme for the synthesis of CoP/NCNHP [56]. 21

Figure 2.11. Schematic illustration for the synthesis of Co/CoP@HOMC [57]. 22

Figure 2.12. A typical electrochemical CO_2 reduction system. 24

Figure 2.13. MOFs-derived SACs by different strategies. (a) co-crystallization, C-Zn_xNi_y ZIF-8 catalysts [77]; (b) ion exchange, Ni SAs/N-C catalyst [75]. (c) cage-confinement, InSAs/NC[73]; (d) atomic replacement, $(PtZn)_n/Ni_1$-CN [78]. 28

Figure 2.14. Illustration of atomic environment of DACs. 30

Figure 2.15. Schematic illustration of synthesis of InNi DS/NC. a) AC HAADF-STEM image of InNi DS/NC. Atomic-resolution EELS mapping of b) In, c) Ni and d) their overlap. e) EELS spectra extracted from the position highlighted in the yellow circle in (d), (inset: the enlarged image in the yellow circle in (d)). f) HAADF-STEM image and corresponding EDS mapping [89]. 31

Figure 4.1. Schematic illustration of the fabrication of h-CoFe-LDH NCs and ys-ZIF@CoFe-LDH NCs..... 43

Figure 4.2. (a) PXRD pattern and (b) A SEM image of ZIF-67 nanocrystals. 44

Figure 4.3. (a) PXRD patterns of h-CoFe-LDH NCs and typical CoFe-LDH NSs (t-CoFe-LDH NSs); SEM and TEM images of (b-d) h-CoFe-LDH NCs and (e, f) ys-

ZIF@CoFe-LDH NCs; HAADF-STEM and the corresponding EDS elemental mapping images of (g) h-CoFe-LDH NCs and (h) ys-ZIF@CoFe-LDH NCs. 45

Figure 4.4. PXRD patterns of ZIF-67 and ys-ZIF@CoFe-LDH NCs. 46

Figure 4.5. EDS analysis of h-CoFe-LDH NCs. Based on the EDS, the atomic ratio of Fe:Co in h-CoFe-LDH NCs is about 1: 7.15. 47

Figure 4.6. (a) A SEM image and (b) corresponding EDS analysis of t-CoFe-LDH NSs. Based on EDS, the atomic ratio of Fe:Co in t-CoFe-LDH NSs is about 1: 6.6, which is similar to that of h-CoFe-LDH NCs. 48

Figure 4.7. (a) PXRD pattern, (b) SEM, and (c-d) TEM images of h-Co-LDH NCs. ... 48

Figure 4.8. (a) N_2 sorption isotherms of ZIF-67, h-CoFe-LDH NC, ys-ZIF@CoFe-LDH NCs, t-CoFe-LDH NSs and h-Co-LDH NCs. (b) FTIR spectra of ZIF-67, h-CoFe-LDH NCs, ys-ZIF@CoFe-LDH NCs and $K_3[Fe(C_2O_4)_3]$. (c) Raman spectra of h-CoFe-LDH NCs and ys-CoFe-LDH NCs. High-resolution XPS spectra of (d) C 1s, (e) Co 2p, and (f) Fe 2p for h-CoFe-LDH NCs and t-CoFe-LDH NSs. 49

Figure 4.9. SEM images of the resultant CoFe-LDHs prepared by using different Fe salts as the reconstruction agents: (a-b) $FeCl_3 \cdot 6H_2O$, (c-d) $Fe(NO_3)_3 \cdot 9H_2O$ 50

Figure 4.10. SEM images of h-CoFe-LDH NCs prepared using $K_3[Fe(C_2O_4)_3]$ with different concentrations: (a) 0.5 mg mL^{-1}, (b) 1.0 mg mL^{-1}, (c) 1.5 mg mL^{-1}, and (d) 2.5 mg mL^{-1} 51

Figure 4.11. FTIR spectra of h-CoFe-LDH NCs, t-CoFe-LDH NSs and h-Co-LDH NCs. 52

Figure 4.12. Raman spectra of h-CoFe-LDH NCs, t-CoFe-LDH NSs, and h-Co-LDH NCs. 53

Figure 4.13. XPS survey spectra of h-CoFe-LDH NCs, ys-ZIF@CoFe-LDH NCs, t-CoFe-LDH NSs, and h-Co-LDH NCs. 54

Figure 4.14. High-resolution XPS spectra of Co 2p for h-CoFe-LDH NCs, ys-ZIF@CoFe-LDH NCs and h-Co-LDH NCs. 55

Figure 4.15. OER performance of the catalysts: (a) LSV curves, (b) the comparison of overpotential η at a current density j=50 mA cm^{-2} and the j at η=300 mV; (c) capacitive Δj ($=j_a - j_c$) against scan rates; (d) Tafel plots; (e) EIS plots; (f) long-term stability test for h-CoFe-LDH NCs at j=10 mA cm^{-2}. All the tests were conducted in 1.0 M KOH. Inset in (f) is the SEM image of h-CoFe-LDH NCs after the stability test. 57

Figure 4.16. CV curves of (a) h-CoFe-LDH NCs, (b) ys-ZIF@CoFe-LDH NCs and (c) h-Co-LDH NCs in 1.0 M KOH at increasing scan rates from 20 to 100 mV s^{-1}. Relationship between the anodic/cathodic current densities with (d-f) the scan rates and (g-i) the square root of the scan rates (red line: cathodic, black line: anodic). 58

Figure 4.17. CV curves of (a) h-CoFe-LDH NCs, (b) ys-ZIF@CoFe-LDH NCs, (c) t-CoFe-LDH NSs and (d) h-Co-LDH NCs at different scanning rates in 1.0 M KOH. 60

Figure 4.18. LSV curves normalized by electrochemically active surface areas (ECSAs). 61

Figure 4.19. TEM images of h-CoFe-LDH NCs after the OER test. 62

Figure 4.20. PXRD patterns of h-CoFe-LDH NCs before and after the long-term stability test. 63

Figure 4.21. Raman spectra of h-CoFe-LDH NCs before and after the long-term stability test. 63

Figure 4.22. (a) XPS survey, (b) Co 2p, (c) Fe 2p, and (d) O 1s spectra of h-CoFe-LDH NCs before and after the OER test. 64

Figure 4.23. (a-d) EGOR performance of the catalysts: (a) LSV curves; (b) ^{1}H NMR spectra of the electrolyte before and after electrolysis; (c) correlation between potential and $FE_{formate}$; (d) multi-step chronopotentiometry curves from 10 to 100 mA cm^{-2}; (e) the schematic illustration and (f) LSV curves of the HER||OER and HER||EGOR based on the Pt/C||ys-ZIF@CoFe-LDH NCs pair. 65

Figure 4.24. Correlation between current density and voltage as a function of time: (a) h-CoFe-LDH NCs, (b) ys-ZIF@CoFe-LDH NCs and (c) h-Co-LDH NCs in 1.0 M KOH with 0.5 M EG. 66

Figure 4.25. Potential-dependent $j_{formate}$ of h-CoFe-LDH NCs, ys-ZIF@CoFe-LDH NCs, and h-Co-LDH NCs. 67

Figure 4.26. Long-term stability test for h-CoFe-LDH NCs, ys-ZIF@CoFe-LDH NCs, and h-Co-LDH NCs at 50 mA cm^{-2} in 1.0 M KOH with 0.5 M EG. 67

Figure 4.27. HER performance of commercial 20% Pt/C in 1.0 M KOH with and without 0.5 M EG. 68

Figure 4.28. Polarization curves over the pairs of Pt/C||h-CoFe-LDH NCs, Pt/C||ys-ZIF@CoFe-LDH NCs, Pt/C||h-Co-LDH NCs and Pt/C||RuO_2 in 1.0 M KOH with 0.5 M EG. 69

Figure 4.29. Voltage-dependent FEs of anodic EGOR over the Pt/C||h-CoFe-LDH NCs, Pt/C||ys-ZIF@CoFe-LDH NCs and Pt/C||h-Co-LDH NCs pair. 69

Figure 5.1. Schematic illustration of the fabrication of MoC-Fe@NCNTs. 76

Figure 5.2. PXRD pattern and a FESEM image of the as-synthesized ZIF-8 crystals. . 76

Figure 5.3. Structure comparison between (a) ZIF-8 and (b) Zn/Mo-HZIF. $Zn(im)_4$ was partially substituted by MoO_4 in HZIF. 77

Figure 5.4. PXRD pattern and a FESEM image of the as-synthesized Zn/Mo-HZIF nanocubes. 77

Figure 5.5. PXRD pattern and a FESEM image of the as-obtained Fe-Zn/Mo-HZIF nanocubes. 78

Figure 5.6. Digital photos of the (a) Zn/Mo-HZIF and (b) Fe-Zn/Mo-HZIF. 79

Figure 5.7. EDS spectrum of the as-prepared Fe-Zn/Mo-HZIF. 79

Figure 5.8. (a-c) FESEM and (d-f) TEM images of the obtained MoC-Fe@NCNTs; (g) HAADF-STEM image and the EDS mapping of MoC-Fe@NCNTs. 80

Figure 5.9. (a) FESEM and (b) TEM images of Fe-NC dodecahedrons. 81

Figure 5.10. (a) FESEM and (b-d) TEM images of MoC NCs. 81

Figure 5.11. FESEM images of the products obtained by pyrolyzing Fe-HZIF particles with different Fe contents at 700 ℃: (a) 0 mg, (b) 10 mg, (b) 60 mg, and (c) 100 mg. 82

Figure 5.12. FESEM images of products obtained by heating Fe_{30}-HZIF particles at (a) 500 ℃ and (b) 900 ℃. 83

Figure 5.13. (a) PXRD patterns; (b) Raman spectra; (c) N_2 sorption isotherms; (d–f) High-resolution Mo 3d, Fe 2p, and N 1s XPS spectra of MoC-Fe@NCNTs and MoC NCs. 84

Figure 5.14. XPS survey spectra of MoC-Fe@NCNTs and MoC NCs. 85

Figure 5.15. Bifunctional electrocatalytic evaluation toward HER and OER. (a) LSV curves for HER; (b) Comparison of η_{50} and current density under the 300 mV overpotential for HER; (c) Tafel plots for HER; (d) LSV curves for OER; (e) Comparison of η_{50} and current density under the 300 mV overpotential for OER; (f) Tafel plots for OER; (g) C_{dl} plots inferred from CV curves; (h) Nyquist plots; (i) Durability evaluation of MoC-Fe@NCNTs via CA test at j=10 mA cm^{-2} for both HER and OER. 87

Figure 5.16. Polarization curves of MoC-Fe_x@NCNTs with (a) different Fe content and (b) different temperature. 88

Figure 5.17. Cyclic voltammetry curves in a non-faradaic potential region under different scan rates for (a) MoC-Fe@NCNTs and (b) MoC NCs. 88

Figure 5.18. (a) HER and (b) OER LSV curves normalized by corresponding ECSA. 88

Figure 5.19. (a) Schematic illustration of water splitting; (b) polarization curves of MoC-Fe@NCNTs and MoC NCs toward overall water splitting; (c) comparison of the cell voltage at the current density of 10, 50 mA cm^{-2}; (d) i-t curve of MoC-Fe@NCNTs at 10 mA cm^{-2} for 24 h. 90

Figure 5.20. LSV curves towards overall water splitting in alkaline. 91

Figure 5.21. TEM and HAADF-EDS mapping images of MoC-Fe@NCNTs after long-term stability test. 91

Figure 5.22. (a) Survey and high-resolution (b) Mo 3d, (c) Fe 2p, and (d) N 1s XPS spectra of MoC-Fe@NCNTs after long-term stability test. 93

Figure 5.23. Schematic diagram of (a) MoC-Fe, (b) MoC and (c) Fe; (d) charge density distribution of MoC-Fe and (f) TDOS of MoC-Fe, MoC, and Fe. 94

Figure 5.24. System of (a) H, (b) OH, and (c) H_2O adsorption on MoC-Fe. (d) Reaction free energies diagram of hydrogen evolution on MoC-Fe, MoC, and Fe. (e) H_2O adsorption and dissociation-free energies in various configuration. 95

Figure 6.1. Schematic illustration of the synthesis for FeSe-N-C. 101

Figure 6.2. PXRD patterns of ZIF-8 and SeO_2-ZIF-8. 102

Figure 6.3. FESEM images of (a) ZIF-8, (b) SeO_2-ZIF-8, and (c) the representative EDS elemental analysis. 103

Figure 6.4. PXRD pattern of the obtained Se@NC. 104

Figure 6.5. FESEM and TEM images of (a, b) FeSe-NC, (c, d) Fe-NC and (e, f) Se-NC. 105

Figure 6.6. (a) HRTEM, (b) AC HAADF-STEM and (c-g) EDS elemental mapping images of FeSe-NC; (h-k) EDS elemental mapping images of Fe-NC; (i-o) EDS elemental mapping images of Se-NC. 107

Figure 6.7. Powder XRD patterns of FeSe-NC, Fe-NC, and Se-NC. 108

Figure 6.8. Raman spectra of FeSe-NC, Fe-NC and Se-NC. 108

Figure 6.9. N_2 sorption isotherms and the corresponding pore size distributions of (a,d) FeSe-NC, (b,e) Fe-NC and (c,f) Se-NC at 77 K. 109

Figure 6.10. XPS analysis of as-obtained products: (a) survey and (b) N 1s spectra of FeSe-NC, Fe-NC and Se-NC; (c) Se 3d spectra of FeSe-NC and Se-NC; (d) Fe 2p spectra of FeSe-NC and Fe-NC. 110

Figure 6.11. (a) LSV curves, (b) CO Faradaic efficiencies, (c) CO partial current densities and (d) Tafel plots, (e-g) CV curves at various scan rates, (h) the corresponding C_{dl} of three catalysts and (i) long-term stability test of FeSe-NC in H-type cell. 112

Figure 6.12. The CO_2RR performance of FeSe-NC catalysts prepared with (a-c) different content of Se and (d-f) different etching times. 114

Figure 6.13. (a) Schematic illustration of the self-designed flow cell. (b) LSV curves. (c) FEs and (d) CO partial current densities at different potentials for CO generation. Long-term test of (e) FeSe-NC and (f) Fe-NC using 1.0 M KOH as the electrolyte. 116

Figure 6.14. (a) SEM and (b-d) TEM of FeSe-NC after long-term stability test. 117

Figure 6.15. Zn-CO_2 battery measurements. (a) Schematic configuration of the ZCB with FeSe-NC cathode. (b) Discharge polarization and power density curves. (c)

Discharge curves at different current densities and corresponding FE_{CO}. (d) Galvanostatic discharge curves and corresponding FE_{CO} at 2 mA cm^{-2}. (e) Discharge-charge polarization curves. (f) Galvanostatic discharge-charge cycling curves at 0.5 mA cm^{-2}..... 118

List of Abbreviations and Notations

Symbol	Description
Ag	Silver
Ar	Argon
atm	Atmospheric pressure
Au	Gold
B	Boron
BET	Brunauer-Emmer-Teller
Bi	Bismuth
°C	Degrees Celsius
cm^{-1}	Per centimetre
CO	Carbon monoxide
Co	Cobalt
CO_2	Carbon dioxide
CO_2RR	Carbon dioxide reduction reaction
CP	Carbon paper
Cu	Copper
CV	Cyclic voltammetry
D	Proton diffusion coefficients
DACs	Dual atom catalysts
DFT	Density functional theory
DMF	Dimethyl Formamide
ECSA	Electrochemical active surface area
EDS	Energy-dispersive X-ray spectroscopy
EELS	Electron energy loss spectroscopy
EGOR	Ethylene glycol oxidation reaction
EIS	Electrochemical impedance spectroscopy
EtOH	Ethanol
FE	Faradaic efficiency
Fe	Iron
FTIR	Fourier-transform infrared spectroscopy

GO	Graphene oxide
h	hollow
HAADF-STEM	High-angle annular dark-field scanning transmission electron microscopy
HCl	Hydrochloric acid
HER	Hydrogen evolution reaction
HRTEM	High-resolution transmission electron microscope
HZIF	Hybrid zeolitic imidazolate framework
ICP-OES	Inductively coupled plasma optical emission spectroscopy
In	Indium
Ir	Iridium
IrO_2	Iridium oxide
j	Current density
K	Kelvins
KOH	Potassium hydroxide
LDHs	Layered double hydroxides
LSV	Linear sweep voltammetry
M	Mole per litre
mA cm^{-2}	Milliampere per square centimetre
mg	Milligram
mL	Millilitre
Mn	Manganese
MoC	Molybdenum carbide
MOF	Metal-organic framework
mV	Millivolt
NC	Nitrogen-doped carbon
NCNT	Nitrogen-doped carbon nanotube
NCs	Nanocages/Nanocubes
NENU-5	Polyoxometalate-based metal–organic framework
NF	Nickel foam
NH_2	Amino
Ni	Nickel
NMR	Nuclear magnetic resonance

NPs	Nanoparticles
NSs	Nanosheets
O	Oxygen radical
OER	Oxygen evolution reaction
OH	Hydroxy radical
OOH	Oxyhydroxide
ORR	Oxygen reduction reaction
P	Phosphorus
PET	Polyethylene terephthalate
Pt	Platinum
RHE	Reversible hydrogen electrode
Ru	Ruthenium
RuO_2	Ruthenium oxide
S	Sulphur
SACs	Single-atom catalysts
Se	Selenium
SEM	Scanning electron microscope
TEM	Transmission electron microscope
TM	Transition metal
TOF	Turnover frequency
W	Tungsten
XPS	X-ray photoelectron spectroscopy
XRD	Powder X-Ray diffraction
ys	Yolk-shell
ZIF-67	Zeolitic imidazolate framework-67
ZIF-8	Zeolitic imidazolate framework-8
Zn	Zinc
η	Overpotential
µL	Microlitre

Abstract

Developing renewable technologies that consume water or carbon dioxide (CO_2), utilize them as feedstocks and convert them into clean energy and value-added chemicals is meaningful but also challenging. Electrochemical water splitting and CO_2 reduction are promising routes to achieve these aspirations while closing the carbon cycle. The major challenge to realizing such electrochemical conversion is the performance-driven design and fabrication of efficient electrocatalysts. Recently, metal-organic framework (MOF)-derived transition metal (TM)-based layered double hydroxides (LDHs), carbides, and single-atom catalysts (SACs) have emerged as highly active electrocatalysts for oxygen evolution reaction (OER), hydrogen evolution reaction (HER) and CO_2 reduction reaction (CO_2RR), respectively. However, despite the many achievements, developing TM-based catalysts with high activity and selectivity is an ongoing challenge. Hence, in this thesis, novel TM electrocatalysts have been obtained by developing effective control over morphology, composition, interface, and atomic structure.

Morphology control and compositional engineering are first applied to synthesize zeolitic imidazolate framework (ZIF)-derived hollow CoFe-based LDH nanocages (h-CoFe-LDH NCs) and yolk-shell ZIF@CoFe-LDH nanocages (ys-ZIF@CoFe-LDH NCs) for OER and selective small organic molecule oxidation. The resultant h-CoFe-LDH NCs exhibited a commendable OER activity with a small overpotential of 278 mV at 50 mA cm^{-2}. Additionally, controlling the reconstruction degree enabled the formation of ys-ZIF@CoFe-LDH NCs with yolk-shell nanocage nanostructure, which have an appreciable electrocatalytic performance for the selective ethylene glycol oxidation reaction (EGOR) toward formate with a Faradaic efficiency (FE) up to 91%.

Structural and interfacial engineering were then employed to construct molybdenum carbide decorated with iron nanoparticles (NPs) for water splitting. The MoC-Fe@NCNTs (N-doped carbon nanotubes) catalyst displayed fast kinetics and small overpotentials of 252 and 304 mV at 50 mA cm^{-2} for the HER and OER, respectively. Theoretical calculations and experimental observation further prove that the incorporation of Fe NPs enables the creation of a heterointerface with MoC which promotes the OER activity of MoC, thereby endowing an outstanding bifunctional electrocatalytic performance.

An atomic engineering strategy was further implemented to prepare a Fe-Se dual-metal SACs electrocatalyst for CO_2RR. Comprehensive analyses suggest that Se SA served as promoter for boosting the CO_2RR activity and selectivity. Consequently, a distinct synergistic effect was observed in the resultant FeSe-NC, which achieved an excellent CO_2RR performance.

Overall, this thesis has realized the delicate design of MOF-derived TM-based catalysts for enhanced electrocatalytic water dissociation and CO_2 reduction, which will shed light on the further design of novel electrocatalysts for renewable energy conversion and other reactions.

CHAPTER 1 Introduction

1.1. Research background

The over-consumption of fossil fuels (*e.g.*, coal, oil, *etc.*) inevitably results in excessive CO_2 emission globally. The growing energy demand and environmental deterioration have impelled society to search for renewable and alternative energy sources. Currently, renewable energy conversion system, especially electrochemical system, may solve the current energy crisis and pollution issues due to their convenience of energy storage and utilization and environmental friendliness [1]. Small molecules such as water, carbon dioxide, and nitrogen in the natural environment can be converted into important chemicals or energy products such as hydrogen, hydrocarbons, and nitrogen-containing compounds through electrochemical catalysis. The efficiency of the electrolysis systems is greatly governed by the properties of the electrocatalysts. Therefore, the development of efficient, environmentally friendly, and cost-effective electrocatalysts for water splitting and CO_2 conversion is highly meaningful.

Noble-metal materials have been regarded as state-of-the-art catalysts due to their high activity and high efficiency. For example, Platinum (Pt)-based catalysts are typically used to catalyze oxygen reduction (ORR) and HER [2, 3]. Ru- or Ir-oxides are generally considered to be efficient OER electrocatalysts [4]. Au has been widely used to catalyze CO_2RR [5]. However, the high cost, poor stability, and scarcity severely limit their large-scale applications. As excellent substitutes, earth-abundant TM-based electrocatalysts have achieved great success in both water and CO_2 electrolysis. Among them, MOF-derived TM-based catalysts have aroused considerable interest due to their

high conductivity, simple synthetic routes and distinctive catalytic characteristic [6]. For the past decade or more, extensive efforts have been dedicated to exploring the controllable synthesis of MOF-derived TM-based materials, in which promising strategies including surface modification, composition doping, chemical etching, hydrothermal/thermal treatment and *in situ* growth were developed. Despite substantial progress in the syntheses of MOF-derived TM-based catalysts, the exploitation of novel electrocatalysts with high performance for water and CO_2 electrolysis is still an ongoing challenge.

1.2. Research objectives

The focus of this thesis is on exploring MOF-derived TM-based electrocatalysts with high electrochemical activities and economic efficiency for water splitting and carbon dioxide electrolysis. Different TM-based electrocatalysts, such as LDHs, nanoparticles, and single atoms, with distinct structures, compositions, and morphologies are designed and prepared. Their potential applications in electrocatalysis (especially in HER, OER, and CO_2RR) are also evaluated. The concrete objectives of my research are listed as follows:

1. To develop facile strategies to fabricate high-active hollow and yolk-shell nanostructured TM-LDHs electrocatalysts with optimized compositions for OER and small organic molecule oxidation reactions.

2. To synthesize MOF-derived bifunctional TM hybrid nanostructures with outstanding electrocatalytic performance for water electrolysis and reveal the structure-performance relationship via experimental and computation tools.

3. To prepare a MOF-derived atomically dispersed Fe/Se-SA electrocatalyst for efficient CO_2RR and investigate the structure-activity relationship of the resultant

catalysts.

1.3. Research significance

In the present study, efforts are primarily focused on two major problems in the design and synthesis of MOF-derivatives as efficient electrocatalysts for H_2O electrolysis and CO_2 electro-reduction reactions. The significance of the research comes in two aspects. First, the strategies, provided in this research, shed light on the development of efficient MOF-derived catalysts for desired electrochemical reactions. Second, this research can offer an effective approach to tuning the selectivity of electrocatalysts to improve their electrocatalytic performance through structural, interfacial, and atomical engineering. Hence, the results presented here can offer new insight into the design and syntheses, as well as mechanistic understanding of catalysis in electrochemistry-driven energy conversion process.

1.4. Arrangement of the thesis

This thesis is arranged into seven chapters and the overview of each chapter are listed as below.

Chapter 1 presents a briefly introduction of the research background of MOF-derived TM catalysts for relevant electrochemical reactions, the aims and objectives of the research, as well as the research significance.

Chapter 2 summarizes the most recent development of MOF-derived TM nanomaterials that work as electrocatalysts in some energy-related electrocatalytic applications, perspectives and challenges.

Chapter 3 provides detailed information on chemicals and experimental methods, including the preparation and characterization of catalysts, and electrochemical measurements.

Chapter 4 covers a controlled synthesis of MOF-derived hollow and yolk-shell CoFe-LDHs nanocages. Hollow CoFe-LDH nanosheets (NSs) assembled nanocages (h-CoFe-LDH NCs) and yolk-shell ZIF@CoFe-LDH nanocages (ys-ZIF@CoFe-LDH NCs) were readily synthesized by adjusting the etching-reconstruction degree under various conditions. Control experiments revealed that the affinity of anion in iron salts plays a key role in the formation of unique hierarchical nanostructures. Owing to the strong synergistic effect between the hollow/yolk-shell structure, the modified composition and electron structure via Fe-doping, as well as the oxalate groups enlarging the layer spacing of LDHs, the as-prepared h-CoFe-LDH NCs and ys-ZIF@CoFe-LDH NCs exhibited excellent electrochemical performance for OER and EGOR, respectively. This study may provide fundamental insight into the controlled synthesis of TM-based LDHs catalysts with tuneable selectivity for water oxidation and small molecule oxidation reactions.

Chapter 5 introduces a facile strategy to synthesize MOF-derived bifunctional MoC-Fe@NCNTs catalyst for water splitting. By trapping $[Fe(C_2O_4)_3]^{3-}$ units in the Zn/Mo-HZIF framework followed by pyrolysis, MoC nanocrystals and Fe NPs confined in NCNTs (denoted as MoC-Fe@NCNTs) were obtained, which exhibited remarkable electrocatalytic activity and stability for hydrogen and oxygen evolution. Comprehensive analyses demonstrate the boosted intrinsic activity can be attributed to the synergetic effect between MoC, Fe and the NCNTs. Theoretical calculations indicate that the Fe site acts as an efficient OER promoter, while MoC has favorable HER activity, leading to enhanced bifunctional performance. This represents a promising method to synthesize effective MOF-derived water-splitting electrocatalyst.

Chapter 6 reports an efficient CO_2RR electrocatalyst with atomically isolated Fe-Se dual sites immobilized on N-doped carbon (FeSe-NC). Through a selenic-acid pre-etching approach, Se was successfully trapping by the N-doped carbon (Se@NC), which was then used to construct dual-atom electrocatalyst by the adsorption-activation method. The obtained FeSe-NC shows a noteworthy CO_2RR performance affording an industrial-level j_{CO} (>235.0 mA cm^{-2}) and high FE_{CO} (>95 %), far superior to Fe-based single-atom catalysts. This work proves that the fabrication of dual-atom pairs as electrocatalysts is an elegant strategy to boost CO_2RR.

Chapter 7 summarizes the main findings and achievements of the three studies from Chapters 4-6. Besides, further challenges and prospects, such as *in-situ* analysis, and identification of the coordination structure, are also put forward.

CHAPTER 2 Literature Review

2.1. Electrocatalysis

The rapid growth of human society can exacerbate some challenges for energy and ecological systems. The continuous consumption of fossil fuels give rise to rampant CO_2 emissions and climate change. Consequently, developing new technologies on renewable energy production and conversion is of great urgency for researchers. Hydrogen energy, being clean and sustainable, has attracted great interest [7]. In addition, converting CO_2 into high-value-added chemicals is another green and sustainable technology [8]. Electrocatalytic techniques, such as water electrolysis and electrochemical CO_2 reduction, can be powered by renewable sources of electricity under ambient conditions, which is crucial for developing the hydrogen economy and achieving CO_2 conversion with zero carbon emission (**Figure 2.1**) [1].

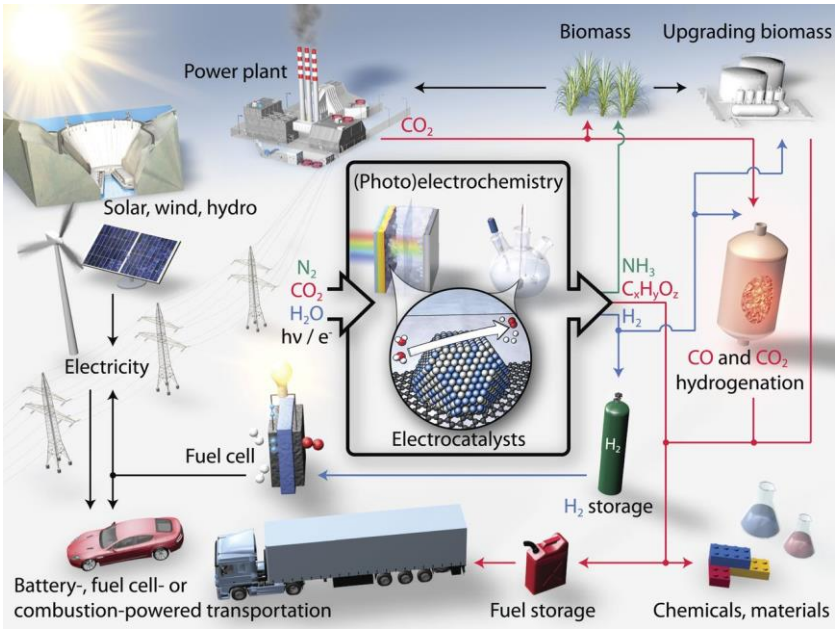

Figure 2.1. Schematics of a sustainable energy future of electrochemical conversion [1].

Electrocatalytic water dissociation consists in two half catalytic processes of cathodic HER and anodic OER, which produce high-purity hydrogen and oxygen gases, respectively (**Figure 2.2**). Water electrolysis process is technologically simple but needs extra energy input since it is an upward reaction rather than a spontaneous process. Theoretically, a thermodynamic voltage of 1.23 V (25 °C, 1 atm) is needed to initiate the water dissociation [9]. However, additional voltage (referred to as overpotential) is required as a result of the sluggish kinetics and high resistance barriers. The kinetic sluggishness of the two half-reactions, especially the four-electron OER process, leads to a low efficiency of water electrolyzers. To break the efficiency limitations, electrocatalysts are utilized to catalyze both anodic OER and cathodic HER, respectively. Currently, noble-metal Pt is commonly employed as a commercial catalyst for HER while RuO_2 and IrO_2 are well-known oxygen evolution catalysts. The above noble-metal-based catalysts are of high efficiency but still lack large-scale commercializations due to their high costs, scarcity and poor stability. To improve the water electrolysis performance, numerous attempts have been made to develop highly efficient HER and OER electrocatalysts during the past decades.

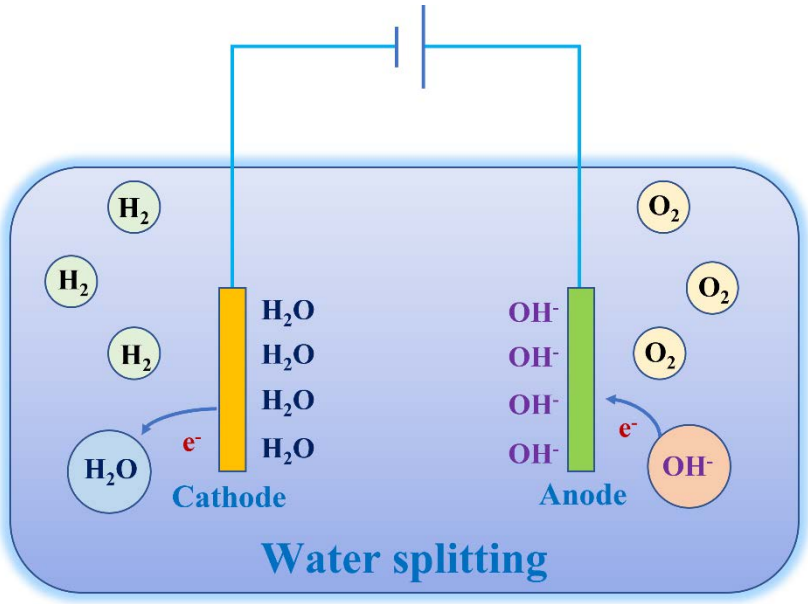

Figure 2.2. Schematics of the electrochemical alkaline water splitting.

2.1.1. Oxygen evolution reaction

2.1.1.1. Fundamentals of oxygen evolution reaction

OER is the anodic half-process of water electrolysis, in which water is oxidized into oxygen at the anode. Besides, OER also involves in many energy-related technologies, such as CO_2 electrocatalytic reduction, metal-air batteries, fuel cells, etc. Different from the two-electron HER, four-electron OER requires the continuous generation of OH^*, O^*, and OOH^* intermediates. Therefore, OER is more sluggish and requires an excessive voltage to initiate the reaction.

In the alkaline electrolyte, OER normally occurs on the catalysts' surface (M: active sites), and the general mechanism is displayed in the following steps (**Figure 2.3**). Firstly, rich OH^- anions are adsorbed on the M site to form M-OH. Then, M-OH is deprotonated and transformed into M-O intermediate. Finally, M-O species can directly combine to form O_2 or transform to M-OOH and then generate O_2 via proton-coupled electron transfer.

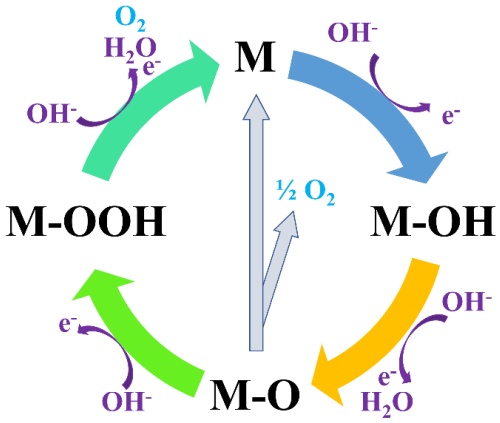

Figure 2.3. The OER mechanism in alkaline medium.

The OER process is a thermodynamically difficult and energy intensive process. Therefore, various strategies, including structural, atomic, surface, and interfacial

engineering, have been developed to design high-efficiency catalysts by regulating the intermediates binding behavior and lowering the reaction barriers.

2.1.1.2. MOF-derived TM-based electrocatalysts for OER

In recent decades, the development of OER catalysts has received extensive attention. As a result, various electrocatalysts have been developed for OER. Among these catalysts, TM-based MOF derivatives are particularly attractive because of their low cost, high conductivity, large surface area, high performance, and porosity. In this section, the recent developments in MOF-derived TM-based catalysts are presented.

MOF-based electrocatalysts. MOFs represent a relatively new class of crystalline materials, in which metallic centers are coordinated by organic linkers. MOFs is regarded as promising OER candidates due to their tunable crystalline structures and functional groups. The organic ligands and metal sites within MOF can affect the bond strengths of highly reactive intermediates (*e.g.*, OH^*, O^*, and OOH^*). However, bulk MOFs still suffer from poor conductivity [10]. To compensate for the lack of electrical conductivity and improve active site exposure, various strategies were explored. For instance, highly porous composite nanomaterials with superior OER properties have been obtained by growing ultrathin MOF nanosheets on conductive graphene oxide (GO) and nickel foam. Compared with bulk crystalline MOFs, two-dimensional (2D) or amorphous MOFs with unsaturated coordination metal sites and edge defects, have shown higher electrocatalytic activity [11, 12]. *In/ex-situ* doping MOF catalysts with secondary metal can decrease overpotentials. Recently, various transition-metal-based MOFs, especially bimetallic MOFs have been assembled and applied for OER [13, 14]. The incorporation of the guest metal species could modify the electronic state of the host metal, thereby regulating intermediate binding energy and facilitating OER (**Figure 2.4**) [15].

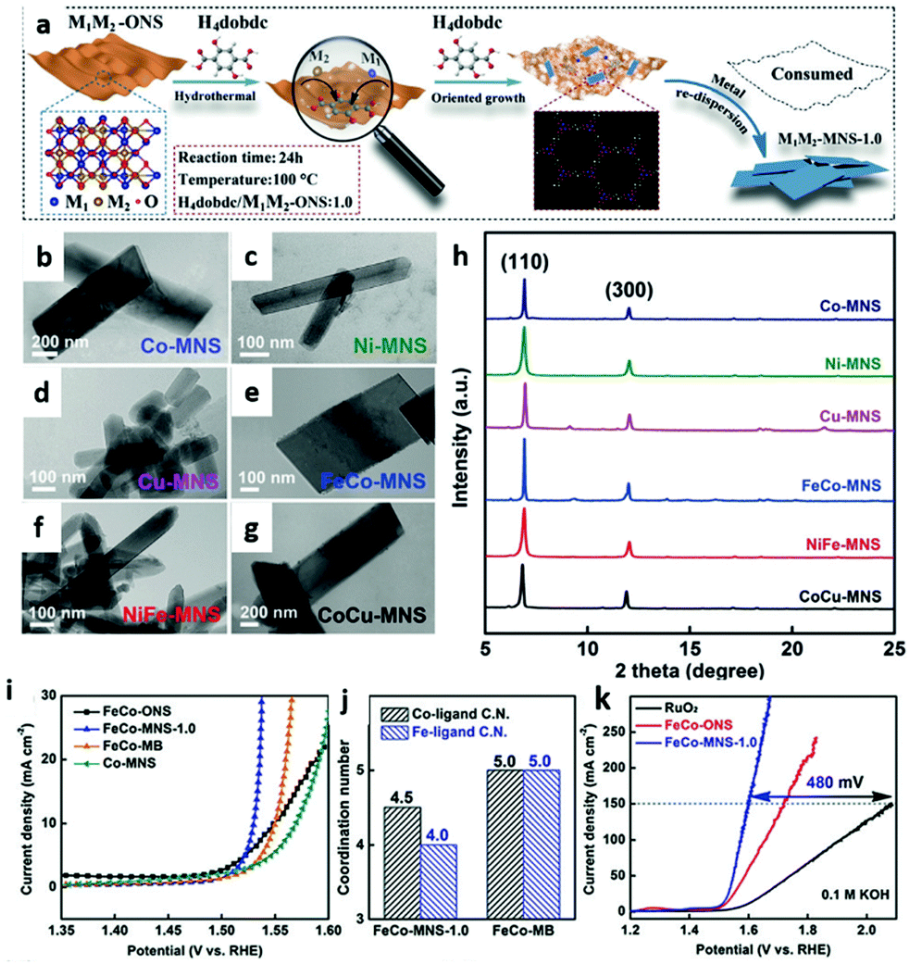

Figure 2.4. Preparation and characterization of M-MNS-1.0. (a) Schematic illustration of the 2D oxide sacrifice approach (2dOSA) for the conversion of M-ONS with H4dobdc ligand to form M-MNS. (b–g) TEM images of Co-MNS, Ni-MNS, Cu-MNS, FeCo-MNS, NiFe-MNS, and CoCu-MNS. (h) XRD patterns of the synthesized MOF-74 nanosheets. (i) OER polarization curves of FeCo-ONS, FeCo-MNS-1.0, FeCo-MB, and Co-MNS in 0.1 M KOH. (j) The C.N. for the Co-ligand and Fe-ligand of FeCo-MNS-1.0 and FeCo-MB. (k) OER curves of FeCo-MNS-1.0, FeCo-ONS, and RuO_2 loaded on Ni foam with a loading of 2.0 mg cm^{-2} in 0.1 M KOH. [15].

Most pristine MOFs still suffer from deactivation due to their poor chemical stabilities. This limitation can be overcome by converting MOFs to diverse derivatives, such as carbon nanohybrids (carbon-captured metal single atom, nanoparticles, and alloys) and metal compounds (phosphides, selenides, borides, oxides, and hydroxides), owing to

the coexistence of metallic species and organic ligands in the frames. The resultant MOF-derived TM-based nanomaterials could be further utilized as cost-efficient OER electrocatalysts.

MOF-derived metal-carbon nanohybrids as OER electrocatalysts. Through direct calcination of MOFs, metal-carbon nanostructures can be easily obtained, and they can inherit the well-defined morphology, high surface area, and porosity. During the pyrolysis, metal ions/clusters are reduced to metal/alloy nanoparticles while organic ligands are carbonized. Metal-carbon hybrid materials derived from MOFs have certain advantages. The density of exposed active sites can be regulated by the selection of MOFs with specific morphologies, surface areas, and pore structures. The strong adhesion between highly distributed metal species and carbon shells can enhance mass and charge transfer, as well as prevent the aggregation of nanoparticles. In addition, the flexible and diverse organic linkers facilitate the integration of heteroatoms (*e.g.*, P, N, S, B, *etc.*) into the carbon skeleton [16]. Carbon substrates with heteroatom doping can induce extra active sites, which could improve the intrinsic activity. Moreover, the synergistic cooperation between metal species, heteroatom doping, and carbon can not only optimize the electronic configuration but also favour electron transfer, thereby facilitating OER kinetics [17, 18]. For instance, Qiu and co-workers [19] reported a NC@Co-NGC nanocage with Co NPs confined in hollow carbon nanocage by controlled calcination of core-shell ZIF-8@ZIF-67, which show a boosted OER activity (**Figure 2.5**). DFT analysis revealed that the uncoordinated C atoms with respect to Co lattice favour adsorption of OOH^* intermediate, thereby enhancing the OER performance.

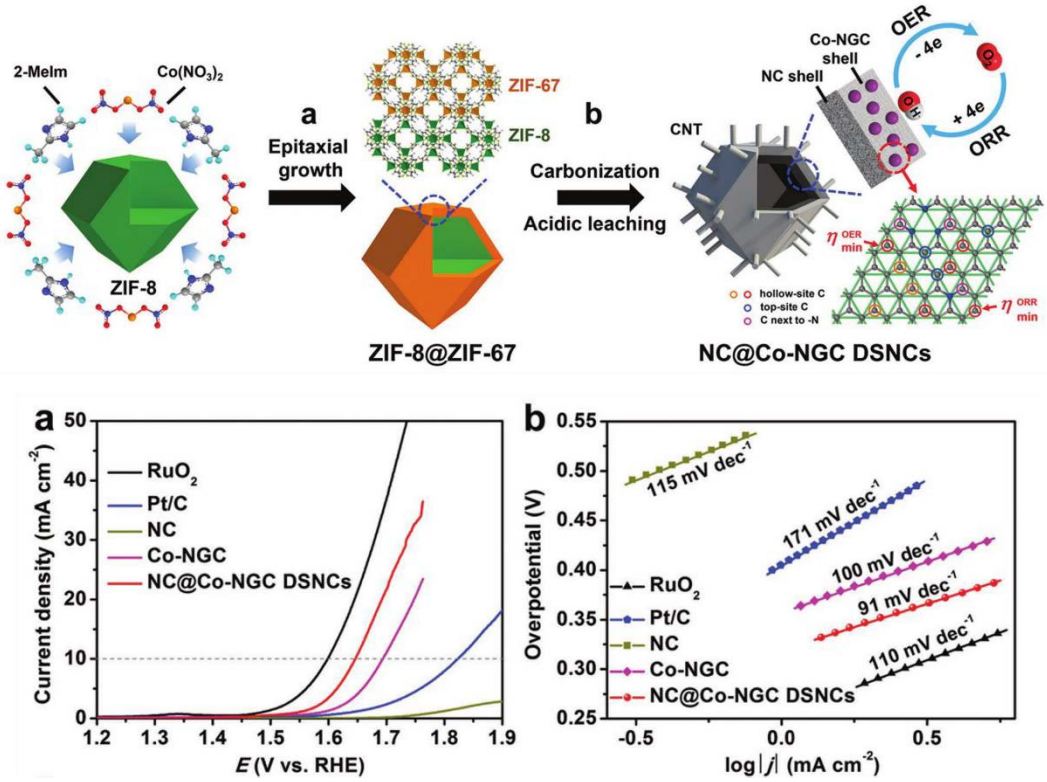

Figure 2.5. Schematic illustration of the synthesis of NC@Co-NGC DSNCs. (a) *iR*-corrected OER polarization curves of NC, Co-NGC, NC@Co-NGC, Pt/C, and RuO_2 catalyst in O_2-saturated 0.1 M KOH solution and (b) Tafel plots of NC, Co-NGC, NC@Co-NGC, Pt/C, and RuO_2 catalyst[19].

Apart from the doping of single non-metallic elements, heteroatom co-doping has also received extensive attention in recent years. With this strategy, Zou and co-workers [20] synthesized a Co-B/N catalyst derived from N, B containing Co-MOFs (CoTIB). The MOF-derived N, B co-doping material exhibited better OER activity than the control samples, demonstrating the role of heteroatoms co-doping in high-performance OER catalysts.

Recently, TM-based SACs with monodispersed metal atom embedded in an N-doped carbon matrix (M-N-C) have drawn increased attention for OER because of their high activity. According to the reported studies, doping heteroatoms into carbon skeletons showed strong catalytic enhancement on OER. However, the performance of mono metal

sites is still unsatisfactory in most reported SACs catalysts because of the homonuclear metal sites and relatively low loading. Recent studies have demonstrated that a secondary metal site can induce strong synergistic interaction and subsequently improve the OER activity of SACs. Later, Lou and co-workers [21] synthesized a dual-metal a-NiCo/NC catalyst, in which strong synergistic interactions between Co and Ni active sites was observed. As shown in **Figure 2.6a**, the resultant a-NiCo/NC catalyst displayed robust OER performance and stability, which outperforms the single-metal samples, and even commercial RuO_2. Similarly, Hu and co-workers [22] reported a CoNi-SAs/NC catalyst with Co-Ni pairs atomically dispersed in a NC nanoframe (**Figure 2.6b**). Thanks to the synergy of neighbouring Co-Ni dual metal sites, the as-obtained CoNi-SAs/NC hybrid exhibited outstanding OER performance. Theoretical computations demonstrate that the introduction of adjacent metal atoms can modify the adsorption/desorption behaviours and reduces the energy barriers, ultimately boosting the OER performance.

Although TM SACs have been widely employed for catalyzing OER and great progress has been achieved, there is still room for improvement especially in separating and stabilizing single-atom active sites. In future research, priority should be given to the design, synthesis, and atomic characterization of SACs catalysts, especially involving dual metals.

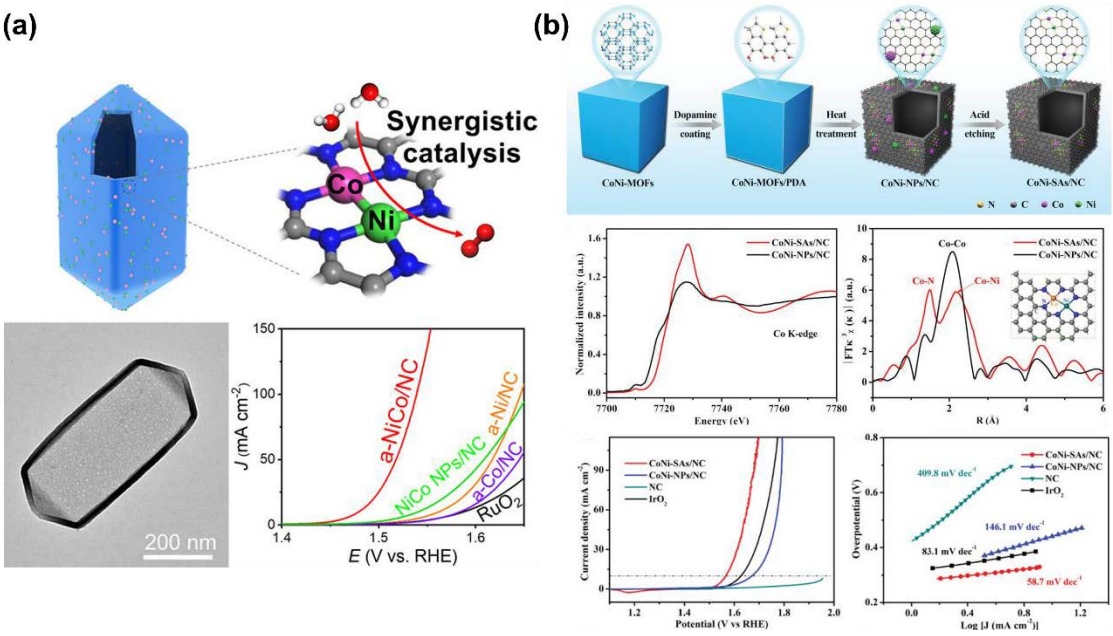

Figure 2.6. (a) Synthesis and OER performance of the a-NiCo/NC [21] and (b) Scheme for the synthesis, characterization and OER performance of CoNi-SAs/NC [22].).

MOF-derived metal compounds as OER electrocatalysts. Apart from the MOF-derived metal-carbon materials, numerous TM-based MOF derivatives have been developed, including oxides [23, 24], hydroxides [25], sulfides [26], phosphides [27], borides, nitrites [28], and other compounds. Thanks to a metal-organic hybrid feature and nanoscale morphology, MOFs are often used as bifunctional precursors serving as both self-sacrificing templates and metal sources for the construction of diverse nanostructures, such as hollow, yolk-shell, core-shell, etc., which have shown interesting performance in water electrocatalysis [29-31]. Using this method, complex functional materials have been synthesized and remarkable progress has been achieved. For example, the template-engaged reaction of ZIF-67 with phytic acid and subsequent pyrolysis led to the formation of hollow CoP/C nanocubes [16]. Recently, MOF-derived hollow TM-based oxides, sulfides, and selenides nanocages were found to be promising OER electrocatalysts. As highlighted by Hu and co-workers [32], carbon-coated metal selenides can be prepared by a simple etching approach using different MOFs (**Figure 2.7**). The as-prepared

$Co_{0.85}Se_{1-x}$@C nanocages showed a significant improvement in OER activity, benefitting from the abundant Se vacancies, enhanced electrical conductivity, and reduced reaction barriers. The binding of intermediates on catalysts is modified by the incorporation of heteroatoms, which contributes to the boosted OER activity.

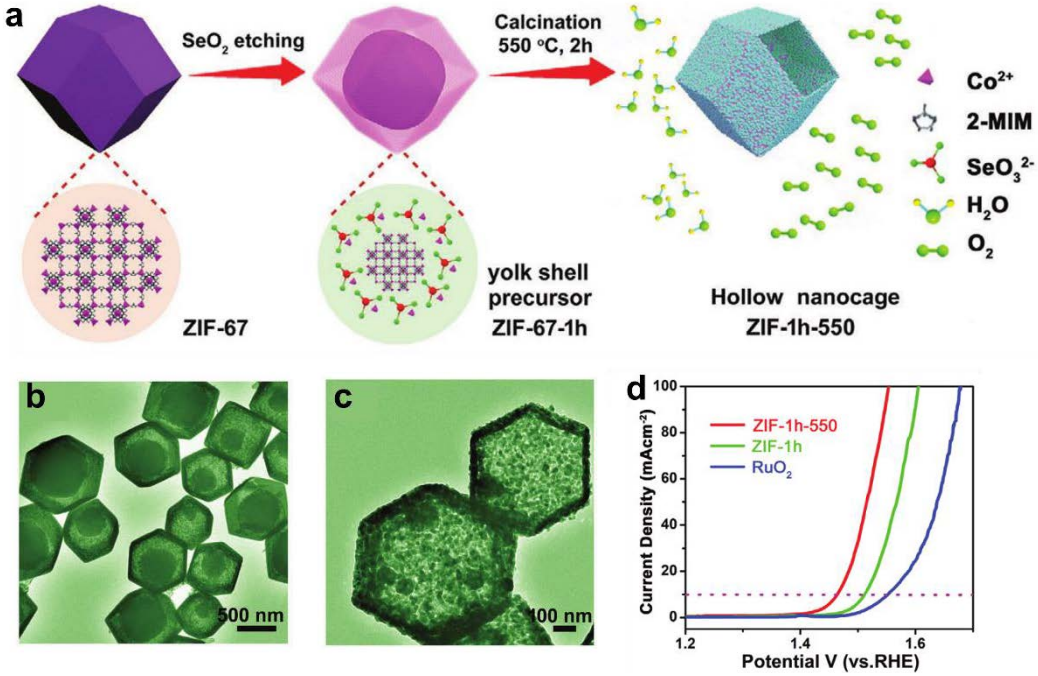

Figure 2.7. (a) Schematic illustration of the synthesis of $Co_{0.85}Se_{1-x}$@C nanocages, (b) TEM image of ZIF-1h, (c) TEM image of ZIF-1h-550 and (d) OER LSV curves of ZIF-1h-550, ZIF-1h, and RuO_2 [32].

Among various promising MOF derivatives, layer double hydroxides (LDHs), especially TM-based LDHs (*e.g.*, Fe, Co, Ni), are frequently reported with appreciable HER activity owing to their earth abundance, unique structure, and tunable composition. Layer hydroxides facilitate the intercalation of ions between layers, thereby decreasing mass transport resistance. Compared with bulk LDHs or nanosheets, hollow and hierarchical LDH nanocages with highly exposed active sites and large surface areas are expected to possess higher OER activity. In light of this, a general self-templated strategy has been developed to fabricate hollow LDH nanocages consisting of ultrathin nanosheets

(**Figure 2.8a**). This strategy involves the hydrolysis reaction of metal ions released from the introduced salts and simultaneous etching of MOF precursors [25]. By carefully modulating the etching reactions and solution compositions, different structures including yolk-shell, hollow and multi-shell nanoarchitectures with significantly enhanced electrocatalytic OER activity have been obtained [33-36].

Further doping with additional metal atoms in LDHs can remarkably upgrade the OER activity [37, 38]. To be more specific, the MOF-derived LDH nanocages provide large surface areas and rich defects, which will stabilize single metal atoms [39]. Wu and co-workers [40] found that imbedded single Ru atom in AC-FeCoNi LDH can significantly decrease the reaction barriers, thus facilitating the OER process (**Figure 2.8b-e**).

Recently, defect engineering, especially cation vacancy engineering, gains increasing attention due to its effective role in regulating the electronic structure, thereby promoting electrocatalytic activity [41]. Therefore, it is expected that inducing metal cation vacancies in LDHs can also improve the intrinsic activity for OER.

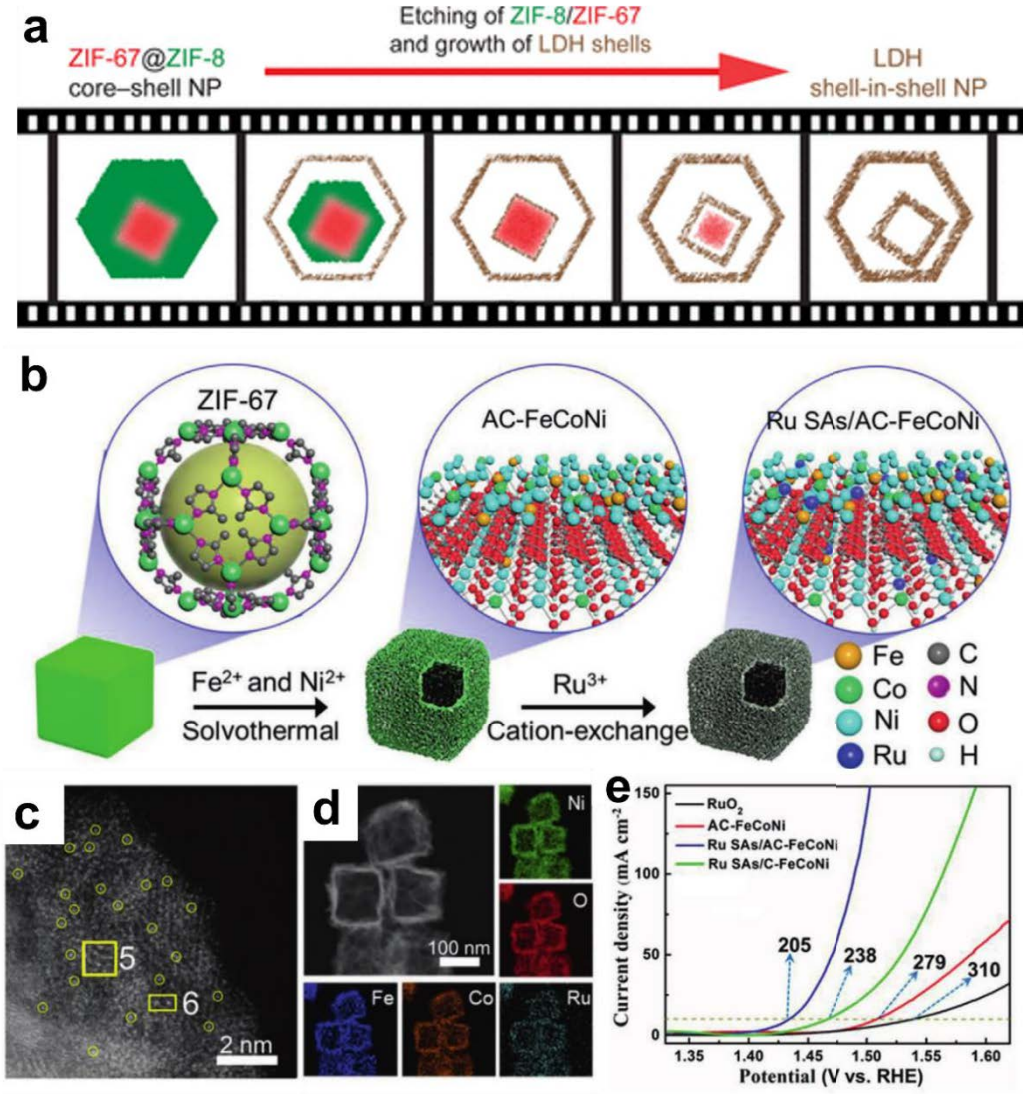

Figure 2.8. (a) Schematic illustration depicting the conversion process of a core-shell ZIF NP into a shell-in-shell LDH nanocage [42], (b) illustration for the synthesis of Ru SAs/AC-FeCoNi, (c) AC HAADF-STEM image, (d) HAADF-STEM image and corresponding elemental mappings of Ru SAs/AC-FeCoNi, and (e) OER LSV curves of RuO_2, AC-FeCoNi, Ru SAs/AC-FeCoNi, and Ru SAs/C-FeCoNi [40].

2.1.2. Hydrogen evolution reaction

2.1.2.1. Fundamentals of hydrogen evolution reaction

As another important half-reaction of water electrolysis, HER is a two-electron process. For alkaline HER, H_2O molecules are first dissociated to deliver the required free protons for the reaction to proceed due to the lack of H^+. The HER would experience Volmer step ($H_2O + e^- \rightarrow OH^- + H^*$) and Heyrovsky step ($H_2O + e^- + H^* \rightarrow OH^- + H_2$) in alkaline media [43].

Compared with acidic HER, additional energy is required to produce protons in alkaline electrolytes, which results in quite sluggish kinetics. Moreover, hydroxide anions are generated near the electrode surface with the consumption of water molecules, which could consequently lower the concentration of water molecules and disrupt the equilibrium of water dissociation. These mechanistic insights reveal that the alkaline HER process is more energy intensive than acidic HER and even the benchmark Pt suffers from low alkaline HER efficiency [44]. Therefore, it is desirable to develop alternative electrocatalysts for alkaline HER. According to previous works, the strength of H^* binding and energy required for H_2O dissociation play a crucial role in determining the alkaline HER activity [45]. Consequently, promoting the water dissociation while achieving moderate hydrogen adsorption, is an effective strategy for designing effective alkaline HER catalysts.

2.1.2.2. MOF-derived TM-based electrocatalysts for HER

Electrocatalysts based on the late first-row transition metals are reported to be highly active HER electrocatalysts. MOF-derived monometallic electrocatalysts, commonly in form of nanoparticles, are a great choice but struggle to deliver efficient HER due to

insufficient active sites [46]. Bimetallic electrocatalysts such as TM-alloys appear more effective and numerous bimetallic MOF-derivatives containing Fe, Co, Ni, Mo, W, or a noble metal, have recently emerged. However, their performances are still unsatisfactory because they trend to agglomerate at high overpotentials. TM-based compounds (*e.g.*, nitrides, phosphide, and chalcogenides) are good substitutes, where N, P, S, and Se-containing groups have been widely applied to functionalize MOFs to enhance catalytic HER performances. For example, Zang's group [47] synthesized a Cu_3P@NPPC catalyst using Cu-NPMOF, whose ligands containing N and P heteroatoms led to *in-situ* phosphidation of Cu and doping of carbon matrix during pyrolysis This electrocatalyst delivered a low overpotential of 89 mV for η_{10}. Moreover, the use of MOFs as template precursors allows the construction of porous nanocomposites containing carbon-coated nanoparticles, which helps to improve the conductivity and prevent aggregation of active sites, thereby enhancing the HER activity.

Beyond Fe/Co/Ni-based materials, numerous Mo/W-based nanomaterials have been developed with excellent HER performance. The electronic structures of MoC_x, WC_x, MoS_2, and MoP suggest that these compounds can be promising alternatives to Pt. Mo/W-based MOF-derivatives, including carbides, sulfides, nitrides, and phosphides, represent a new generation of economical catalysts for alkaline HER [48]. Lou and co-workers [49] fabricated MoC_x nano-octahedrons from a MOFs-based compound (NENU-5) (**Figure 2.9a**). The HER performance of MoC_x is greatly improved by the presence of amorphous carbon matrices. Employing the same strategy, MoN-NC and MoP@PC were fabricated from NENU-5 and showed good HER performances [50, 51]. In addition, catalysts possessing different phases should be favorable for HER because dual phases with optimized electronic configuration can facilitate the mobility of protons [52-55]. For example, dual-phased MC-M_2C/PNCDs (M = Mo or W) catalysts were achieved by

pyrolyzing molybdate/tungstate-functionalized ZIF-8 (**Figure 2.9b**) [52]. The strong cooperative interactions between the dual carbides endow the resultant composites with optimized capability for water dissociations and hydrogen desorption, thereby possessing synergistic enhancement in HER performances.

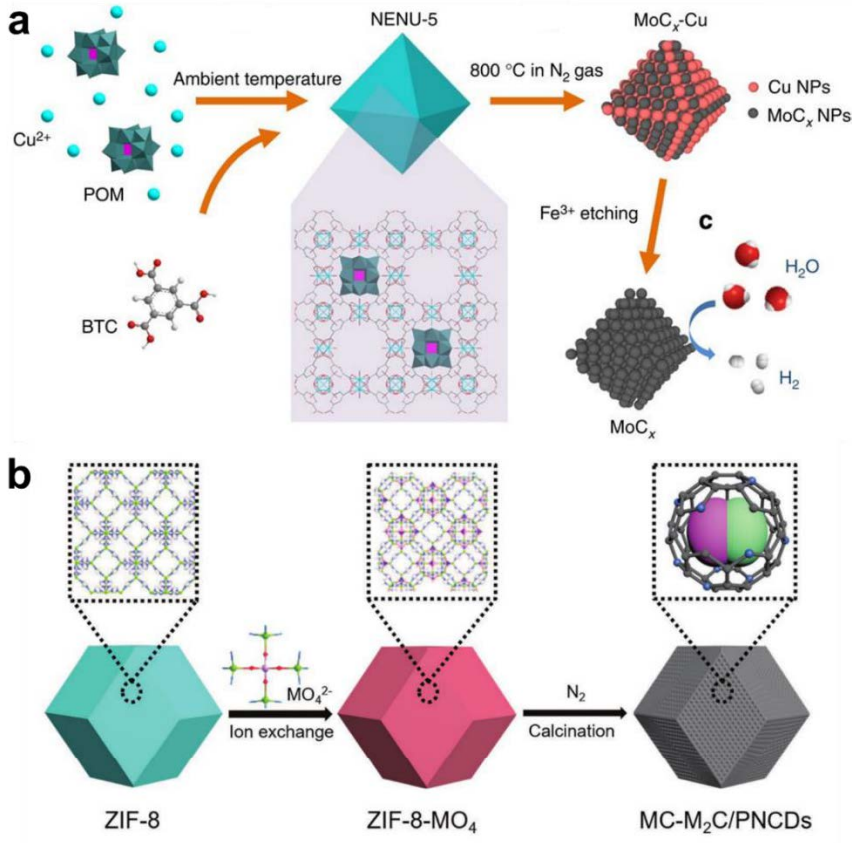

Figure 2.9. Scheme for the syntheses of (a) porous MoC_x nano-octahedra [49] and (b) MC-M_2C/PNCDs [52].

2.1.3. Overall water splitting

Electrocatalytic water splitting is composed of cathodic HER and anodic OER, and both reactions, especially OER, require effective catalysts. Although some effective HER and OER electrocatalysts have been developed, it is highly desirable to design a bifunctional catalyst capable of catalyzing both reactions. Transition metal components in MOFs are currently of interest but only some of them can serve as bifunctional

HER/OER catalysts. Pristine MOFs are normally electrochemically inert, but they are good platforms to provide catalytic sites for both HER and OER. Consequently, there has been remarkable interest in enhancing water dissociation using bifunctional MOF derivatives.

MOF-derived TM and their compounds have been studied as water-splitting electrocatalysts. For example, Chen and Li's group [56] fabricated a MOF-derived hybrid composite with CoP NPs encapsulated in a N-doped CNT hollow polyhedron (NCNHP), which shows commendable HER and OER bifunctional activities (**Figure 2.10**). The electron interactions between CoP and NCNHP increase the bond strength of H^*, thereby leading to excellent performance with a low voltage of 1.64 V to obtain10 mA cm^{-2}.

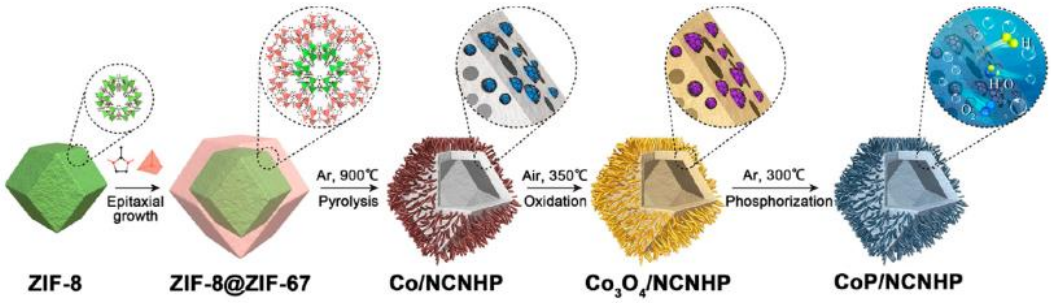

Figure 2.10. Scheme for the synthesis of CoP/NCNHP [56].

Heterostructure engineering is also effective in developing novel electrocatalysis as water dissociation prefers to occur at the interfaces. For instance, Co and its phosphide (CoP) heterojunction with abundant Co/CoP interfaces featured remarkable activity [57] (**Figure 2.11**). Following a similar approach, Zhu and co-workers [58] developed CoP modified by atomic Ni which also displayed high catalytic performance.

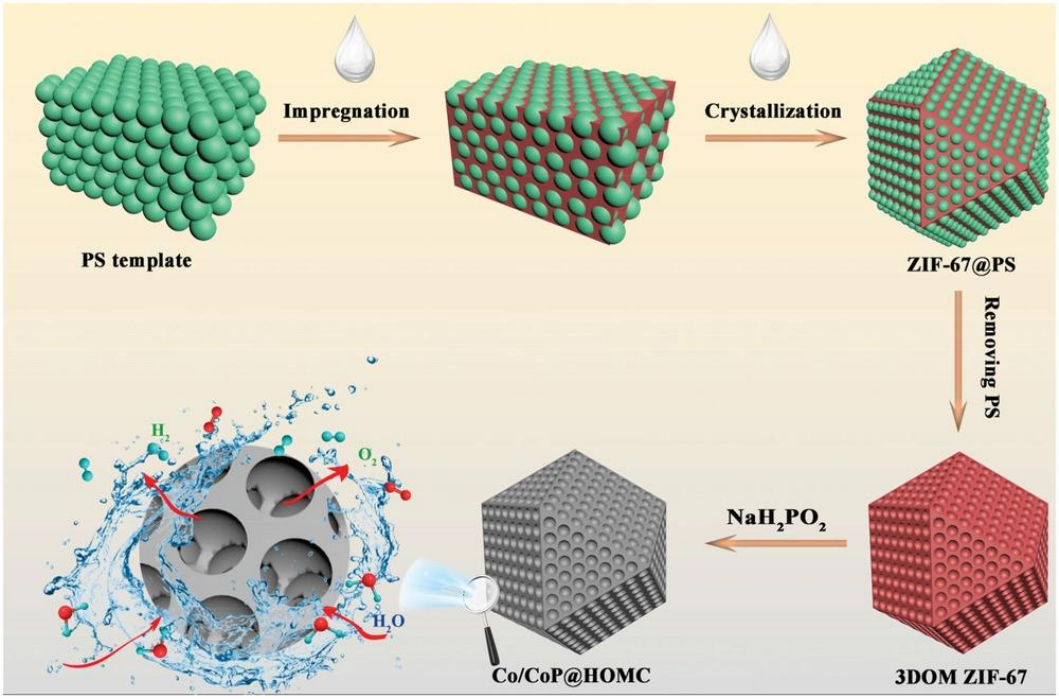

Figure 2.11. Schematic illustration for the synthesis of Co/CoP@HOMC [57].

Introducing additional metal atoms into phosphides to form bimetallic or trimetallic compounds can also lead to significant enhancement of bifunctional performance. For instance, Zhao and co-workers [59] reported a MOF-74-derived Co_4Ni_1P with η_{10} values of 129 mV, 245 mV, and 1.59 V for HER, OER, and overall water splitting, respectively, due to the enhanced active sites and cooperative interactions between NiCoP and Co_2P. Tang and Wang's group [60] found that Co decorated with noble Ir (Co@Ir/NC-10%) delivered better bifunctional activity than Co alone.

2.2. Electrochemical CO_2 reduction

2.2.1. The fundamentals of CO_2 electroreduction

Carbon dioxide (CO_2), a waste product from fossil fuel consumption, is readily available. The excessive emission of CO_2 could result in a rising global temperature, and therefore, change the climate and disrupt the carbon cycle in nature. There is an urgent

need for developing technologies that convert CO_2 into value-added chemicals. Consequently, the electrochemical CO_2 reduction reaction (CO_2RR) has been developed.

As shown in **Figure 2.12**, CO_2RR comprises a cathode, an anode, a CO_2-saturated electrolyte, and a membrane. Specifically, the cathode drives the CO_2RR, and at the same time, an oxidation reaction, such as OER, takes place on the anode. During reactions, the products of oxidation and reduction is separated by a gas-impermeable ion-exchange membrane while maintain charge neutrality. As for the electrolyte, it should be effective in transporting the charged species and facilitating the transport of CO_2 to reach the cathodic electrocatalyst surface. Furthermore, the pH of electrolytes also greatly influences the efficiency of CO_2 reduction [61].

CO_2 is an inert linear molecule with high thermodynamic stability and demands high energy input to reduce it to desirable products. For example, the thermodynamic potentials for reducing CO_2 to different products are listed in **Table 2.1** [62]. However, the actual energy input required for CO_2RR greatly exceed the thermodynamic value due to the activation barrier and complex pathways. Therefore, the heart of the electrochemical CO_2RR is to develop a catalyst that transforms the CO_2 molecule into useful chemical products under moderate conditions.

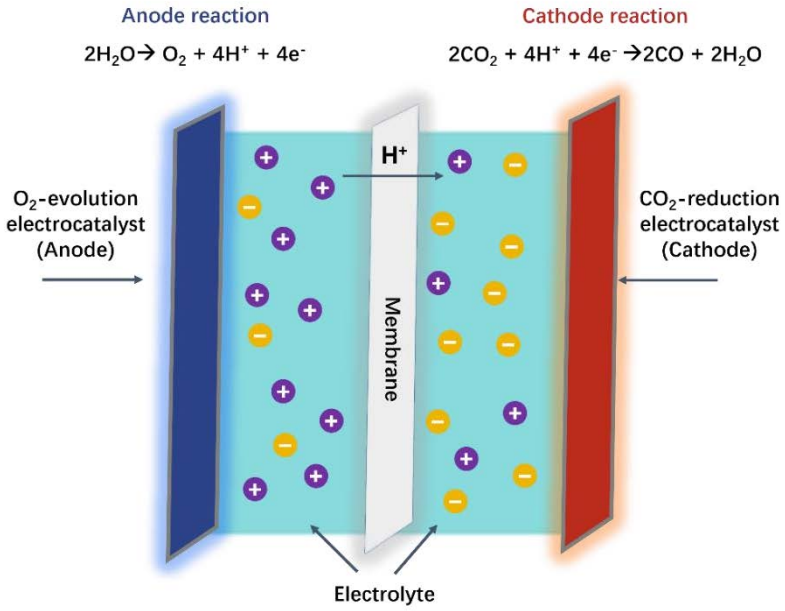

Figure 2.12. A typical electrochemical CO_2 reduction system.

Table 2.1. Reaction pathways for different products of electrochemical CO_2 reduction [62].

Reaction pathway	E_0 (V vs. RHE)
$CO_2 + 2H^+ + 2e^- \rightarrow CO_{(g)} + H_2O$	−0.11
$CO_2 + 2H^+ + 2e^- \rightarrow HCOOH_{(aq)}$	−0.21
$CO_2 + 6H^+ + 6e^- \rightarrow CH_3OH_{(aq)} + H_2O$	0.03
$CO_2 + 8H^+ + 8e^- \rightarrow CH_{4\,(g)} + 2H_2O$	0.17
$2CO_2 + 8H^+ + 8e^- \rightarrow CH_3COOH_{(aq)} + 2H_2O$	−0.26
$2CO_2 + 12H^+ + 12e^- \rightarrow C_2H_5OH_{(aq)} + 3H_2O$	0.09
$2CO_2 + 12H^+ + 12e^- \rightarrow C_2H_{4\,(g)} + 4H_2O$	0.07

As with all electrocatalysts, a CO_2RR electrocatalyst is evaluated from some key parameters including the overpotential, selectivity, current density, turnover frequency (TOF), stability, and energy efficiency.

In general, the most desirable electrocatalysts will drive CO_2RR at the thermodynamical potential (E_0) under ideal conditions. However, in reality, additional energy input is required (known as onset overpotential) since it is a nonspontaneous process. Greater energy input, namely, electrochemical overpotential exceeding the thermodynamic value, is needed to trigger CO_2RR at palpable rates. Moreover, the multiple reactions at similar thermodynamical potentials further complicate the CO_2 reduction process, making it difficult to get single product.

Selectivity is defined as the percentage of efficiency for producing a desired product, which is commonly referred to as Faradaic efficiency. Different from water splitting, there exist competing reactions (HER) in CO_2RR. Hence, most of the reported CO_2RR electrocatalysts possess less than 100% FE. Based on the FE, by multiplying the total current density by FE, the partial current density representing the effective current density for producing a specific product can be obtained. Beyond intrinsic activity of the electrocatalyst, the partial current density is also affected by the electrolyte and the type of electrochemical cell. For example, the partial current density in H-cell is greatly limited by the CO_2 solubility and diffusion [63]. This limitation can be overcome by using gas diffusion flow-cell systems with higher gas flow rates and better contact between CO_2 and catalysts, while preserving their high FE and achieving industry-level current density [64]. Durability is another important criterion of CO_2RR electrocatalyst and an ideal CO_2RR electrocatalyst is expected to show negligible degradation in activity including the FE, current density, and overpotential.

A good CO_2RR electrocatalyst are expected to have a low onset potential and low Tafel slope. Also, the partial current density, turnover frequency (TOF), and FE for a specific product should be higher. Meanwhile, the impacts of electrolytes, substrates and the type of electrochemical cell should not be overlooked. A comprehensive discussion on the mesoscopic effects of different parameters can be found in a review by Sargent and co-workers [65]. In the following section, the recent development of CO_2RR electrocatalyst for CO production is summarized.

2.2.2. MOF-derived electrocatalysts for CO_2RR to CO

In recent years, a variety of CO_2RR electrocatalysts have been designed, including but not limited to metals, metal oxides, alloys, molecular complexes, and metal-free carbon-based materials. CO is the simplest gas product for CO_2RR. Precious metals (Au, Ag, and Pd) are considered to be a class of highly active CO_2RR electrocatalysts for the CO_2-to-CO reduction [66-68]. Nevertheless, their high cost and scarcity are the greatest obstacle to practical applications.

Electrocatalyst based on SACs, featuring isolated metal atom dispersed on a conductive substrate, are attractive, and it shows superior CO selectivity. Back in the 1970s, cobalt and nickel phthalocyanines with well-defined M-N_4 sites were first reported with commendable activity for CO_2 electro-reduction [69]. Since then, metal-organic composites featuring isolated M-N_4 sites have been extensively studied as CO_2RR electrocatalysts by physical or chemical immobilization of these molecular catalysts on conductive supports [70, 71]. Recently, heterogeneous SACs catalysts derived from MOFs possessing similar M-N_x configurations attract extensive attention for CO_2RR because of their facile preparation procedures, flexible structure, high conductivity and

superior electrochemical stability [72]. Most of these MOF-derived SACs with CO as the main product outperform traditional precious metal electrocatalysts such as Au and Ag.

Owing to the facile syntheses and tunable composition, ZIF-8 is an ideal material for the preparation of various SACs. Direct pyrolysis of ZIF-8 harvests porous carbon materials with N-rich defects, during which the reduced metallic Zn evaporates easily due to its low boiling point. These N-rich defects can serve as anchoring sites to stabilize metal atoms and prevent the formation of metal nanoparticles, thereby obtaining SACs. Furthermore, through physical adsorption, ion exchange, and cage confinement strategies (**Figure 2.13**), single-atom Co, Ni, Cu, Fe, Mo, In, etc. have been constructed and studied for CO_2RR [73-75]. The activity/selectivity of SACs for CO_2RR varies with the different metal centers, even in similar coordination environments. For example, Pan et al. [76] obtained Fe and Co SACs from Fe or Co-substituted ZIF-8. The resultant Fe SACs exhibited a better CO_2RR performance than Co-N-C and NC catalysts. Following a similar approach, Li and co-workers successfully confined Ni ions in ZIF-8 pores through a double-solvent method and obtained single Ni atom anchored on NC (**Figure 2.13b**). The resultant Ni SAs/NC catalyst delivered a maximum FE_{CO} of 71.9% at −0.9 V_{RHE}. Compared with Fe SACs, Ni SACs had significantly higher overpotentials due to the strong *COOH binding strength. Co SACs catalyzed CO_2RR at a low onset potential but had unsatisfactory CO selectivity as a result of competing HER.

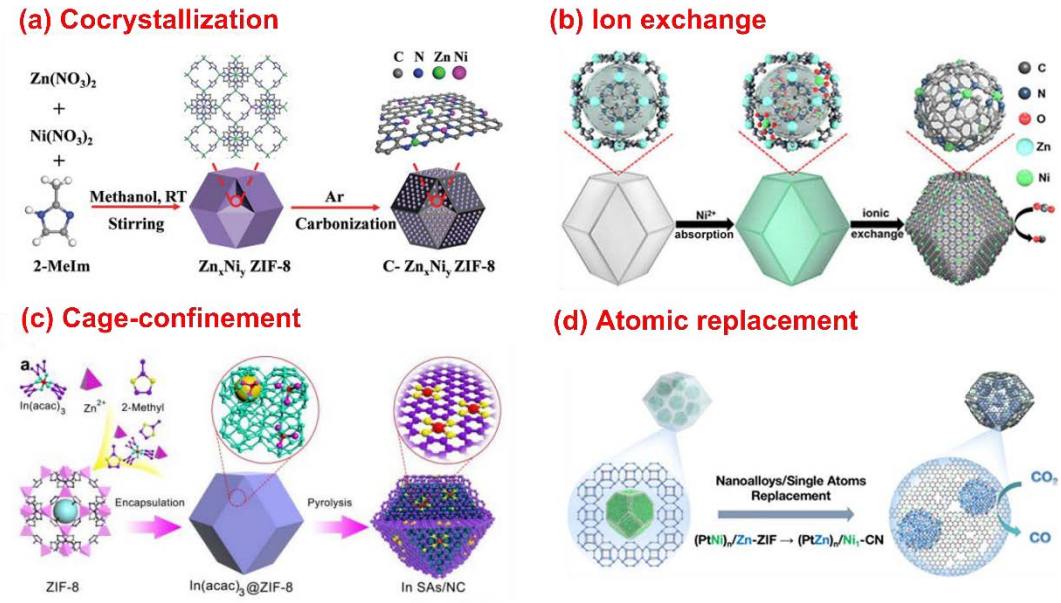

Figure 2.13. MOFs-derived SACs by different strategies. (a) co-crystallization, C-Zn_xNi_y ZIF-8 catalysts [77]; (b) ion exchange, Ni SAs/N-C catalyst [75]. (c) cage-confinement, InSAs/NC[73]; (d) atomic replacement, $(PtZn)_n/Ni_1$-CN [78].

Enhancement in CO_2RR performance of these MOF-derived SACs can be also achieved by adjusting the coordination number of the central atoms, which could be realized by varying pyrolysis temperatures. Yan et al. [77] reported an unsaturated Ni SAC with high Ni loading (5.44 wt%) starting from Ni-doped ZIF-8. The obtained Ni SAC had appreciable CO_2RR activity with high FE_{CO} of over 92% from −0.53 ~ −1.03 V_{RHE}. DFT calculation uncovered that the unsaturated Ni-N_x sites is more active for CO_2RR than Ni-N_4 sites. The same observation was made by replacing Zn of low coordination number with Ni [79]. However, several studies show that there is still relatively high loading of Zn after pyrolysis of ZIF-8, which should not be overlooked [80, 81].

Conductive carbon supports doped with heteroatoms (*e.g.*, F, S, P, B, etc.) are known to affect the electrocatalytic performance [82]. Certainly, the coordinated or neighbouring atoms stabilizing central atoms on carbon substrates could also influence the CO_2RR activity and selectivity. It is comprehended that heteroatom dopant in carbon skeletons

plays an important role in modulating the electronic configuration and microenvironment of metal centers in SACs, as well as the binding of intermediates. It was found that incorporating P elements in the Fe SAC (Fe-SAC/NPC) increased the binding strength of *COOH, thereby enhancing CO_2RR activity [83]. Liu and co-workers [84], witnessed a similar enhancement in the CO_2RR performance of Fe SAC after doping with B and N, which presented a high FE_{CO} of ~94% at −0.7 V_{RHE}. Theoretical calculations suggested that the integration of B dopants can modulate the electronic configuration of the Fe sites, resulting in a boosted CO_2RR performance.

Recently, dual atom catalysts (DACs) were found to perform better CO_2RR than these mono-metal SACs as they endow active sites with more favorable intermediate adsorption/desorption energies. A secondary metal atom decorating the first one could serve as a promoter, hence allowing new reaction pathways. DACs with synergetic metal atoms can therefore improve CO_2RR performance. According to the polarity of metal bonds, DACs roughly falls into three categories (**Figure 2.14**): (a) DACs with metal-metal bonds whose atomic nuclei are the same or different; (b) DACs with heteroatomic bridging featuring metal-heteroatom-metal bonds. (c) Site-isolated DACs exist in an in-plane or spatially separated form. So far, the commonly reported combinations are Ni-Co, Ni-Fe, Co-Fe, Ni-Cu, Ni-Zn, Mo-Se, and In-Ni [85-87].

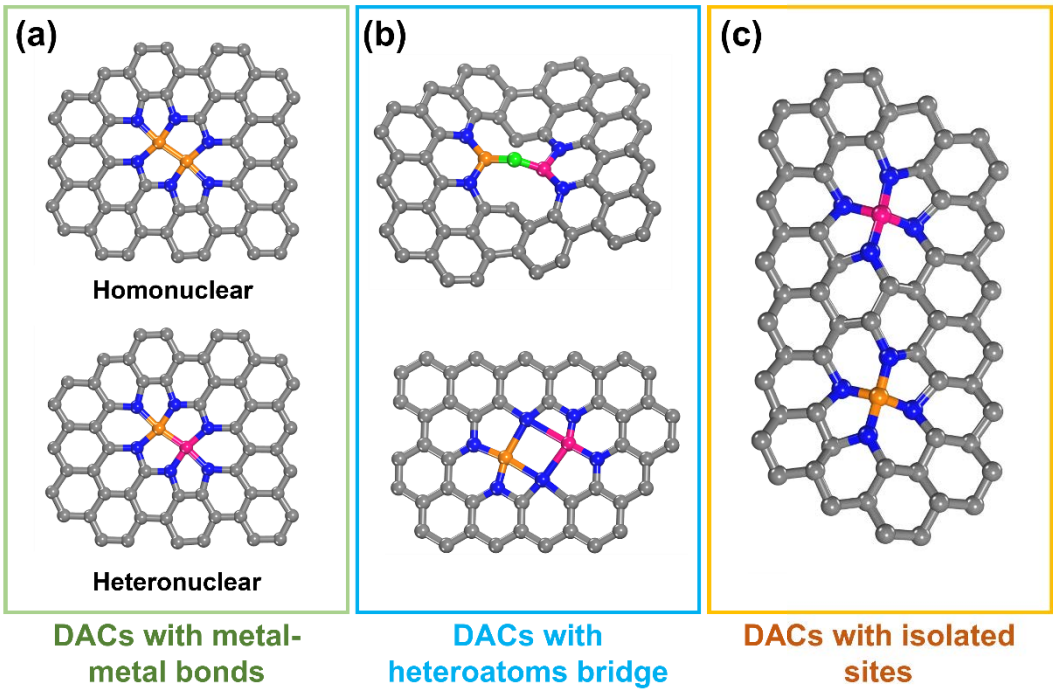

Figure 2.14. Illustration of atomic environment of DACs.

Homonuclear DACs with the same metal atoms provide a facile path for regulating the geometrical and electronic configuration of M-N-C catalysts. For example, a Ni dual-atom catalyst fabricated by Zhang et al. through a top-down strategy delivered high electrocatalytic CO_2RR [88]. Compared with homonuclear DACs, heteronuclear DACs with strong binary metal interactions can have a synergistic effect which further enhances reaction activity and selectivity. The heterometallic bonding results in a structural distortion and charge polarization which can be beneficial for tuning the energetics of reaction intermediates. Hou and co-workers [89] found that DACs bridged with O feature lower the reaction barrier of *COOH formation and suppressed HER (**Figure 2.15**). The InNi DS/NC catalyst with synergistic indium-nickel dual sites bridged by an axial oxygen atom (O-In-N_6-Ni moiety) exhibited excellent activity and selectivity in CO_2RR, with a FE_{CO} >90% over a wide potential range.

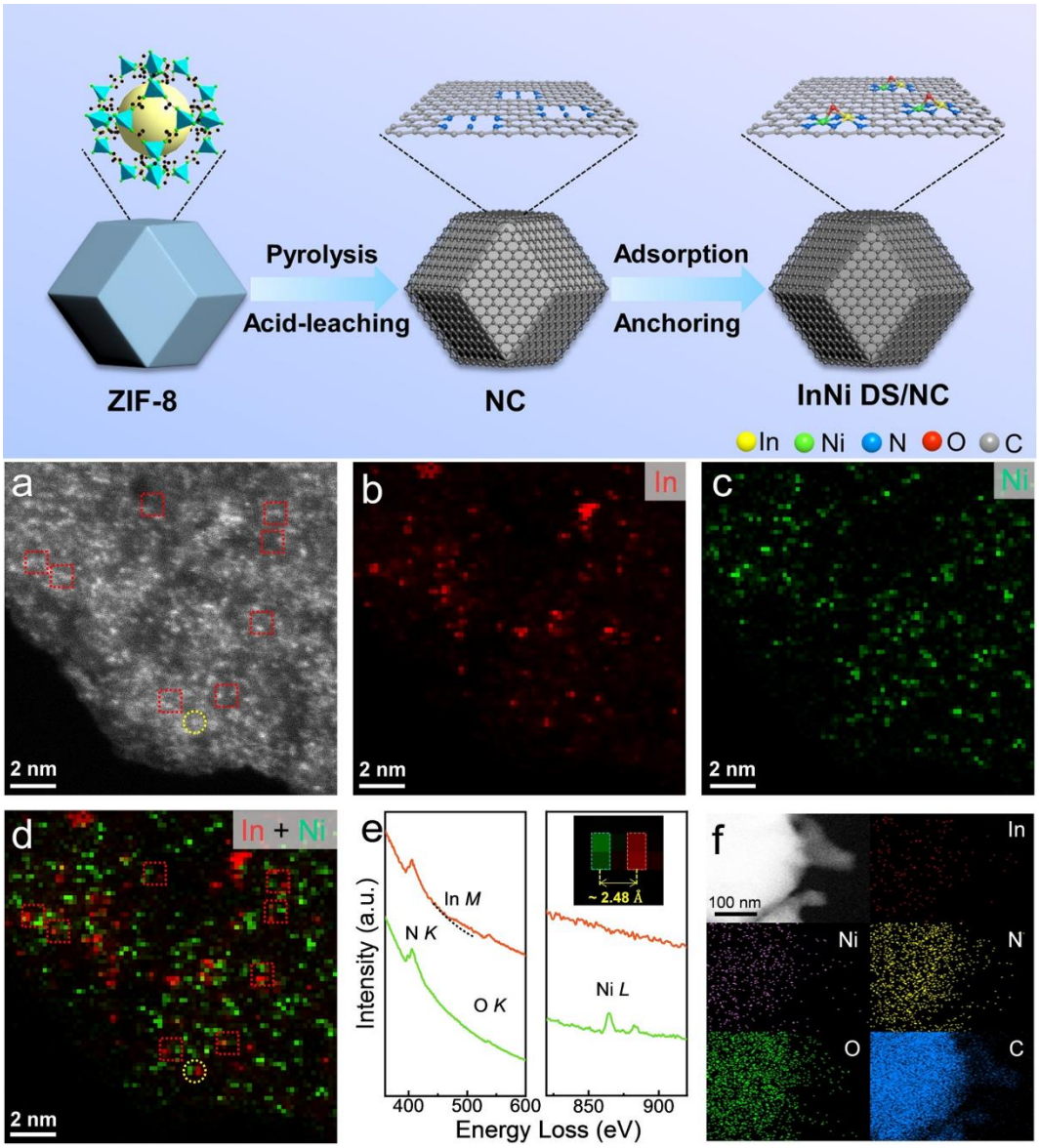

Figure 2.15. Schematic illustration of synthesis of InNi DS/NC. a) AC HAADF-STEM image of InNi DS/NC. Atomic-resolution EELS mapping of b) In, c) Ni and d) their overlap. e) EELS spectra extracted from the position highlighted in the yellow circle in (d), (inset: the enlarged image in the yellow circle in (d)). f) HAADF-STEM image and corresponding EDS mapping [89].

2.3. Summary and gap identification

Electrochemical water splitting and CO_2 reduction are promising technologies for developing clean, low-carbon, and sustainable energy system. But there are still

challenges in term of cost and efficiency, which greatly limit their commercialization. Hence, developing advanced and efficient catalysts for water and CO_2 electrocatalysis is of great scientific and industrial significance. As described above, TM-based materials are promising candidates and various strategies were proposed for the design and syntheses of TM-based electrocatalysts. From recent attempts of using TM-based materials (compounds, heterostructures, nanoclusters, single atom sites) as HER, OER, and CO_2RR electrocatalysts, it is now understood that structural, compositional, and atomic engineering of TM-based materials can be effective in improving electrochemical water dissociation and CO_2 reduction. However, facile syntheses, precise control over geometric/electronic structures, and the underlying structure-activity relationship of TM-based catalysts still require further research.

2.4. Aims and objectives

This Ph.D. project aims to develop MOF-derived high-performance TM-based electrocatalysts with well-desired composition and structure for water splitting and CO_2RR. The specific objectives are lists below:

1) To design and synthesize MOF-derived TM-based electrocatalysts featuring tuneable composition and well-defined morphology.

2) To develop innovative strategies to improve the efficiency of MOF-derived TM electrocatalysts, including secondary metal doping, interfacial and atomic engineering, and morphology control.

3) To investigate the structure-activity relationship of these MOF-derivatives TM-based catalysts.

CHAPTER 3 Experimental details

3.1. Chemicals

Table 3.1 Reagents used in the experiments.

Reagents	Formula	Grade	Manufacturer
Potassium trioxalatoferrate (III) trihydrate	$K_3[Fe(C_2O_4)_3]$	99%	Macklin
Zinc acetate dihydrate	$Zn(OAc)_2 \cdot 2H_2O$	AR	Sinopharm Chemical Reagent Co. Ltd.
Ferric nitrate nonahydrate	$Fe(NO_3)_3 \cdot 9H_2O$	AR	
iron (III) chloride hexahydrate	$FeCl_3 \cdot 6H_2O$	AR	
Cobalt nitrate hexahydrate	$Co(NO_3)_2 \cdot 6H_2O$	AR	
Potassium hydroxide	KOH	85%	
Sodium hydroxide	NaOH	96%	
Potassium bicarbonate	$KHCO_3$	95%	
Sodium carbonate	Na_2CO_3	AR	
Methanol	MeOH	AR	
Ethanol	EtOH	AR	
Ethylene glycol	EG	AR	
Hydrochloric acid	HCl	37%	
2-Methylimidazole		AR	Aladdin
Selenium dioxide	SeO_2	AR	
Molybdenum(VI) dioxy Acetylacetonate		AR	
Ruthenium(IV) oxide	RuO_2	RG	Adamas

3.2. Catalyst preparation

The catalyst preparation in Chapter 4–6 mainly involves solvothermal synthesis and thermal annealing. For the thermal annealing, the sample was loaded in a crucible and then heated to the desired temperature in a tube furnace under an Argon flow. The tube furnace by MTI (OTF-1200X-UL) is equipped with a 60 mm OD quartz tube and a pair of stainless-steel vacuum flanges with needle valves & gauges to allow heating samples under vacuum or gas flow. The temperature of this tube furnace is controlled by a high-precision digital controller which provides 30 programmable segments with +/- 1°C accuracy. The max. working temperature is 1200 °C. The specific details of the syntheses of the catalysts are given in each chapter.

3.3. Materials characterization

X-ray diffraction

The crystal structure was characterized by X-ray diffraction (XRD). The powder XRD (PXRD) patterns were collected on a Rikagu-Miniflex 600 diffractometer with Cu Kα radiation (40 kV, 30 mA). The crystal structures of the synthesized materials are analyzed by matching the recorded XRD patterns with the standard reference in the Joint Committee on Powder Diffraction Standards (JCPDS) database.

Scanning electron microscopy

Scanning electron microscopes (SEMs) are commonly used to image samples with a resolution down to the nanometer scale. The characterization of morphology and chemical composition was conducted on a Zeiss Sigma 300 instrument equipped with energy dispersive X-ray spectroscopy (EDS).

Transmission electron microscopy

Transmission electron microscopy (TEM) was conducted using a Talos-F200X instrument. The powders were dispersed in ethanol by sonication, followed by dropping 20 μL of the dispersion on a 300-mesh copper grid coated with lacey carbon for TEM analysis. TEM studies yield more information on the nanostructure than SEM.

Raman spectroscopy

Raman spectroscopy was used to probe specific vibrational information related to chemical structure. In this study, Raman spectroscopy analysis was performed to provide insight information about the chemical bond, surface reconstruction, as well as the carbon species of the catalyst using a 532 nm laser source.

N_2 sorption-desorption measurement

Brunauer-Emmer-Teller (BET) analysis is adopted to characterize the surface area of the as-synthesized materials, which can also provide important information such as pore sizes, surface areas, pore volumes. A BELSORP Max analyzer was used to perform the BET measurements.

Fourier transform infrared spectroscopy (FTIR)

Infrared spectroscopy analysis was carried out on a VERTEX 70v compact Fourier transform infrared (FTIR) spectrometer. Before data collection, the samples were grinded into fine powders and then put on the detector directly. The FTIR spectra were collected in a spectral range of 4000-400 cm^{-1}.

Nuclear magnetic resonance (NMR) spectroscopy

Liquid products (formate) were quantified using ^{1}H nuclear magnetic resonance (NMR) spectroscopy (Chapter 4). In a typical analysis, a mixture of 500 μL of the electrolyte and 100 μL of 10 mM DMSO (used as internal standard) D_2O solution was analyzed. The ^{1}H spectra were obtained by using a pre-saturation method to suppress the water peak.

Gas chromatography

During CO_2RR (Chapter 6), gas products (CO and H_2) were quantified using gas chromatography (Agilent 7820A), which was equipped with a thermal conductivity detector (TCD) and flame ionization detector (FID). Ar was used as the carrier gas.

Faraday efficiencies (FE) of CO and H_2 were calculated based on the following equation: FE = mnF/Q, where n is the number of electrons required for the product, m is the molar weight of the product, F represents Faraday constant (96485 C mol^{-1}), and the Q corresponds to the amount of cumulative charge during CO_2 reduction.

3.4. Electrochemical studies

HER and OER measurements of electrocatalysts were conducted in a typical three-electrode cell using a CHI-760E electrochemical workstation. Carbon rod and saturated Ag/AgCl electrode were applied as counter electrode and reference electrode, respectively.

3.4.1. Preparation of the working electrode

The catalyst ink was prepared by dispersing 10 mg of catalyst in a mixture of H_2O (200 μL), EtOH (700 μL), DMF (50 μL), and Nafion solution (50 μL, 5 wt%), followed by ultrasonication for 1 h to form a homogeneous suspension. Then, 100-200 μL of the

catalyst ink was deposited on a piece of carbon paper (CP) or nickel form (NF) substrate with a size of 1.0 × 1.0 cm^2 to obtain a loading of 1-2 mg cm^{-2}.

3.4.2. Cyclic voltammetry

Cyclic voltammetry (CV) is an effective electrochemical technique commonly employed to investigate the catalytic reactions including both the reduction and oxidation processes. Additionally, CV measurement is a well-established technique to measure the double-layer capacitance (C_{dl}) to calculate the electrochemically active surface area (ECSA) of a catalyst. In a typical CV experiment, the working electrode potential is ramped linearly versus time. Before performing the electrochemical measurements, CV scan was carried out to optimize the electrocatalysts at 100 mV s^{-1}.

3.4.3. Linear sweep voltammetry

Similar to CV, linear sweep voltammetry (LSV) is a powerful electrochemical technique, in which the voltage is increased from a low value to a high one. LSV curves are recorded for HER, OER and EGOR with 90% iR-compensation at a scan rate of 5 mV s^{-1}, which are commonly adopted to evaluate the catalyst performance. All the measured potentials versus Ag/AgCl were normalized to reversible hydrogen electrode (RHE) by the following equation: $E_{RHE} = E_{Ag/AgCl} + 0.059 \times pH + 0.197$ (V). The overpotential (η) of OER was calculated according to the following formula: $\eta = E_{RHE} - 1.23$ V. Overall water splitting test was performed in two-electrode systems.

3.4.4. Other measurements

The electrochemical impedance spectroscopy (EIS) was measured from 10^5 to 0.01 Hz with an amplitude of 5 mV. Additionally, the long-term stability was tested by the chronoamperometry (CP) method at a constant current density. Then CV tests were

performed in the non-Faradaic region at different sweeping rates to estimate the double-layer capacitance (C_{dl}).

3.4.5. Computational details

In this thesis, DFT calculations were conducted using the Vienna ab initio simulation package (VASP) [90, 91]. The projector-augmented wave (PAW) method was adopted to describe interactions between ions and valence electrons [92]. The generalized gradient approximation (GGA) in the form of Perdew, Burke, Ernzerhof (PBE) was employed to describe the exchange-correlation effects [93]. The plane-wave basis set along with a kinetic cut-off energy was 400 eV. The Brillouin zones were sampled with 3 × 3 × 1 Monkhorst-Pack meshes. The structures were completely relaxed until the maximum force on each atom was smaller than –0.02 eV/Å and 10^{-5} eV. At least 20 Å of vacuum space was inserted along the z direction to avoid any interaction between periodically repeating images. The van der Waals interaction was considered using the DFT-D3 method of Grimme.

The Gibbs free energy (ΔG) was described as follows:

$$\Delta G = \Delta E + \Delta E_{ZPE} - T\Delta S \quad (1)$$

ΔE is the reaction energy from the density functional theory calculations. ΔE_{ZPE} and ΔS are the zero-point energy difference and the entropy difference between the products and the reactants at room temperature, respectively.

CHAPTER 4 MOF-Derived Hollow and Yolk-Shell Nanocages for Water Oxidation and Selective Ethylene Glycol Reformation

This chapter has been extracted from the published paper of M. Huang, C. Cao, L. Liu, W. Wei, Q. -L. Zhu, Z. Huang, "Controlled synthesis of MOF-derived hollow and yolk–shell nanocages for improved water oxidation and selective ethylene glycol reformation", eScience, accepted, 2023.

4.1. Introduction

Structural engineering has been regarded as an effective path to improve the electrochemical performance of electrode materials [94]. Hollow and yolk-shell nanostructures have demonstrated advantages as functional materials for electrocatalysis owing to their unique structures and inherent physical and chemical properties, such as large surface areas, rich cavities, low mass density, and reduced diffusion length for mass and charge transport [95, 96]. Particularly, the yolk-shell nanostructures possessing hollow shells and interior cores feature multiple structural merits, incredibly attractive for electrocatalysis. As a result, numerous synthetic strategies have been developed to fabricate hollow frame-like and yolk-shell nanoarchitectures [16, 18, 97, 98]. For instance, the most efficient approach to prepare such nanostructures is the template-assisted method, in which the sacrificial templates can be transformed into various targeted products through careful etching and/or pyrolysis [99, 100]. Owing to their accessible porous crystalline structures enabling high mass transport, MOFs often serve as the

starting sacrificial templates for synthesizing high-performance hollow and yolk-shell nanostructured electrocatalysts [101]. Most pristine MOFs cannot be used in practical energy conversion and storage applications because of their intrinsically low electrical conductivity and poor structural stability [102, 103]. This limitation can be overcome by converting MOFs to diverse derivatives (e.g., LDHs, carbonaceous materials, and metal oxides) with more beneficial properties and nanostructures while preserving their high porosity [25, 42].

MOF-derived LDHs, particularly the Co-LDHs, have been proven to be effective for OER [104, 105]. However, the performance is still far from satisfactory for practical water electrolysis due to the poor intrinsic activity and insufficient active sites [106]. Based on previous works, the introduction of foreign metal atoms into Co-LDHs can enhance the OER performance, since the synergistic interactions between Co and foreign metals can tune the local coordination environment and electronic structure of Co sites, thereby boosting the intrinsic activity [24, 37, 107-109]. For example, Wang's research group reported that incorporating Zn^{2+} ions into CoOOH gave rise to oxygen non-bonding states with different local configurations and changed the OER routes. $Zn_{0.2}Co_{0.8}OOH$ with Zn–O2–Co–O2–Zn configuration showed much better catalytic activity than the corresponding monometallic component [37]. However, obtaining MOF-derived hollow and yolk-shell LDH catalysts with optimized compositions is still challenging due to complex synthetic procedures and different precipitation kinetics between divalent and trivalent metal cations [34].

It is well known that the sluggish kinetics of the anodic OER makes it a bottleneck reaction in water electrolysis [1, 110]. In addition, OER is an energy-intensive process and only produces a low-value product (*i.e.*, O_2). Alternatively, replacing OER with thermodynamically favourable small organic molecule oxidation reactions is attractive to

reduce energy input while simultaneously producing value-added products, which has been verified [111-116]. Notably, Co-based LDH electrocatalysts have shown high activity for the electro-reforming of some organic fuels. For example, with cobalt hydroxide@hydroxysulfide nanosheets on carbon paper ($Co(OH)_2$@HOS/CP) as the working electrode, methanol can be selectively converted into formate with Faradaic efficiency (FE) as high as ~100% [117]. Further replacing OER with methanol oxidation reaction (MOR) in a hybrid water electrolysis system enables the simultaneous production of H_2 and formate with less energy input. Encouraged by these findings, it is desirable to construct MOF-derived Co-based LDHs with controlled compositions and morphologies as a bifunctional electrocatalyst for water oxidation and selective ethylene glycol (EG) reforming for enhanced H_2 production.

Herein, an etching-doping reconstruction strategy was developed to synthesize oxalate-decorated hierarchically nanostructured CoFe-LDHs by using a Co-based MOF (ZIF-67) as the precursor. Through adjusting the reconstruction degree under various conditions, hollow CoFe-LDH nanosheets (NSs) assembled nanocages (h-CoFe-LDH NCs) and yolk-shell ZIF@CoFe-LDH nanocages (ys-ZIF@CoFe-LDH NCs) were readily synthesized. Control experiments revealed that the strong affinity between oxalate groups and Co^{2+}/Fe^{3+} ions is the key to the formation of the unique hierarchical nanostructures. Owing to the strong synergistic interactions between Co and Fe sites, as well as the oxalate groups enlarging the layer spacing of LDHs, the as-prepared h-CoFe-LDH NCs and ys-ZIF@CoFe-LDH NCs exhibited excellent electrochemical performance for OER and ethylene glycol oxidation reaction (EGOR), respectively. Further assembling ys-ZIF@CoFe-LDH NCs as the anode into an EGOR-coupled hybrid water electrolysis system can not only reduce energy input but also produce formate with high Faradaic efficiency.

4.2. Experimental section

4.2.1. Catalyst synthesis

Synthesis of ZIF-67 nanocrystals. Co-based MOF precursor (ZIF-67) was prepared via the solvothermal assembly of Co^{2+} and 2-methylimidazole ligand. Typically, 2.91 g of $Co(NO_3)_2 \cdot 6H_2O$ and 3.28 g of 2-methylimidazole were dissolved in 200 mL of methanol, respectively. Then, the two solutions were mixed under vigorous stirring. After reacting for 24 h, the purple precipitate was filtered, washed 3 times with methanol, and then finally vacuum-dried.

Synthesis of oxalate-modified yolk-shelled ZIF@CoFe-LDH NCs and hollow CoFe-LDH NCs. Oxalate-modified hollow h-CoFe-LDHs NCs were synthesized by using ZIF-67 as the template. Typically, 100 mg of ZIF-67 was first ultrasonically dispersed in 20 mL of ethanol. Then 20 mL of $K_3[Fe(C_2O_4)_3]$ aqueous solution (1.5 mg mL^{-1}) was slowly added. The mixture was then refluxed at 85 ℃ for 60 min. After cooling to room temperature, the product was collected by centrifugation, washed with ethanol 3 times, and dried at 60 ℃ for 10 hours. To obtain the oxalate-modified yolk-shell ys-ZIF@CoFe-LDH NCs, the reaction was aged at room temperature for 30 min. Finally, the product was collected by centrifugation, washed with ethanol several times, and dried at 60 ℃ overnight.

Synthesis of hollow h-Co-LDH NCs. Hollow h-Co-LDH NCs were prepared similarly to that of h-CoFe-LDH NCs. Typically, 100 mg of ZIF-67 was dispersed in 25 mL of ethanol containing 180 mg of $Co(NO_3)_2 \cdot 6H_2O$. Then the mixture was refluxed at 85 ℃ for 60 min. Finally, the collected product was washed with ethanol several times and dried at 60 ℃ overnight.

Synthesis of typical CoFe-LDH NSs. Typical CoFe-LDH nanosheets (t-CoFe-LDH NSs) were prepared as follows. 5.25 mmol of $Co(NO_3)_2 \cdot 6H_2O$ and 0.75 mmol of $Fe(NO_3)_3 \cdot 9H_2O$ were dissolved in 40 mL deionized water to form solution A. 3 mmol of Na_2CO_3 and 21 mmol of NaOH were dissolved in 40 mL of deionized water to form solution B. Then, solutions A and B were simultaneously added dropwise into a beaker containing 80 mL of deionized water until the pH of the final solution reached 8.5. After stirring for 24 h, the precipitates were collected and dried at 60 °C overnight.

4.3. Results and discussion

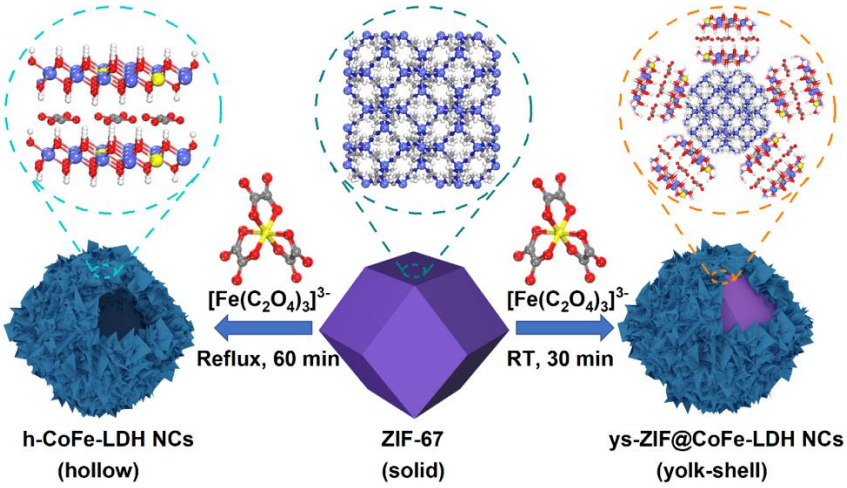

Figure 4.1. Schematic illustration of the fabrication of h-CoFe-LDH NCs and ys-ZIF@CoFe-LDH NCs.

As shown in **Figure 4.1**, the hierarchical CoFe-LDH based nanocages with two different nanostructures can be prepared by using an etching-doping reconstruction strategy, starting from the Co-MOF (ZIF-67) precursor. The ZIF-67 nanocrystals with rhombic dodecahedral morphology were first synthesized as the sacrificial templates via the assembly of Co^{2+} and 2-methylimidazole ligands under ambient conditions **(Figure 4.2)**.

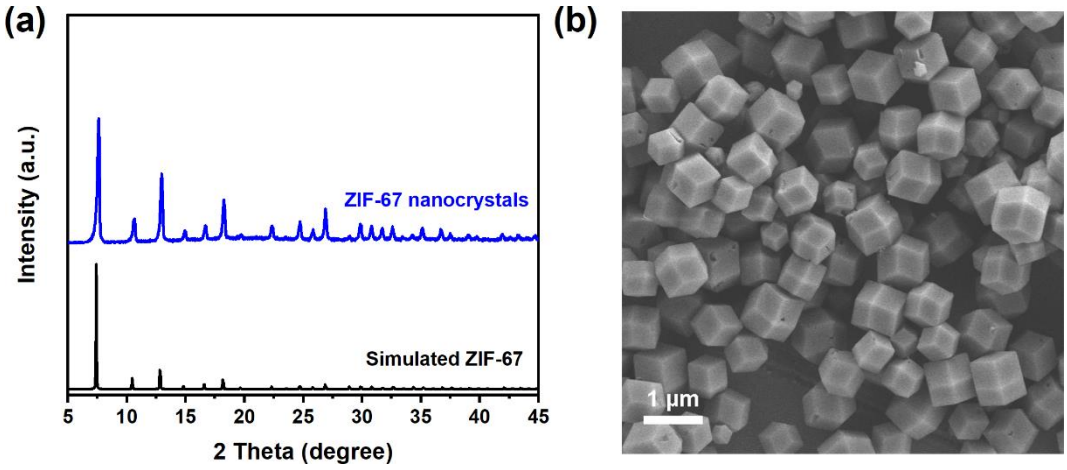

Figure 4.2. (a) PXRD pattern and (b) A SEM image of ZIF-67 nanocrystals.

After the reaction between $K_3[Fe(C_2O_4)_3]$ and ZIF-67 in an ethanol-water solution, hollow h-CoFe-LDH NCs and yolk-shell ys-ZIF@CoFe-LDH NCs were obtained under refluxing and ambient conditions, respectively. During the reconstruction process, the ZIF-67 template was gradually etched by the H^+ generated from the hydrolysis of $[Fe(C_2O_4)_3]^{3-}$ and, meanwhile, the released Fe^{3+} and Co^{2+} coprecipitated with $OH^-/C_2O_4^{2-}$ to form thin CoFe-LDH NSs shell [25]. The reconstruction degree can be readily controlled by adjusting the reaction temperature. Specifically, the low temperature slowed down the etching of ZIF-67, leading to the formation of yolk-shell ys-ZIF@CoFe-LDH NCs, whereas refluxing at a higher temperature led to faster hydrolysis and consequently hollow h-CoFe-LDH NCs.

For h-CoFe-LDH NCs, the diffraction peaks corresponding to ZIF-67 disappeared after reflux treatment (**Figure 4.3a**). Instead, new diffraction peaks located at 8.8, 17.9, and 33.8° were observed, which can be assigned to the typical LDH phase (labelled as t-CoFe-LDH NSs, JCPDS No. 50-0235) but with certain shift, indicating a complete conversion of ZIF to the LDH phase. Compared with t-CoFe-LDH NSs with CO_3^{2-} as the intercalated anions, the diffraction peaks of h-CoFe-LDH NCs indexed as (003) and (006) shifted to lower 2θ values. This is caused by the intercalation of larger $C_2O_4^{2-}$ anions

which leads to the interlayer expansion of the derived CoFe-LDH [118, 119]. In contrast, the PXRD pattern of ys-ZIF@CoFe-LDH NCs is similar to that of pristine ZIF-67 but with weaker peak intensity (**Figure 4.4**), implying that only part of ZIF-67 was converted into CoFe-LDH which has poor crystallinity.

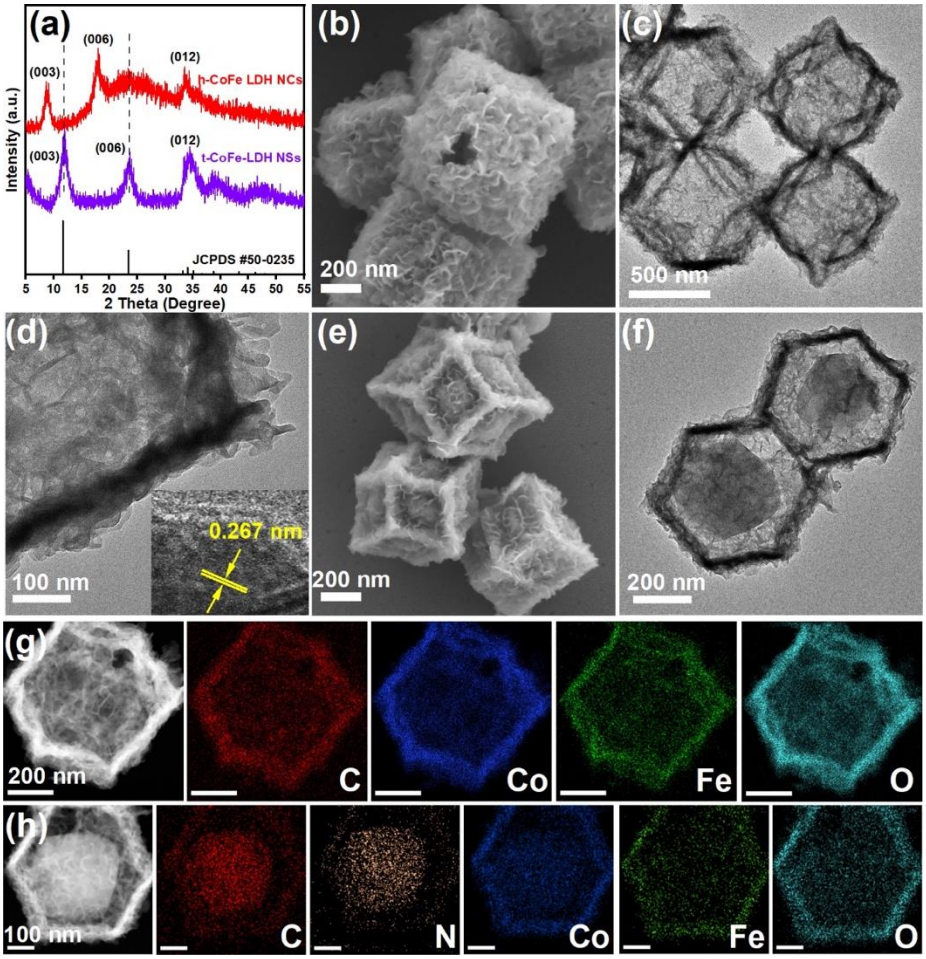

Figure 4.3. (a) PXRD patterns of h-CoFe-LDH NCs and typical CoFe-LDH NSs (t-CoFe-LDH NSs); SEM and TEM images of (b-d) h-CoFe-LDH NCs and (e, f) ys-ZIF@CoFe-LDH NCs; HAADF-STEM and the corresponding EDS elemental mapping images of (g) h-CoFe-LDH NCs and (h) ys-ZIF@CoFe-LDH NCs.

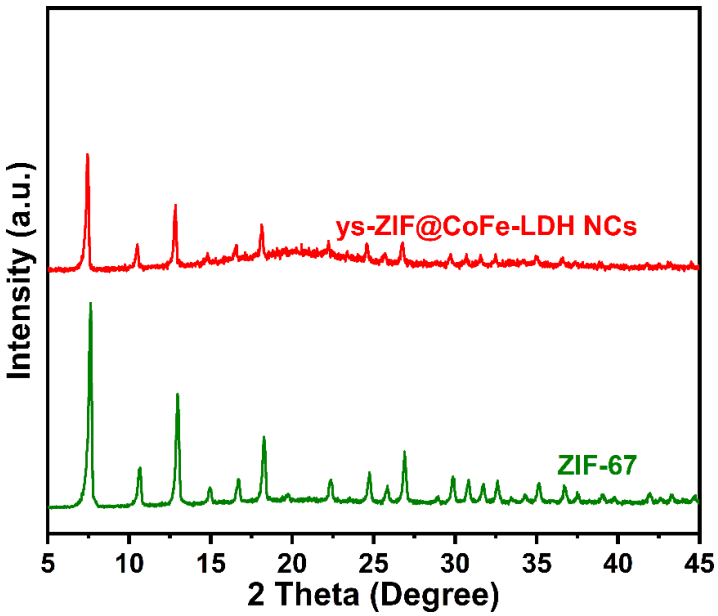

Figure 4.4. PXRD patterns of ZIF-67 and ys-ZIF@CoFe-LDH NCs.

SEM and TEM images show that the as-prepared h-CoFe-LDH NCs inherits the dodecahedral morphology of ZIF-67 and displays a hollow nanocage morphology, while the smooth surfaces of ZIF-67 turned into rough shells composed of randomly oriented nanosheets (**Figure 4.3b, c)**. A lattice spacing of 0.267 nm in the high-resolution TEM (HRTEM) image can be indexed to the (012) plane of LDH **(Figure 4.3d, inset)**. EDS analysis indicates the presence of C, Fe, Co, and O in h-CoFe-LDH NCs with a Co:Fe atomic ratio of ~7.15 **(Figure 4.5)**, which is close to the value of 6.7 obtained from inductively coupled plasma optical emission spectrometry (ICP-OES) analysis.

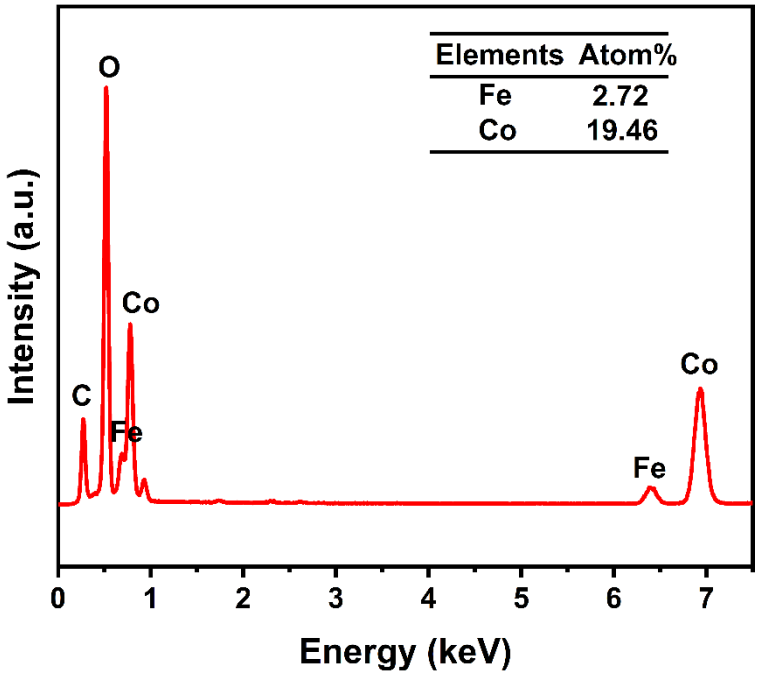

Figure 4.5. EDS analysis of h-CoFe-LDH NCs. Based on the EDS, the atomic ratio of Fe:Co in h-CoFe-LDH NCs is about 1: 7.15.

High-angle annular dark-field scanning TEM (HAADF-STEM) image and the corresponding elemental mapping images show a uniform distribution of C, Co, Fe, and O throughout the hollow nanocages (**Figure 4.3g**). Comparatively, ys-ZIF@CoFe-LDH NCs exhibit an intriguing yolk-shell structure consisting of the CoFe-LDH nanosheet-based shell of ~40 nm in thickness and the maternal ZIF-67 core of ~250 nm (**Figure 4.3e, f**). The CoFe-LDH shells of ys-ZIF@CoFe-LDH NCs are similar to that of h-CoFe-LDH NCs. EDS mapping confirms that the inner core consists of only C, N, and Co, while the outer shell contains primarily Co, Fe, and O (**Figure 4.3h**), further verifying the CoFe-LDH shell and the ZIF-67 core in ys-ZIF@CoFe-LDH NCs. For comparison, t-CoFe-LDH NSs with the same Co:Fe ratio and hollow Co-LDH NCs (h-Co-LDH NCs) were also prepared **(Figure 4.6 and Figure 4.7)**.

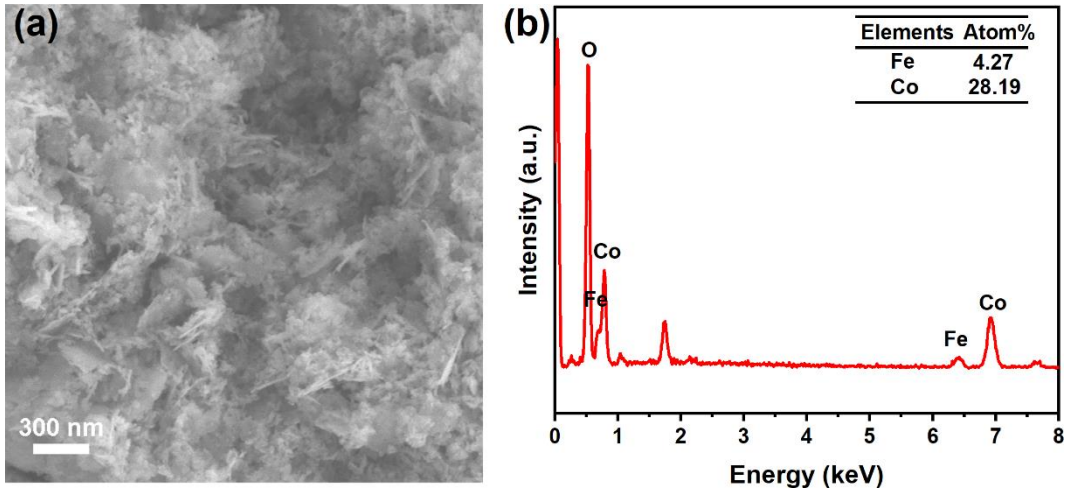

Figure 4.6. (a) A SEM image and (b) corresponding EDS analysis of t-CoFe-LDH NSs. Based on EDS, the atomic ratio of Fe:Co in t-CoFe-LDH NSs is about 1: 6.6, which is similar to that of h-CoFe-LDH NCs.

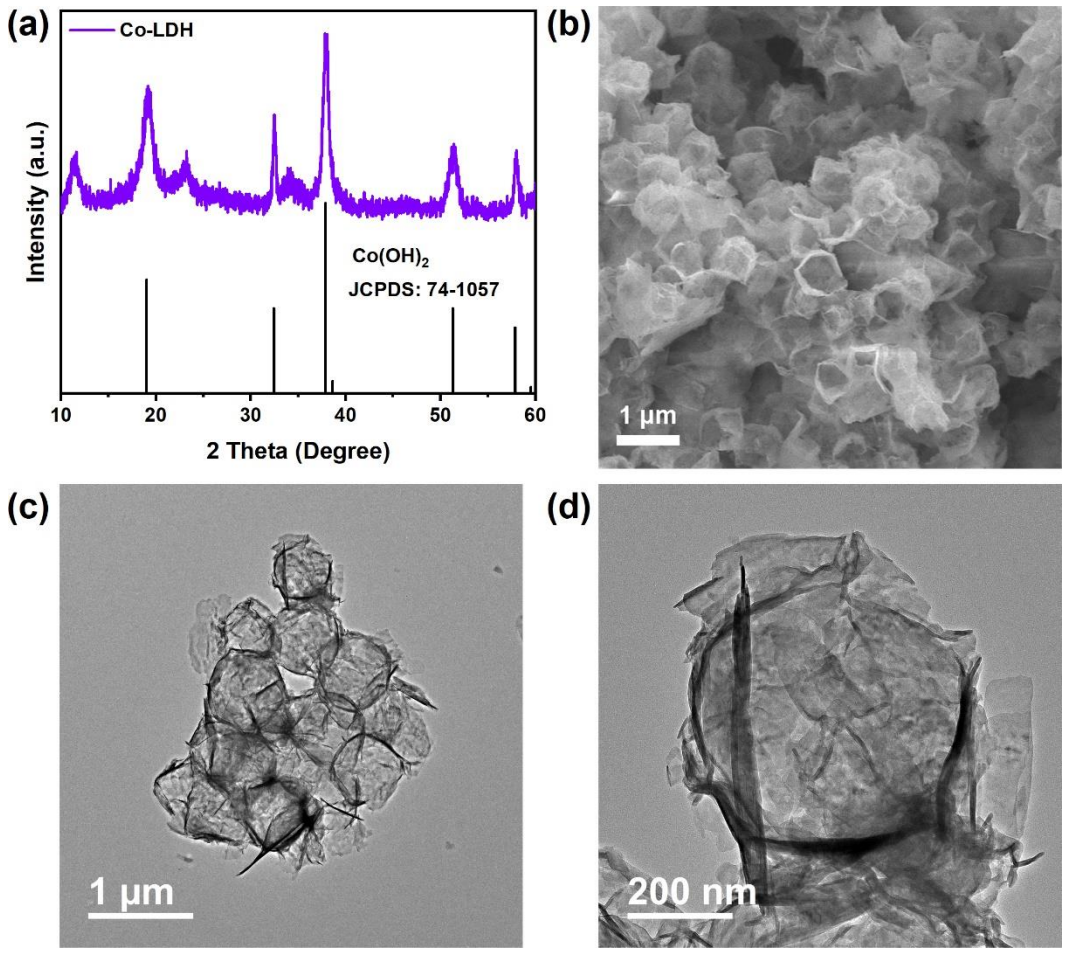

Figure 4.7. (a) PXRD pattern, (b) SEM, and (c-d) TEM images of h-Co-LDH NCs.

The textural properties of h-CoFe-LDH NCs, ys-ZIF@CoFe-LDH NCs, t-CoFe-LDH NSs, and h-Co-LDH NCs were further analyzed by N_2 adsorption-desorption isotherms. As shown in **Figure 4.8a**, both h-CoFe-LDH NCs and h-Co-LDH NCs display type-II isotherms with BET surface areas of 109 and 104 $m^2\ g^{-1}$, respectively, higher than that (65 $m^2\ g^{-1}$) of t-CoFe-LDH NSs, indicating the formation of hollow hierarchical structure with higher surface areas which would provide more accessible active sites for electrochemical reaction. In contrast, ys-ZIF@CoFe-LDH NCs show a type-I isotherm similar to pristine ZIF-67 with a BET surface area of 759 $m^2\ g^{-1}$, suggesting that part of ZIF-67 was preserved.

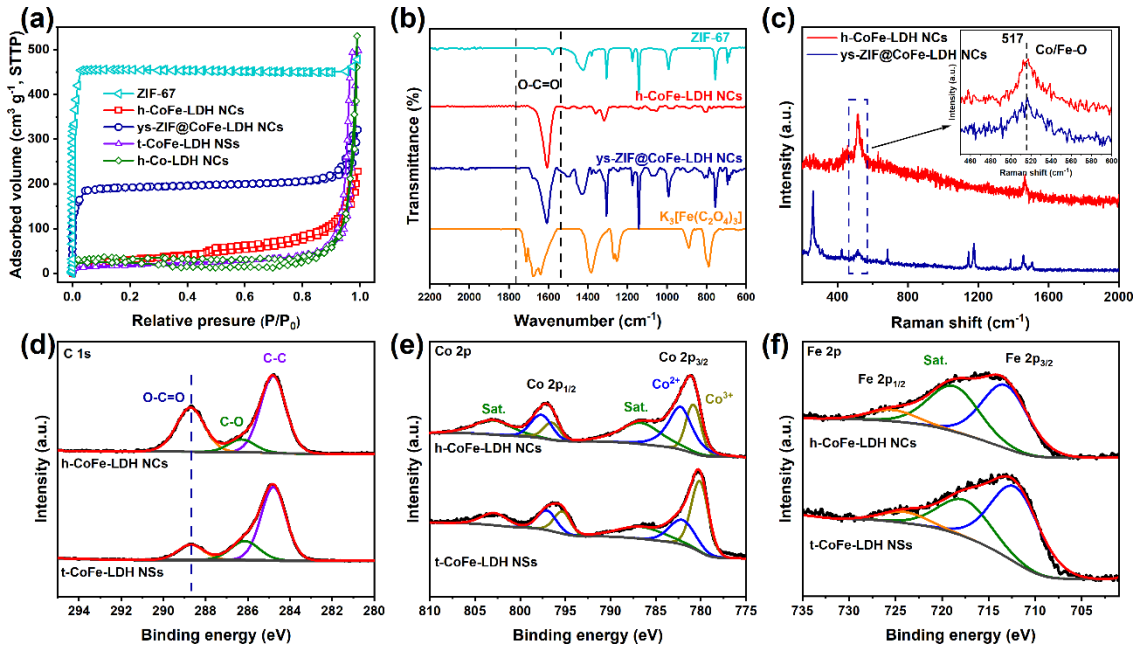

Figure 4.8. (a) N_2 sorption isotherms of ZIF-67, h-CoFe-LDH NC, ys-ZIF@CoFe-LDH NCs, t-CoFe-LDH NSs and h-Co-LDH NCs. (b) FTIR spectra of ZIF-67, h-CoFe-LDH NCs, ys-ZIF@CoFe-LDH NCs and $K_3[Fe(C_2O_4)_3]$. (c) Raman spectra of h-CoFe-LDH NCs and ys-CoFe-LDH NCs. High-resolution XPS spectra of (d) C 1s, (e) Co 2p, and (f) Fe 2p for h-CoFe-LDH NCs and t-CoFe-LDH NSs.

To understand the formation of the nanocage morphology of h-CoFe-LDH NCs and ys-ZIF@CoFe-LDH NCs, the reconstruction-induced agent $K_3[Fe(C_2O_4)_3]$ was replaced

by other Fe salts, such as $FeCl_3 \cdot 6H_2O$ and $Fe(NO_3)_3 \cdot 9H_2O$. In contrast, only polyhedral particles with smooth surfaces and cracked particles were obtained **(Figure 4.9)**, proving that the oxalate group is crucial for the formation of such distinct morphology in h-CoFe-LDH NCs and ys-ZIF@CoFe-LDH NCs.

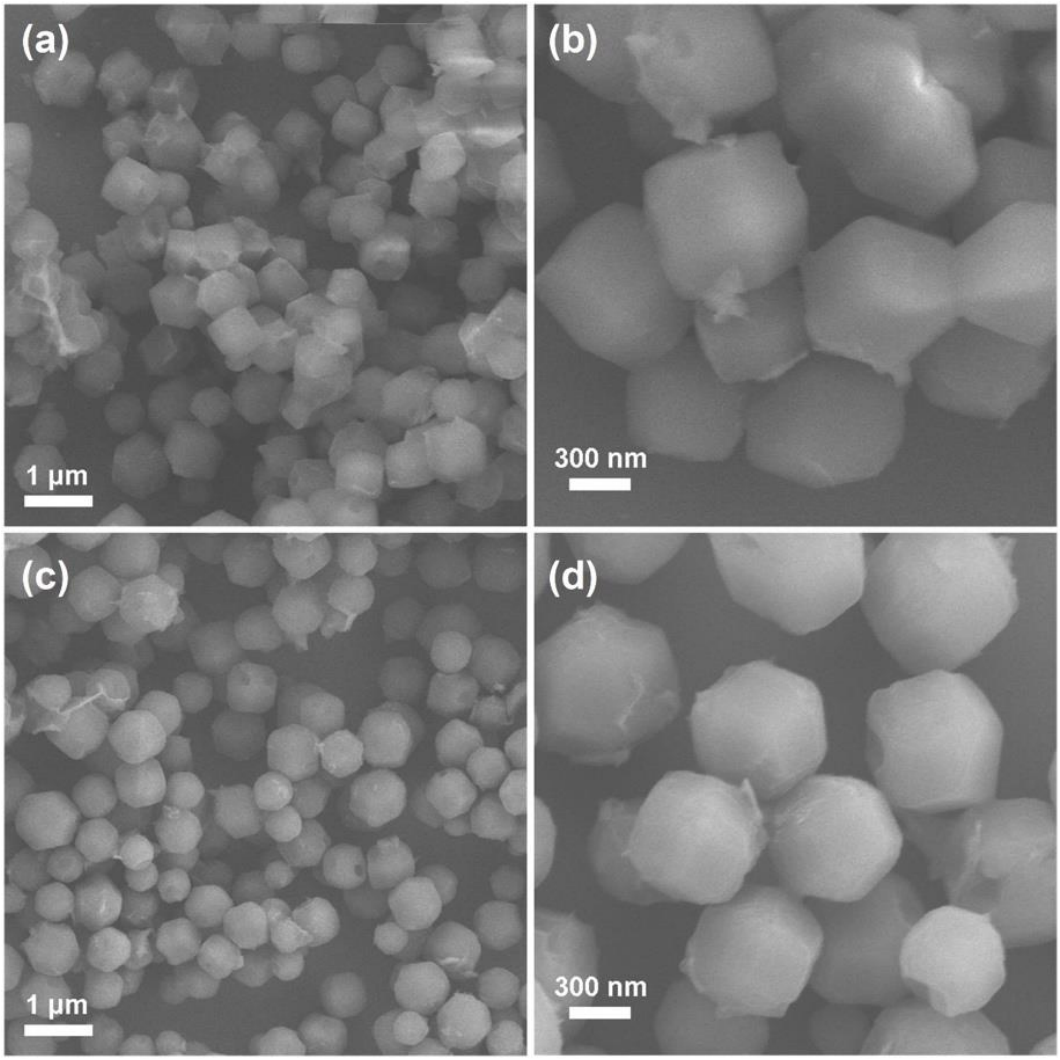

Figure 4.9. SEM images of the resultant CoFe-LDHs prepared by using different Fe salts as the reconstruction agents: (a-b) $FeCl_3 \cdot 6H_2O$, (c-d) $Fe(NO_3)_3 \cdot 9H_2O$.

According to the coordination chemistry theory, the leached Co^{2+} can coordinate with $C_2O_4^{2-}$ to form a stable coordination complex around ZIF-67 particles during the etching process [120]. Hence, the strong affinity between the etchant and the ZIF-67 template enables the fabrication of hierarchical nanocages [97]. In contrast, the

coordination ability of Cl^- and NO_3^- is too weak to form the exterior hierarchical LDH shell that mimics the ZIF-67 template geometry. The added amount of $K_3[Fe(C_2O_4)_3]$ is also important in determining the final morphology. As shown in **Figure 4.10**, a very small amount of $K_3[Fe(C_2O_4)_3]$ could not induce the formation of hollow structures **(Figure 4.10a)**, while too much $K_3[Fe(C_2O_4)_3]$ led to the over-etching of ZIF-67 framework, causing the collapse of the polyhedra **(Figure 4.10d).**

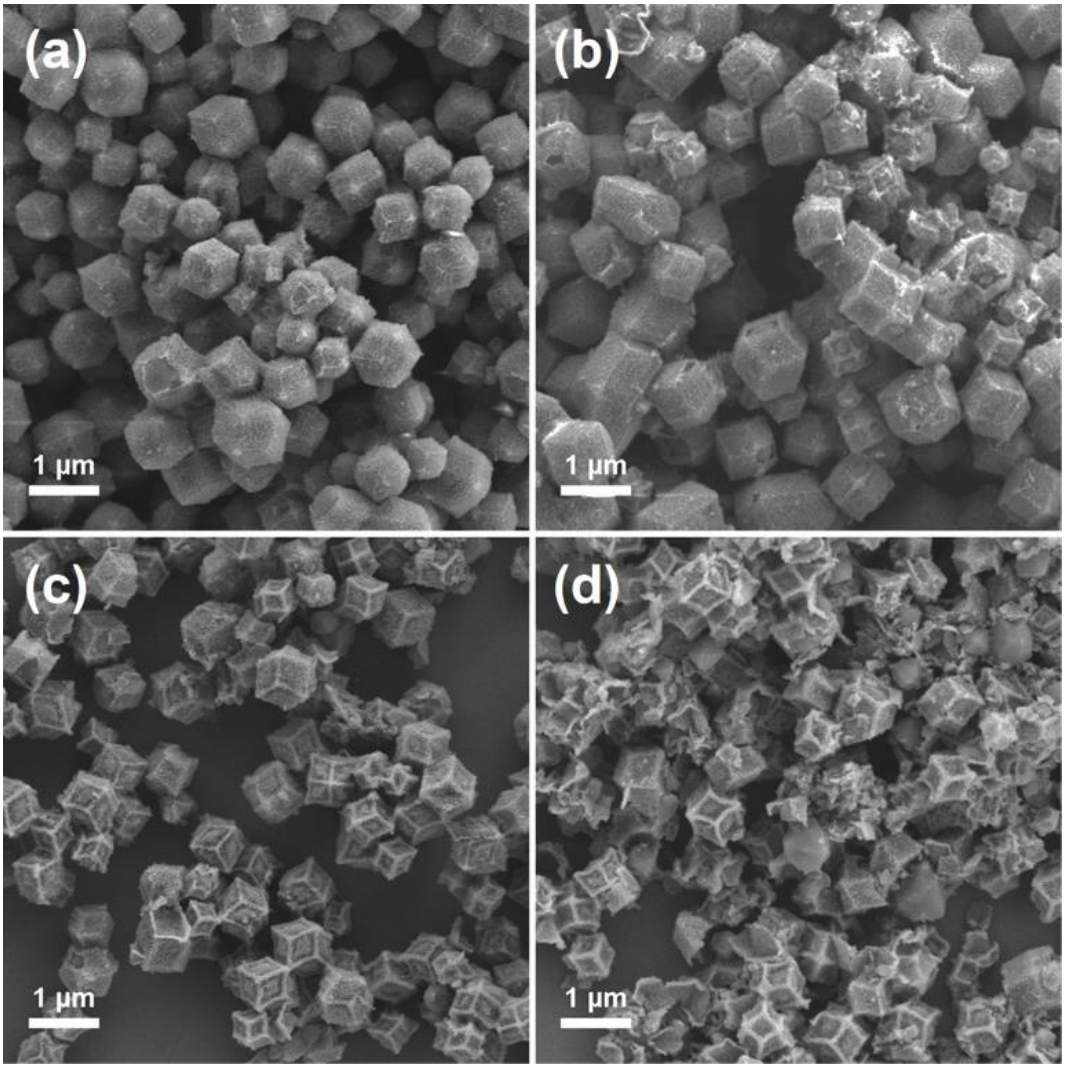

Figure 4.10. SEM images of h-CoFe-LDH NCs prepared using $K_3[Fe(C_2O_4)_3]$ with different concentrations: (a) 0.5 mg mL^{-1}, (b) 1.0 mg mL^{-1}, (c) 1.5 mg mL^{-1}, and (d) 2.5 mg mL^{-1}.

FTIR spectra were also collected. Compared with pristine ZIF-67 and h-Co-LDH NCs **(Figure 4.8b and Figure 4.11)**, a new strong band at around 1610 cm^{-1} was observed in h-CoFe-LDH NCs and ys-ZIF@CoFe-LDH NCs, which is ascribed to the asymmetric C=O stretching vibration [121], indicating that the oxalate groups are intercalated into the CoFe-LDH NSs. According to the previous work, the presence of the hydrophilic oxalate group can improve the adsorption of water molecules on the catalyst surface, thereby enhancing the electrochemical performance [122]. Additionally, Raman spectra were also collected to gain more information on the bonding and chemical structure.

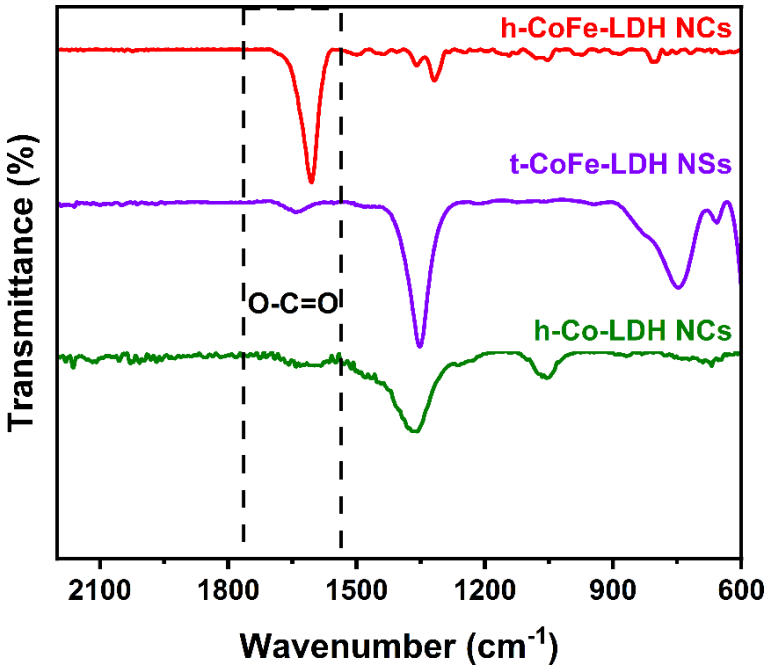

Figure 4.11. FTIR spectra of h-CoFe-LDH NCs, t-CoFe-LDH NSs and h-Co-LDH NCs.

As shown in **Figure 4.8c,** h-CoFe-LDH NCs display two peaks at about 455 and 517 cm^{-1}, which are attributed to Co-OH and Co-O bonds, respectively [123]. In comparison with h-Co-LDH NCs (**Figure 4.12**), the peaks corresponding to Co-O bonds in h-CoFe-LDH NCs and t-CoFe-LDH NSs are red-shifted, indicating the elongation of Co-O bonds, which should be caused by the strong interaction between the Co and Fe sites [124].

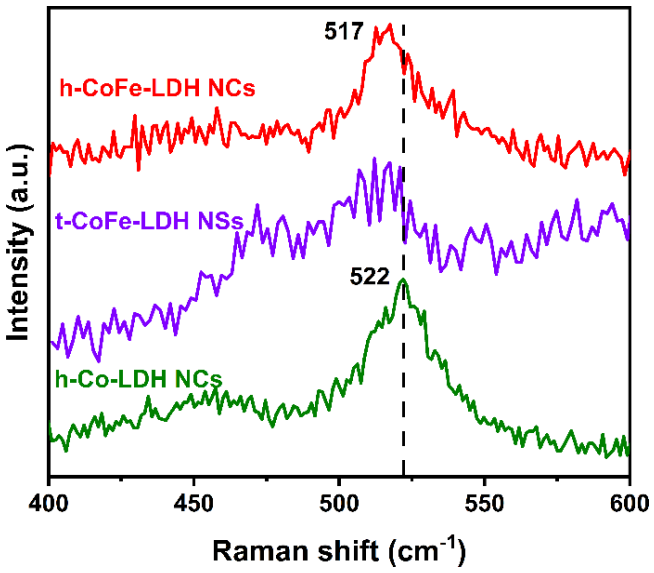

Figure 4.12. Raman spectra of h-CoFe-LDH NCs, t-CoFe-LDH NSs, and h-Co-LDH NCs.

Moreover, the surface compositions and chemical states of the samples were further investigated by XPS. As shown in **Figure 4.13**, the survey spectra of h-CoFe-LDH NCs, ys-ZIF@CoFe-LDH NCs, and t-CoFe-LDH NSs reveal the existence of C, Co, Fe, and O, whereas Fe was not detected in h-Co-LDH NCs. Notably, the signal of N in ys-ZIF@CoFe-LDH NCs is ascribed to the existence of the 2-methylimidazole ligand in the ZIF-67 cores.

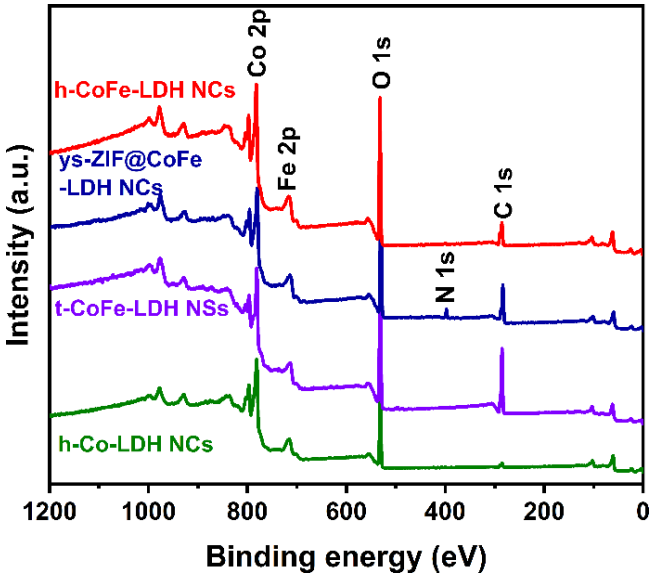

Figure 4.13. XPS survey spectra of h-CoFe-LDH NCs, ys-ZIF@CoFe-LDH NCs, t-CoFe-LDH NSs, and h-Co-LDH NCs.

As observed in **Figure 4.8d**, the C 1s XPS spectrum of h-CoFe-LDH NCs can be deconvoluted into three peaks at 284.8, 285.9, and 288.7 eV, indexed to C-C, C-O, and O-C=O bonds [125], respectively, indicating the presence of oxalate, which is consistent with the PXRD and FTIR results. For Co 2p XPS spectra **(Figure 4.8e)**, the deconvoluted peaks at 780.7 and 782.2 eV are attributed to Co^{3+} and Co^{2+}, respectively [126]. In comparison with h-Co-LDH NCs **(Figure 4.14)**, the peaks of Co 2p in h-CoFe-LDH NCs and ys-ZIF@CoFe-LDH NCs shift to higher energy, demonstrating the interactions between Co and Fe sites, which is consistent with the Raman spectra. The Fe 2p XPS spectra of the samples can be deconvoluted into two broad peaks at 725.3 eV and 713.2 eV, assigned to Fe $2p_{1/2}$ and Fe $2p_{3/2}$ signals, respectively, confirming that the Fe species in CoFe-LDH phase are mostly in the +3 oxidation state [34] **(Figure 4.8f).**

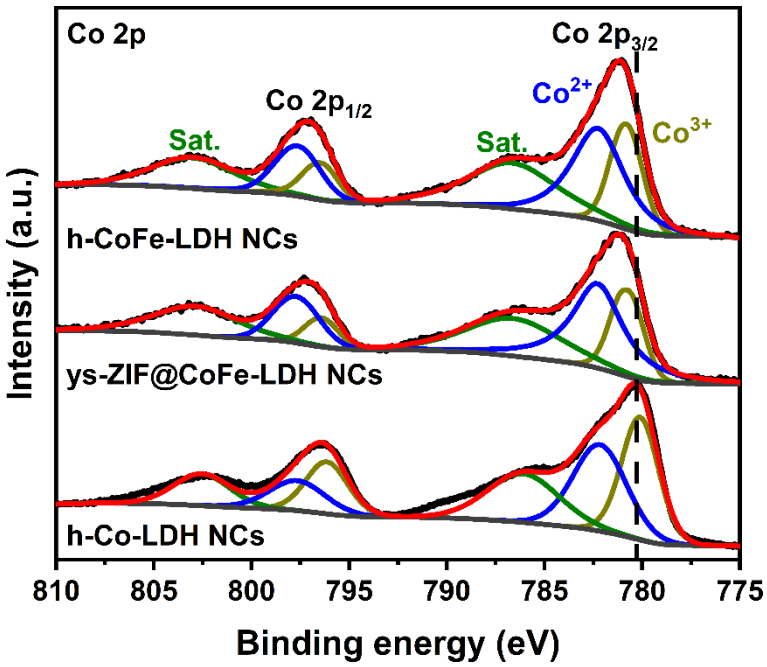

Figure 4.14. High-resolution XPS spectra of Co 2p for h-CoFe-LDH NCs, ys-ZIF@CoFe-LDH NCs and h-Co-LDH NCs.

The electrocatalytic OER performance of the as-prepared catalysts was investigated in 1.0 M KOH. Commercial RuO_2 was used as the reference. All electrocatalysts were loaded on a piece of carbon paper (CP) with a working area of 1.0 cm^2. As shown in **Figure 4.15a**, ZIF-67-derived electrocatalysts displayed an oxidation peak of Co^{2+} to Co^{3+} at around 1.1 V. According to the previous works, high-valence Co species (*i.e.*, Co^{3+}) are the active sites for OER in Co-based electrocatalysts[127].

Based on the relationship between the anodic/cathodic current densities with the scan rates [128] **(Figure 4.16d-f)**, the surface coverage of Co^{2+}/Co^{3+} redox couple was estimated to be 3.04×10^{-7} for h-CoFe-LDH NCs, which is 1.05 and 2.09 times those of ys-ZIF@CoFe-LDH NCs (2.90×10^{-7}) and h-Co-LDH NCs (1.45×10^{-7}), respectively. Moreover, the anodic and cathodic peak current densities for all the as-prepared catalysts are in proportion to the square root of the scan rates **(Figure 4.16g-i)**, suggesting that the Co^{2+}/Co^{3+} redox process is a proton diffusion-controlled process [129]. Notably, the

calculated proton diffusion coefficients (D) value for h-CoFe-LDH NCs (5.93×10^{-7}) is larger than ys-ZIF@CoFe-LDH NCs (5.37×10^{-7}) and h-Co-LDH NCs (1.21×10^{-7}) [130]. It is generally accepted that the larger D value would induce the lower oxidation onset potential, which is beneficial for generating more Co^{3+} species. Consequently, the higher surface coverage of Co^{2+}/Co^{3+} redox couple and faster proton diffusivity of h-CoFe-LDH NCs should promote its OER performance. This is the case, as shown in **Figure 4.15a and b**, since h-CoFe-LDH NCs required overpotentials (η) of only 243 and 278 mV to deliver current densities of 10 and 50 mA cm^{-2}, respectively, which are much lower than those for ys-ZIF@CoFe-LDH NCs (268 and 308 mV), t-CoFe-LDH NSs (292 and 336 mV), h-Co-LDH NCs (288 and 348 mV), and even commercial RuO_2 catalyst (273 and 352 mV), as well as many recently reported Co-based electrocatalysts **(Table 4.1)**. More impressively, h-CoFe-LDH NCs can deliver a current density of about 202 mA cm^{-2} at η = 300 mV, which is much higher compared with ys-ZIF@CoFe-LDH NCs (38 mA cm^{-2}), t-CoFe-LDH NSs (13 mA cm^{-2}), h-Co-LDH NCs (14 mA cm^{-2}), and RuO_2 (21 mA cm^{-2}), further manifesting its excellent OER activity.

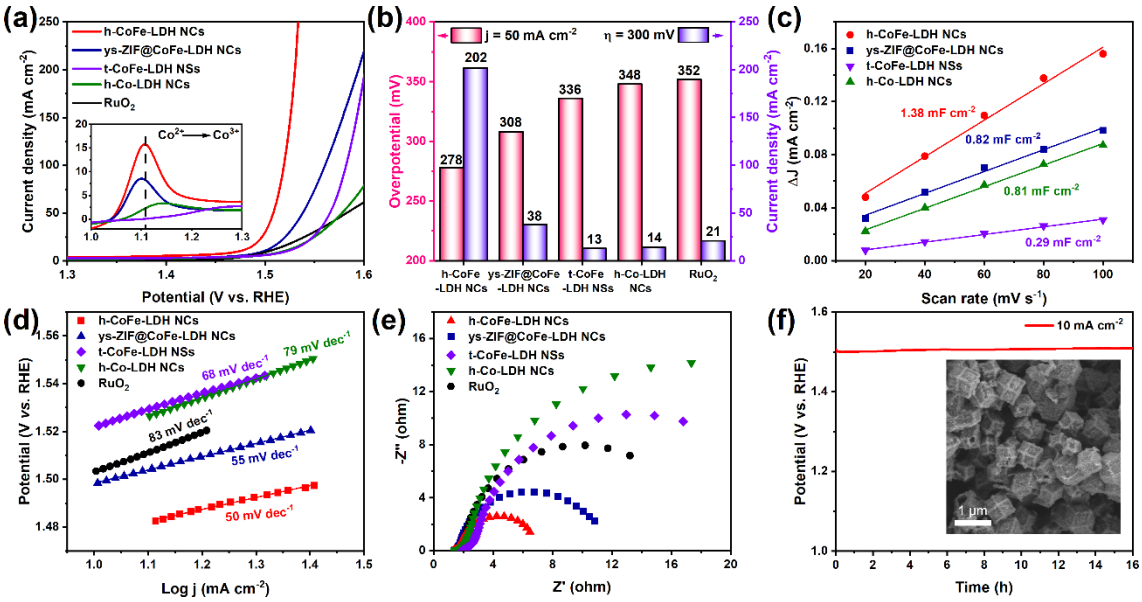

Figure 4.15. OER performance of the catalysts: (a) LSV curves, (b) the comparison of overpotential η at a current density j=50 mA cm^{-2} and the j at η=300 mV; (c) capacitive Δj (=$j_a - j_c$) against scan rates; (d) Tafel plots; (e) EIS plots; (f) long-term stability test for h-CoFe-LDH NCs at j=10 mA cm^{-2}. All the tests were conducted in 1.0 M KOH. Inset in (f) is the SEM image of h-CoFe-LDH NCs after the stability test.

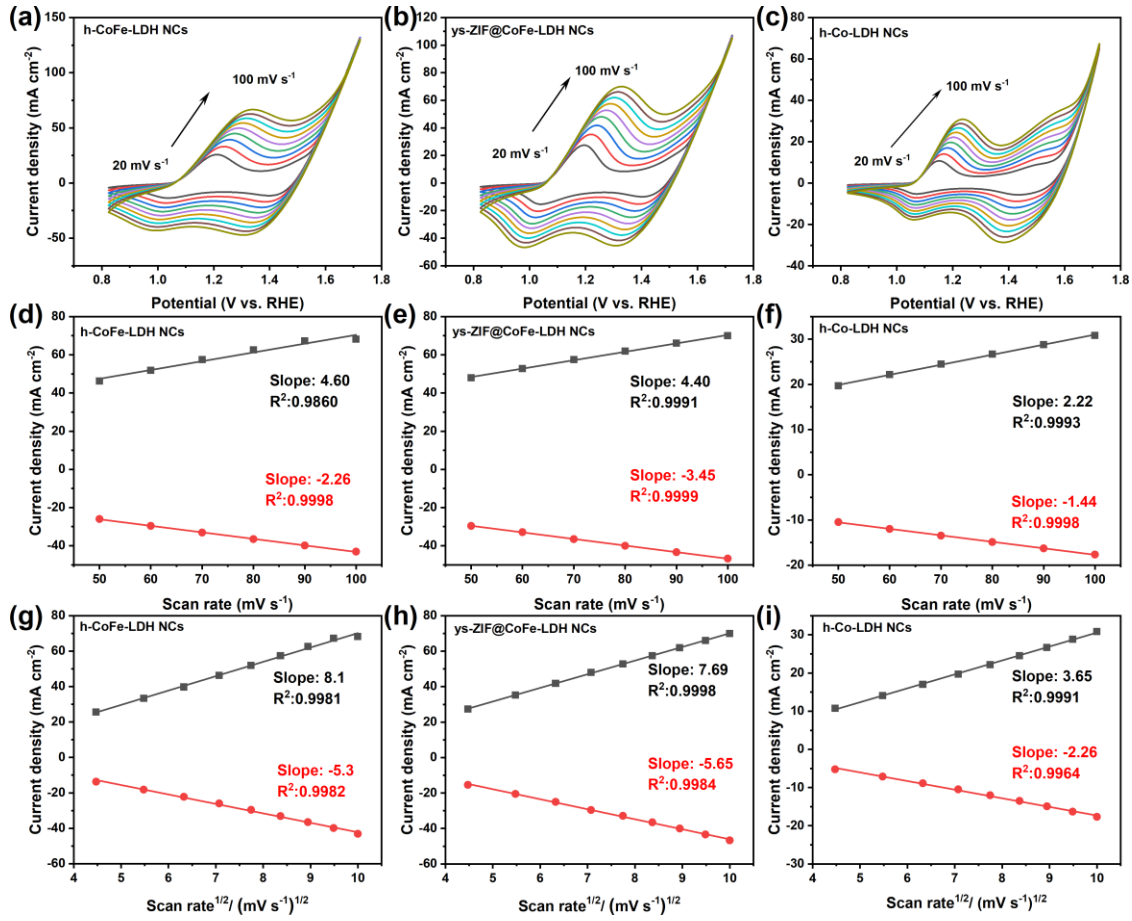

Figure 4.16. CV curves of (a) h-CoFe-LDH NCs, (b) ys-ZIF@CoFe-LDH NCs and (c) h-Co-LDH NCs in 1.0 M KOH at increasing scan rates from 20 to 100 mV s^{-1}. Relationship between the anodic/cathodic current densities with (d-f) the scan rates and (g-i) the square root of the scan rates (red line: cathodic, black line: anodic).

Table 4.1. Comparison of the OER performance of h-CoFe-LDH NCs and other Co-based electrocatalysts reported.

Electrocatalysts	η@10 mA cm^{-2} (mV)	Tafel slope (mV dec^{-1})	Refs.
h-CoFe-LDH NCs	**243**	**50**	**This work**
NiCoP/C	330	96	[27]
Co_3O_4/Co-Fe DSNBs	297	61	[131]
$Ni_{0.6}Co_{1.4}P$ nanocages	300	80	[108]
$Co_{0.85}Se_{1-x}$@C	231	57	[32]
Fe-doped XP@NC800	266	49	[132]
Fe-Co_3O_4	262	43	[39]
Ni-Fe LDH hollow nanoprisms	280	49.4	[35]
CoCu-MOF NBs	271	63.5	[133]
NiCoPO/NC nanosheets	300	94	[134]
Fe-Co-P nanoboxes	269	31	[30]
Co-Fe-O frames	290	62	[100]
Fe1Ni2-BDC	260	42	[135]
CoO-MoO_2 nanocages	312	69	[136]
3D Co(OH)F microspheres	313	52.8	[137]
MOF-Fe/Co(1:2)	238	52	[12]
Ag@$Co(OH)_x$/CC	250	76	[138]
Co/CoP@HOMC	260	151	[139]

To further investigate the OER performance, the ECSAs of the as-prepared electrocatalysts, which are generally proportional to the double-layer capacitances (C_{dl}), were measured based on CV curves at different scan rates **(Figure 4.17)**.

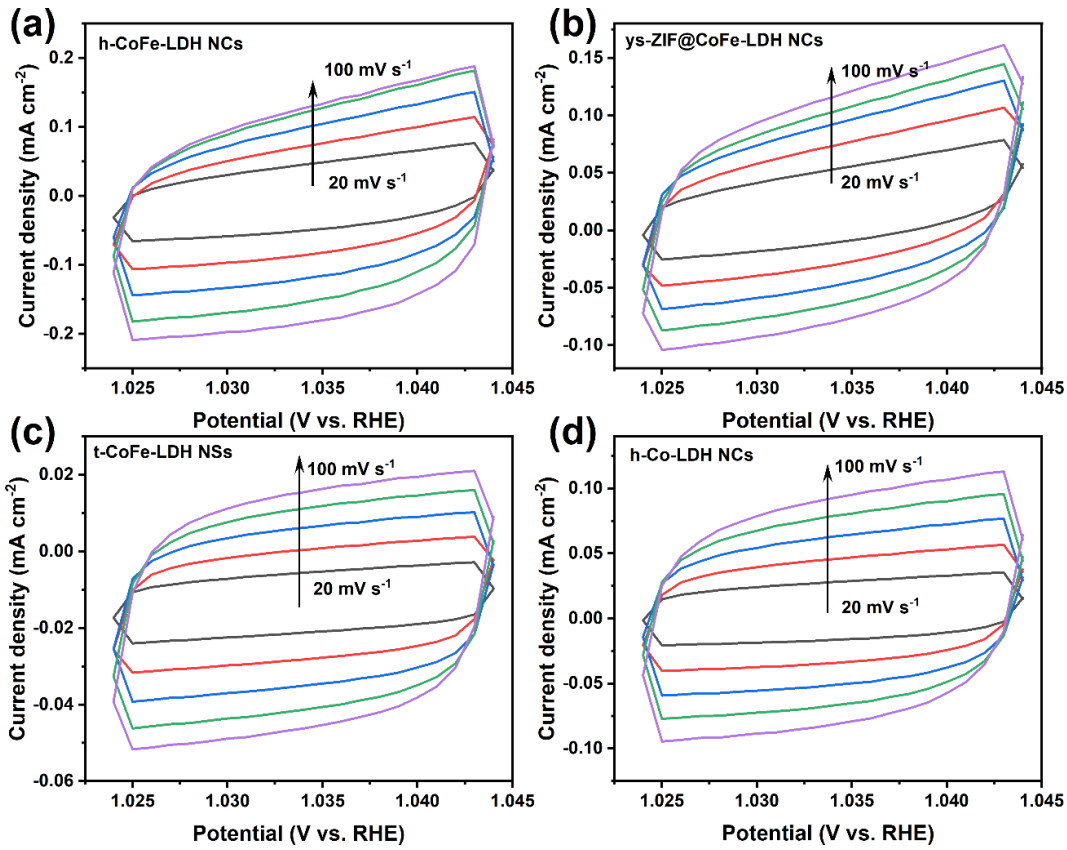

Figure 4.17. CV curves of (a) h-CoFe-LDH NCs, (b) ys-ZIF@CoFe-LDH NCs, (c) t-CoFe-LDH NSs and (d) h-Co-LDH NCs at different scanning rates in 1.0 M KOH.

As shown in **Figure 4.15c**, the measured C_{dl} of h-CoFe-LDH NCs is 1.38 mF cm^{-2}, while the values are only 0.82 mF cm^{-2}, 0.81 mF cm^{-2}, and 0.29 mF cm^{-2} for ys-ZIF@CoFe-LDH NCs, t-CoFe-LDH NSs, and h-Co-LDH NCs, respectively. Moreover, h-CoFe-LDH NCs also exhibited the highest current density normalized by ECSAs among all the samples (**Figure 4.18**).

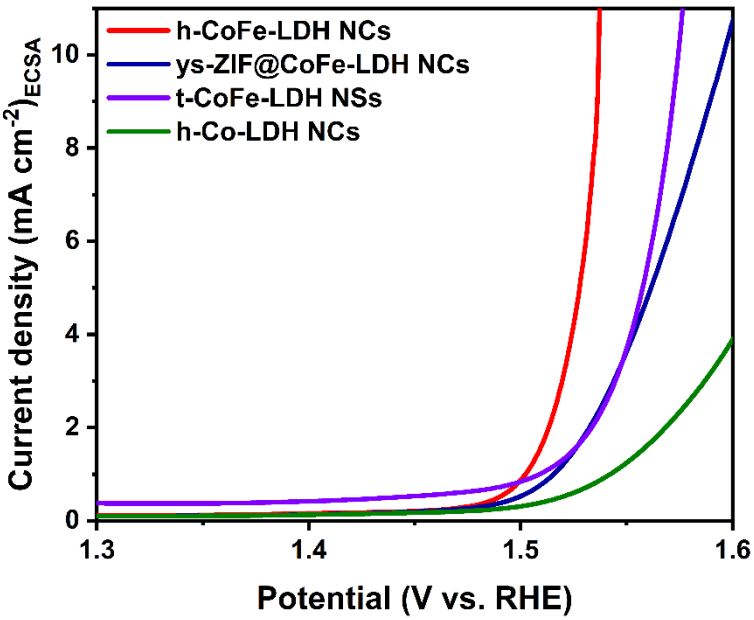

Figure 4.18. LSV curves normalized by electrochemically active surface areas (ECSAs).

This outstanding performance is likely due to the synergistic effect originating from the distinctive micromorphology, the intercalation of oxalate species, and the bimetallic interactions. The corresponding Tafel plots of the as-prepared electrocatalysts were also obtained to study the reaction kinetics. As shown in **Figure 4.15d**, h-CoFe-LDH NCs exhibited the smallest Tafel slope of 50 mV dec^{-1} compared with ys-ZIF@CoFe-LDH NCs (55 mV dec^{-1}), t-CoFe-LDH NSs (68 mV dec^{-1}), h-Co-LDH NCs (79mV dec^{-1}) and RuO_2 (83 mV dec^{-1}), demonstrating the enhanced OER kinetics. EIS plots of the samples were collected to gain insight into the charge transfer resistance during OER. As displayed in **Figure 4.15e**, h-CoFe-LDH NCs possessed the smallest charge-transfer resistance compared with ys-ZIF@CoFe-LDH NCs, t-CoFe-LDH NSs, h-Co-LDH NCs, and RuO_2, which would enhance the charge transfer kinetics, thereby promoting the OER activity.

h-CoFe-LDH NCs also display good stability during long-term electrolysis. The chronoamperometric curve shows that the potential experienced negligible change while maintaining 10 mA cm^{-2} for more than 16 h **(Figure 4.15f)**. Meanwhile, SEM **(Figure**

4.15f, inset) and TEM images **(Figure 4.19)** show that the morphology of h-CoFe-LDH NCs remains the same after the long-term durability test.

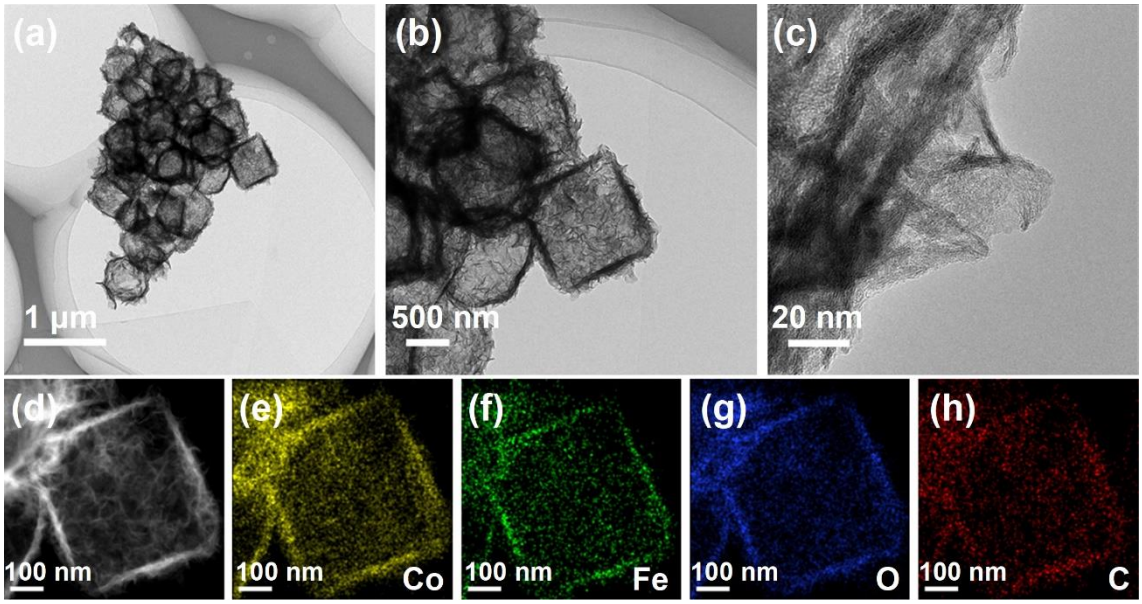

Figure 4.19. TEM images of h-CoFe-LDH NCs after the OER test.

However, totally different PXRD patterns (**Figure 4.20**) and Raman spectra (**Figure 4.21**) demonstrate a structural reconstruction of the catalyst during the OER process. XPS measurement of h-CoFe-LDH NCs after the stability test shows some changes (**Figure 4.22**), namely, the high-resolution XPS of O 1s suggesting the formation of oxyhydroxide (MOOH, 535 eV)[140]. Based on the Raman and XPS results, the CoFe-LDH phase transformed into metal oxyhydroxide, which has been widely accepted as the real active species for OER [127, 141].

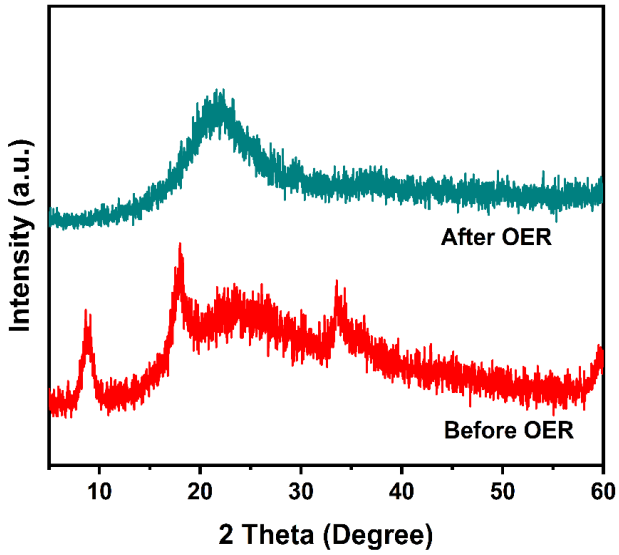

Figure 4.20. PXRD patterns of h-CoFe-LDH NCs before and after the long-term stability test.

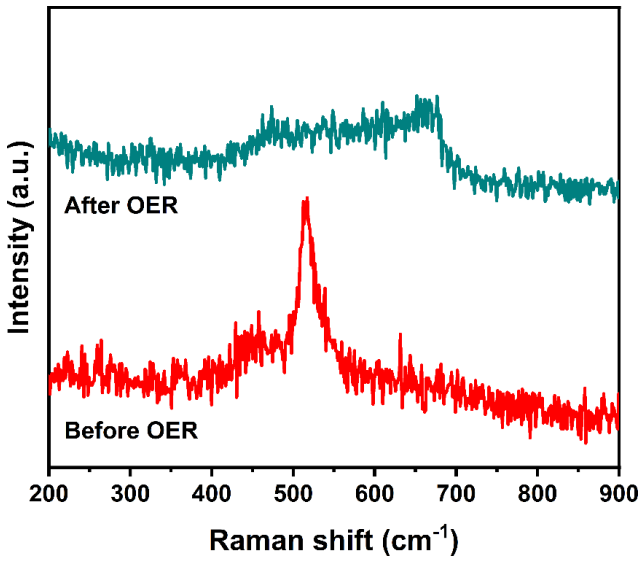

Figure 4.21. Raman spectra of h-CoFe-LDH NCs before and after the long-term stability test.

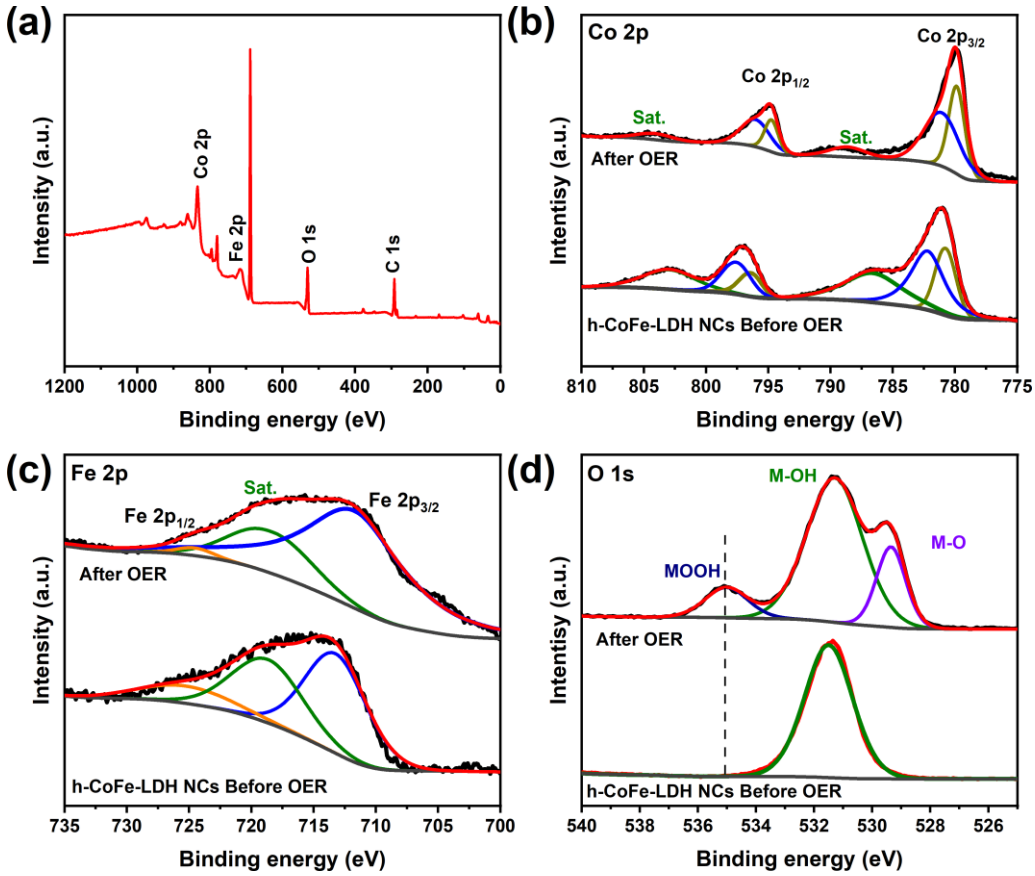

Figure 4.22. (a) XPS survey, (b) Co 2p, (c) Fe 2p, and (d) O 1s spectra of h-CoFe-LDH NCs before and after the OER test.

As mentioned above, replacing OER with thermodynamically favourable ethylene glycol (EG, a hydrolysate of polyethylene terephthalate (PET) plastic) oxidation reaction can simultaneously reduce energy input and upcycle PET plastic waste to produce value-added products. As a proof of concept, the electrocatalytic performance of the as-obtained catalysts toward EGOR was also investigated. As shown in **Figure 4.23a**, h-CoFe-LDH NCs exhibited a much higher activity than that h-Co-LDH NCs. This is consistent with the literature that Co species (*e.g.*, Co^{3+}) are the real active species for EGOR, whose activity can be further enhanced via moderate Fe doping [142]. On the other hand, unlike OER, ys-ZIF@CoFe-LDH NCs exhibited a better EGOR activity compared with h-CoFe-LDH NCs, which may be due to the synergistic cooperation between the ZIF-67 cores and the CoFe-LDH shells. The unique yolk-shell structure enables the enrichment of EG

within the voids during the electrocatalytic process and subsequently enhances the EGOR performance. Specifically, ys-ZIF@CoFe-LDH NCs needed only 1.39 V to reach 50 mA cm^{-2}, which is 20 and 150 mV lower than those for h-CoFe-LDH NCs and h-Co-LDH NCs, respectively. The voltage is 144 mV lower than that required to deliver the same current density for OER **(Figure 4.23a, inset)**, demonstrating the potential of replacing OER with EGOR to reduce energy input for water electrolysis.

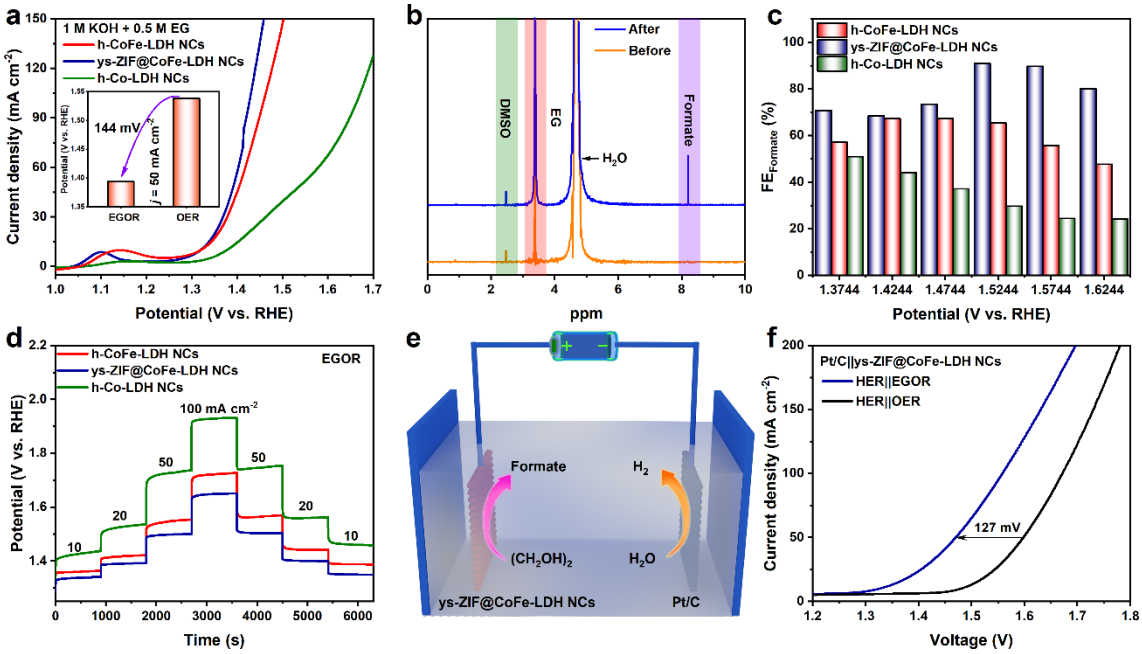

Figure 4.23. (a-d) EGOR performance of the catalysts: (a) LSV curves; (b) ^{1}H NMR spectra of the electrolyte before and after electrolysis; (c) correlation between potential and $FE_{formate}$; (d) multi-step chronopotentiometry curves from 10 to 100 mA cm^{-2}; (e) the schematic illustration and (f) LSV curves of the HER||OER and HER||EGOR based on the Pt/C||ys-ZIF@CoFe-LDH NCs pair.

The oxidation products during EGOR were quantitatively analyzed using ^{1}H nuclear magnetic resonance (NMR) spectroscopy. Notably, formate is the only detectable liquid product during constant potential electrolysis **(Figure 4.23b and Figure 4.24)**. ys-ZIF@CoFe-LDH NCs yielded the highest Faradaic efficiencies for formate generation

($FE_{formate}$) **(Figure 4.23c)**, when compared with h-CoFe-LDH NCs and h-Co-LDH NCs at all applied potentials. The maximum $FE_{formate}$ of ys-ZIF@CoFe-LDH NCs is 91%, while those of h-CoFe-LDH NCs and h-Co-LDH NCs are only 67% and 51%, respectively. ys-ZIF@CoFe-LDH NCs also provide the highest formate partial current density ($j_{formate}$) compared with the other two samples **(Figure 4.25)**, further indicating its excellent EGOR performance. Moreover, ys-ZIF@CoFe-LDH NCs showed excellent long-term stability toward EGOR with negligible potential changes during the multi-step and constant chronopotentiometry measurements **(Figure 4.23d and Figure 4.26)**. It is worth noting that the slight increase in potential should be caused by the continuous consumption of ethylene glycol during the electrolysis process.

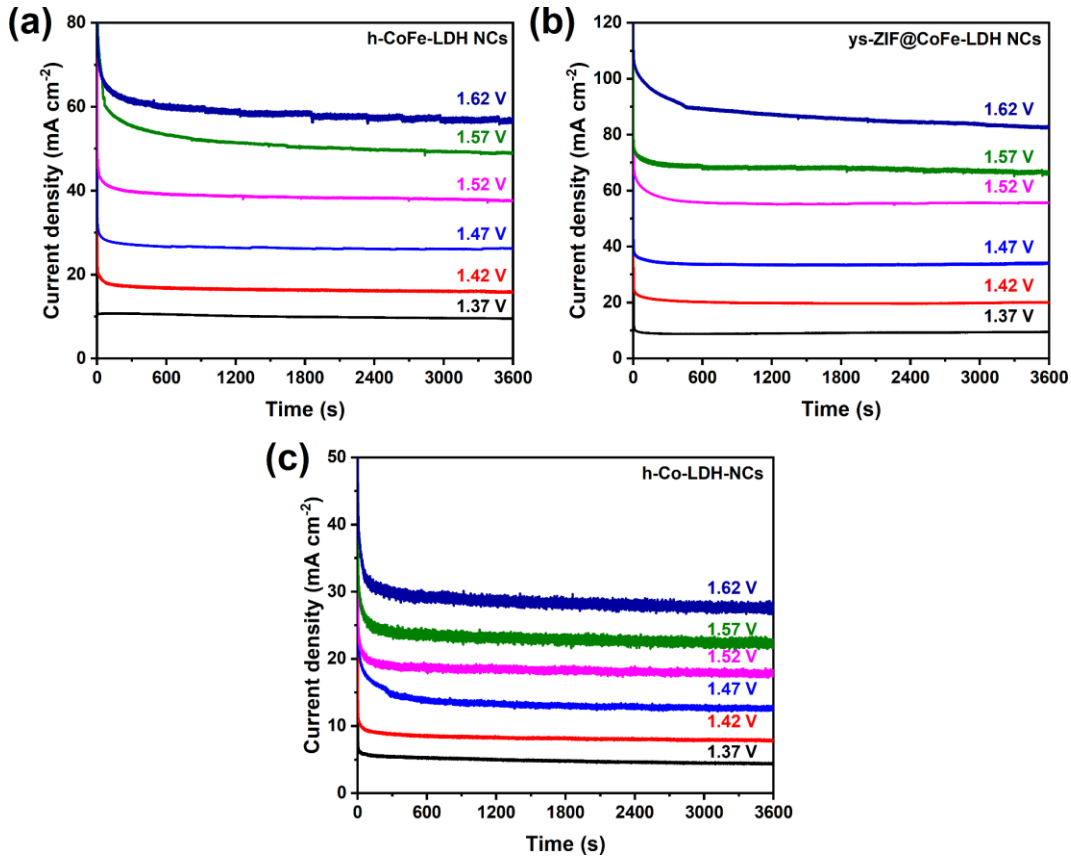

Figure 4.24. Correlation between current density and voltage as a function of time: (a) h-CoFe-LDH NCs, (b) ys-ZIF@CoFe-LDH NCs and (c) h-Co-LDH NCs in 1.0 M KOH with 0.5 M EG.

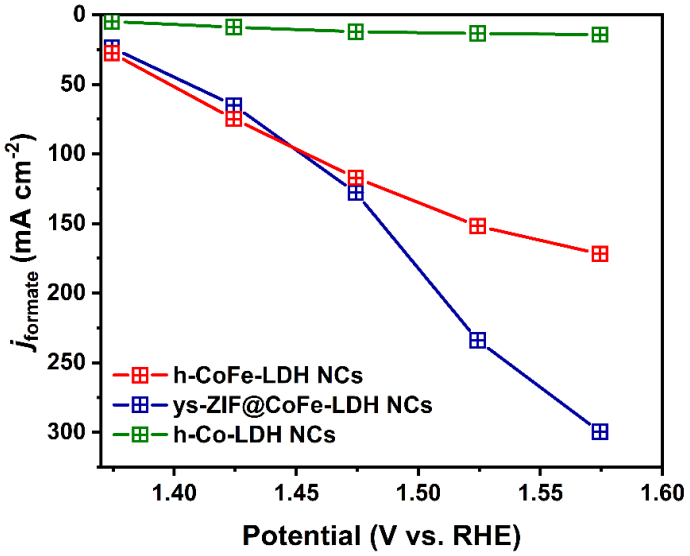

Figure 4.25. Potential-dependent $j_{formate}$ of h-CoFe-LDH NCs, ys-ZIF@CoFe-LDH NCs, and h-Co-LDH NCs.

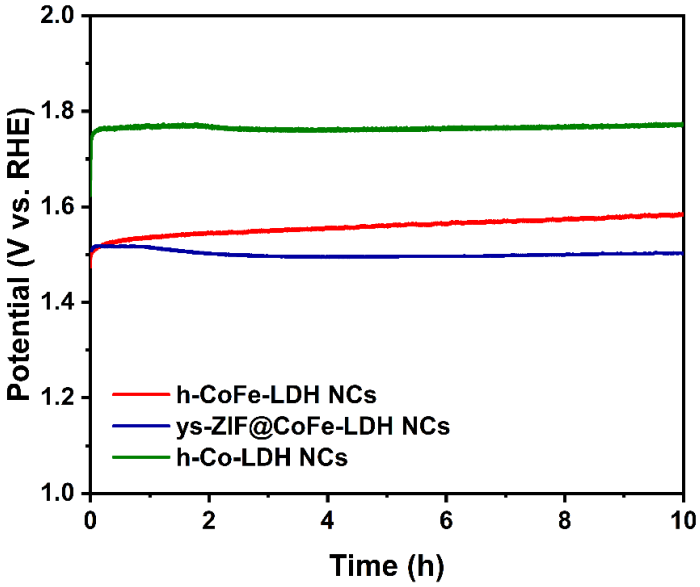

Figure 4.26. Long-term stability test for h-CoFe-LDH NCs, ys-ZIF@CoFe-LDH NCs, and h-Co-LDH NCs at 50 mA cm^{-2} in 1.0 M KOH with 0.5 M EG.

Encouraged by the excellent EGOR performance of ys-ZIF@CoFe-LDH NCs, an HER||EGOR hybrid system was assembled to generate H_2 and formate simultaneously, where commercial Pt/C and ys-ZIF@CoFe-LDH NCs are served as the cathode and the anode, respectively (**Figure 4.23e**). As shown in **Figure 4.23f**, a cell voltage of 1.47 V

was needed to deliver a current density of 50 mA cm^{-2} for concurrent HER and EGOR, which is 127 mV lower compared with HER||OER. Pt/C||ys-ZIF@CoFe-LDH NCs also exhibited better HER||EGOR performance than Pt/C||h-CoFe-LDH NCs, Pt/C||h-Co-LDH NCs, and even Pt/C||RuO_2 (**Figure 4.27 and Figure 4.28**). Notably, the HER||EGOR performance of Pt/C||ys-ZIF@CoFe-LDH NCs is better than most recently reported transition metal-based electrocatalysts (**Table 4.2**). The produced formate was quantitatively analyzed. As shown in **Figure 4.29**, despite the similar Faradaic efficiencies for H_2 generation (FE_{H2}), the values of $FE_{formate}$ over Pt/C||ys-ZIF@CoFe-LDH NCs are the highest among all the electrode pairs.

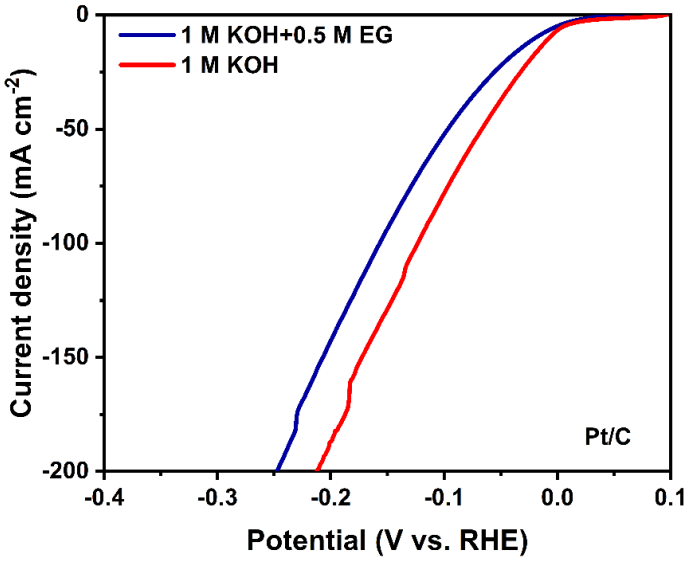

Figure 4.27. HER performance of commercial 20% Pt/C in 1.0 M KOH with and without 0.5 M EG.

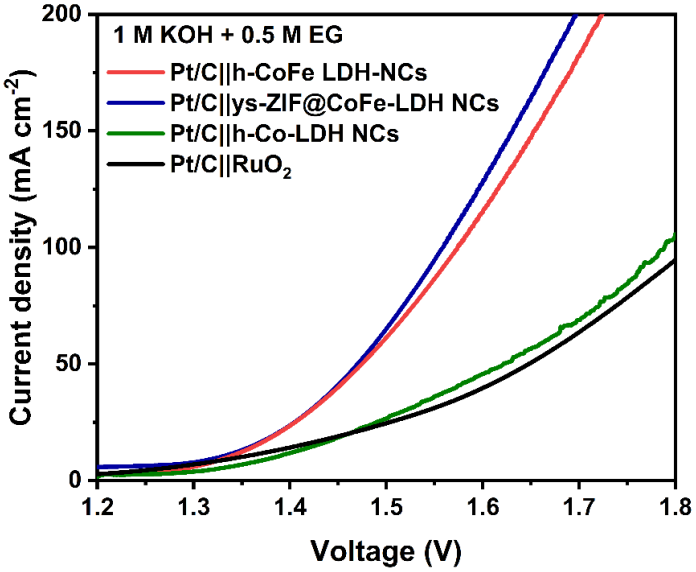

Figure 4.28. Polarization curves over the pairs of Pt/C||h-CoFe-LDH NCs, Pt/C||ys-ZIF@CoFe-LDH NCs, Pt/C||h-Co-LDH NCs and Pt/C||RuO_2 in 1.0 M KOH with 0.5 M EG.

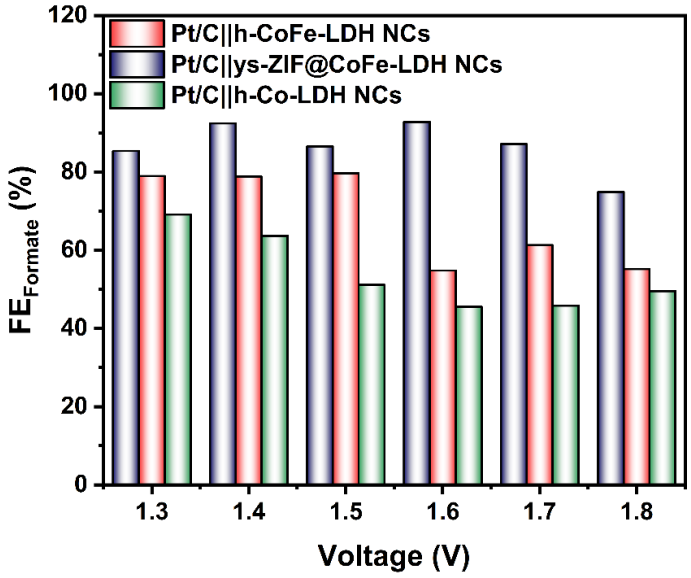

Figure 4.29. Voltage-dependent FEs of anodic EGOR over the Pt/C||h-CoFe-LDH NCs, Pt/C||ys-ZIF@CoFe-LDH NCs and Pt/C||h-Co-LDH NCs pair.

Table 4.2. Performance comparison of overall water splitting (HER||OER) and hybrid electrolysis coupled with small organic molecule oxidation reactions in recent reports and this work.

Electrocatalysts	Voltage at 10 mA cm^{-2} (V)	Refs.
Pt/C||ys-ZIF@CoFe-LDH NCs	**1.327 (HER||EGOR)** **1.48**	**This work**
Pt/C||h-CoFe-LDH NCs	**1.47**	**This work**
Co/CoP@HOMC	1.54	[139]
OMS-Ni_1-CoP	1.52 (HER||EGOR) 1.68	[58]
FeNi-P	1.63	[143]
Co_2P/CoNPC	1.64	[144]
Cu-CoP NAs/CP	1.72	[145]
$Co(OH)_2$@HOS/CP	1.497 (HER||MOR)[1]	[146]
$Ni_{0.33}Co_{0.67}(OH)_2$/NF	1.50 (HER||MOR)[1]	[147]
NF/NiMoO-Ar||NF/NiMoO-H_2	1.38 (HER||UOR)[2]	[148]

Note: [1]The anodic reaction is the oxidation of methanol (MOR). [2]The anodic reaction is the oxidation of urea (UOR).

4.4. Conclusion

In summary, a facile etching-reconstruction strategy was used to prepare hollow h-CoFe-LDH NCs and yolk-shell ys-ZIF@CoFe-LDH NCs by using ZIF-67 nanocrystals as the template. The oxalate anions are crucial for the formation of such distinctive morphology, which not only exposes abundant accessible active sites with enhanced intrinsic activity but also facilitates charge and mass transport, thereby promoting electrochemical performance. Specifically, h-CoFe-LDH NCs exhibited an outstanding OER performance with an overpotential of only 278 mV to achieve the current density of 50 mA cm^{-2}, superior to commercial RuO_2 catalyst and Co-based electrocatalysts reported. ys-ZIF@CoFe-LDH NCs can selectively electro-oxidize ethylene glycol to formate with a Faradaic efficiency as high as 91%. Assembly of ys-ZIF@CoFe-LDH NCs and commercial Pt/C catalyst into an HER||EGOR hybrid electrolysis system enables efficient simultaneous production of H_2 and formate with less energy input. This work sheds light on the development of efficient MOF-derived catalysts for desired electrochemical reactions.

CHAPTER 5 MoC-Fe Heterojunctions Encapsulated in N-doped Carbon Nanotubes for Water Splitting

This chapter has been extracted from the published paper of M. Huang, S. Zhou, D. Ma, W. Wei, Q. -L. Zhu, Z. Huang, "MOF-Derived MoC-Fe Heterojunctions Encapsulated in N-doped Carbon Nanotubes for Water Splitting", *Chemical Engineering Journal*, 2023, 145170.

5.1. Introduction

Water electrosplitting is an attention-grabbing technique as the most efficient and cleanest route for hydrogen production [1], however, it currently suffers from low energy-efficiency, sluggish kinetic, and poor durability, especially in alkali [149, 150]. To achieve economical applications, emphasis is now on the fabrication of highly active and stable electrocatalysts for HER and OER [151]. Normally, conventional Pt-based materials and Ir/Ru oxides (IrO_2 and RuO_2), are best electrocatalysts for HER and OER, respectively [152-154]. However, a substantial commercialization of noble metal-based electrocatalysts is hindered due to their high cost, scarcity, inferior stability, and poor resistance to poisons (methanol or CO) [155]. Thus, great efforts have been focused on developing highly efficient bifunctional TM-based electrocatalysts for simultaneous HER and OER.

TM and their carbides, nitrides [156], sulfides [157], selenides [32], and phosphides [158], exhibit promising catalytic performance and have been widely explored as potential substitutes. Among them, transition metal carbides, such as molybdenum carbides (MoC_x), are promising electrocatalysts for HER because of their Pt-like electronic structure [159, 160]. Attempts have been made to tune their electrochemical properties by nanostructuring and hybridization with carbon materials [161-163]. Although MoC_x have been widely reported as one of the most effective electrocatalysts for HER, their poor OER activity has become a major hindrance to overall water splitting. Strong efforts are devoted to improving the OER performance of MoC_x, but the experimental results are still far from satisfactory. For instance, Luo et al.[164] reported a Mo_2C/carbon microsphere that requires a high overpotential of over 500 mV to reach a current density of 10 mA cm^{-2}. Hence, the design of highly active MoC_x-based HER and OER electrocatalysts for alkaline electrolyzers is highly desirable but remains challenging.

Interfacial engineering is an effective strategy to promote the catalytic kinetics of MoC_x-based electrocatalysts because electrocatalytic reactions usually occur at the interfaces [55, 165-167]. It is demonstrated that heterojunctions can promote electron transfer, enrich the active sites, and thus promote catalytic ability [168, 169]. Thus, it is believed that a bifunctional HER/OER electrocatalyst can be fabricated through the construction of heterostructured catalysts. TMs, especially iron, have been reported as the most attractive metal in OER due to their low cost and inexhaustible supply [170, 171]. Previous studies have indicated that single Fe atom-based materials have poor HER activity and stability, but they work as an OER promotor in many multi-metallic electrocatalysts [172, 173]. Accordingly, the combination of Fe with MoC_x may offer great potential for boosting both the HER and OER activity. Heterojunctions composed

of early and post-transition metals feature abundant active sites at the interfaces owing to the synergistic effect of the two metals [174, 175]. Additionally, micro-nanostructural engineering is also effective in developing robust MoC_x-based hybrid electrocatalysts. Aggregation and corrosion of bare MoC_x/Fe nanoparticles easily occur in long-term tests, resulting in the degradation of catalytic activity [176]. Compared with bulk materials, encapsulating MoC_x and Fe into nitrogen-doped porous carbon materials can not only provide more stable active sites but also improve mass transfer, leading to higher electrocatalytic stability and activity [56, 177]. Among reported strategies, direct pyrolysis of MOFs is one of the most efficient approaches for manufacturing carbon-confined nanocrystalline porous structure with high surface areas [178]. Zn, Mo-based hybrid zeolitic imidazolate frameworks (denoted as Zn/Mo-HZIF) with MoO_4 units are among the ideal reactive precursors to obtain various nanostructured Mo-based electrocatalysts and corresponding hybrid derivatives [179, 180]. However, up to now, the development of novel MOF-derived Fe/MoC_x hybrid nanocomposite as an efficient bifunctional catalyst has rarely been reported.

Based upon the above findings, a novel hybrid nanostructure composed of MoC and Fe nanoparticles encapsulated in NCNTs was obtained from Fe-doped Zn/Mo-based MOF. The electrochemical results prove that it could be used as a bifunctional catalyst for water splitting. The as-prepared catalysts retain the well-defined morphology of the initial cubic framework, with surface shells of interconnected NCNTs. The hybrid nanostructure between Fe-MoC NPs and NCNTs has never been reported before. Benefitting from the advantageous features in composition, structure, and optimum graphitic degree, the resultant MoC-Fe@NCNTs show remarkable electrocatalytic activity and stability for both HER and OER.

5.2. Experimental section

5.2.1. Catalyst synthesis

Synthesis of ZIF-8. A solution of 300 mg zinc acetate dihydrate ($Zn(OAc)_2 \cdot 2H_2O$) in 5 mL of deionized water was added into a solution of 1120 mg 2-methylimidazolate in 5 mL of deionized water, and the mixture solution was continuously stirred for 60 seconds. The solution was then kept for 24 h at room temperature. The white precipitate was collected by centrifugation, washed in ethanol several times, and dried at 80 °C under vacuum.

Synthesis of Zn/Mo-HZIF. 100 mg ZIF-8 was dispersed in 15 mL DMF, and 50 mg $MoO_2(acac)_2$ was subsequently added into the solution and sonicated for 10 min. Finally, the solution was transferred to a Teflon-lined stainless-steel autoclave and kept at 150 °C for 6 h. After cooling to room temperature, the obtained HZIF were separated by centrifugation, washed methanol, and dried at 80 °C under vacuum.

Synthesis of Fe-doped Zn/Mo-HZIF. 300 mg as-prepared Zn/Mo-HZIF was dispersed in 20 mL methanol, and 30 mg of potassium ferrioxalate ($K_3Fe(C_2O_4)_3$) in 20 mL H_2O was then added and aged for 30 min. After that, the Fe-Zn/Mo-HZIF was collected by centrifugation, washed with methanol, and dried overnight at 60 °C under vacuum. Zn/Mo-HZIF doped with different amounts of Fe (10, 60, and 100 mg) was also prepared. For comparison, Fe-ZIF-8 was also synthesized using a method similar to that of Fe-Zn/Mo-HZIF, except that ZIF-8 instead of Zn/Mo-HZIF was used as the precursor.

Synthesis of MoC-Fe@NCNTs. In a typical synthesis, Fe-Zn/Mo-HZIF was transferred to a quartz tube and pyrolyzed at 700 °C for 2 h under Ar flow. For comparison, MoC nanocubes (NCs) were also synthesized by a similar method in the absence of Fe. Fe-NCs were also synthesized by pyrolyzing Fe-ZIF-8 with the same procedure.

5.3. Results and discussion

The synthetic process of MoC-Fe@NCNTs composite is schematically illustrated in **Figure 5.1**.

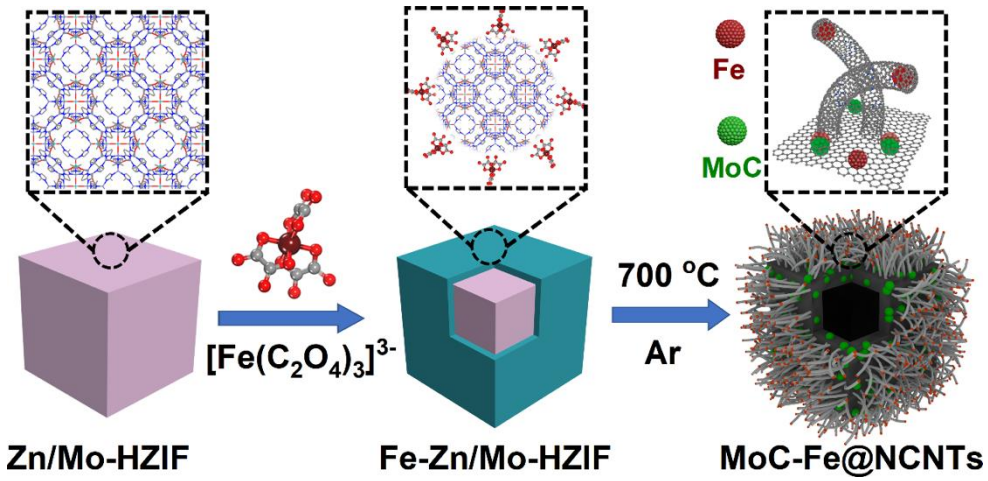

Figure 5.1. Schematic illustration of the fabrication of MoC-Fe@NCNTs.

In brief, ZIF-8 dodecahedrons are first obtained according to the modified method reported [181]. The PXRD pattern confirms the crystal structure and FESEM image shows solid ZIF-8 cubes with an average diameter of 300 nm (**Figure 5.2**).

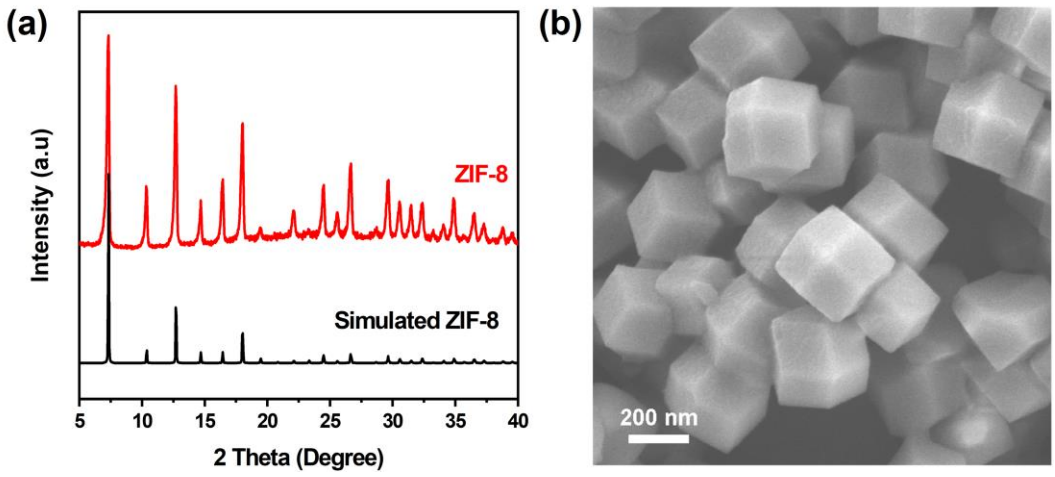

Figure 5.2. PXRD pattern and a FESEM image of the as-synthesized ZIF-8 crystals.

Zn/Mo-HZIF nanocubes (NCs) were then prepared through an anion exchange reaction starting from ZIF-8. Through a solvothermal transformation process at 150 °C, ZIF-8 nanoparticles reacted with MoO_4^{2-} leading to Zn/Mo-HZIF. As shown in **Figure**

5.3, Zn/Mo-HZIF consists of two kinds of tetrahedral building blocks and structural features of both zeolites and ZIFs.

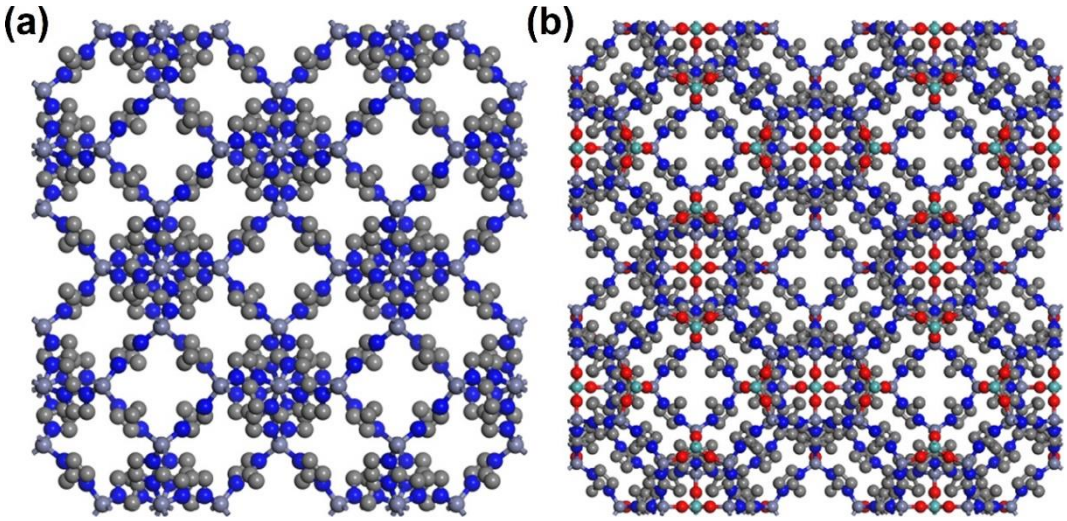

Figure 5.3. Structure comparison between (a) ZIF-8 and (b) Zn/Mo-HZIF. $Zn(im)_4$ was partially substituted by MoO_4 in HZIF.

The PXRD pattern of the as-achieved Zn/Mo-HZIF is entirely different from that of ZIF-8, indicating the successful MOF-to-MOF transformation (**Figure 5.4a**). Besides, the Zn/Mo-HZIF adopts a cubical structure with much larger NCs (2 μm, **Figure 5.4b**), very different from that of the starting ZIF-8 NPs.

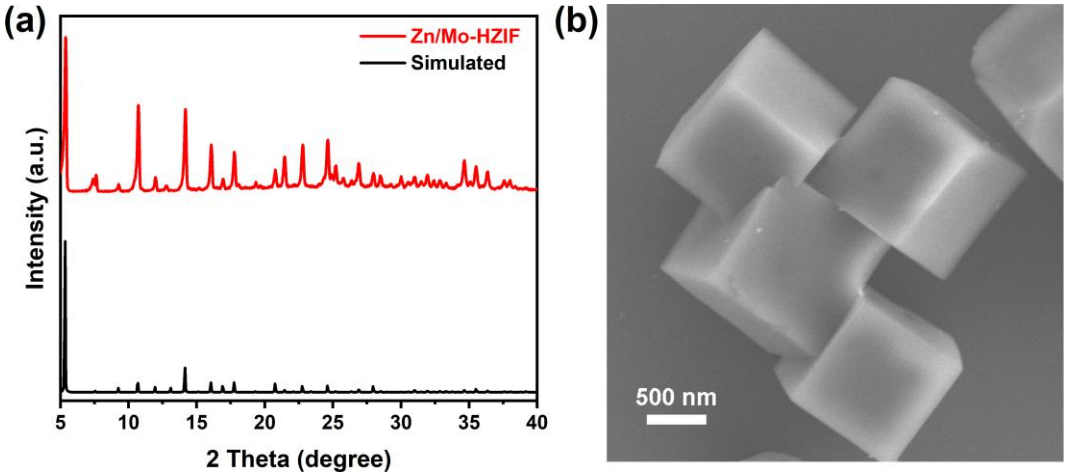

Figure 5.4. PXRD pattern and a FESEM image of the as-synthesized Zn/Mo-HZIF nanocubes.

Subsequently, Zn/Mo-HZIF was homogeneously dispersed in methanol, followed by the addition of $K_3[Fe(C_2O_4)_3]$ aqueous solution. Through a double-solvent approach, $[Fe(C_2O_4)_3]^{3-}$ units were encapsulated into cavities of Zn/Mo-HZIF framework to form Fe-Zn/Mo-HZIF nanocomposites. PXRD pattern reveals a crystal structure similar to that of Zn/Mo-HZIF. FESEM image (**Figure 5.5**) confirms that the obtained Fe-Zn/Mo-HZIF maintains the cubical shape, but the surfaces of nanocubes become porous after the chemical etching process.

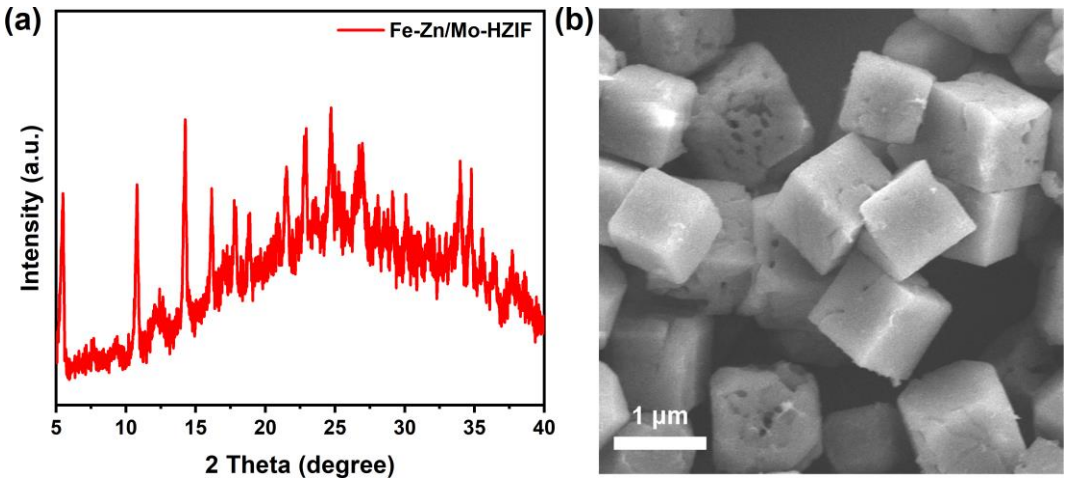

Figure 5.5. PXRD pattern and a FESEM image of the as-obtained Fe-Zn/Mo-HZIF nanocubes.

Fe-Zn/Mo-HZIF frameworks appear green which is different from the light blue color of pristine Zn/Mo-HZIF (**Figure 5.6**).

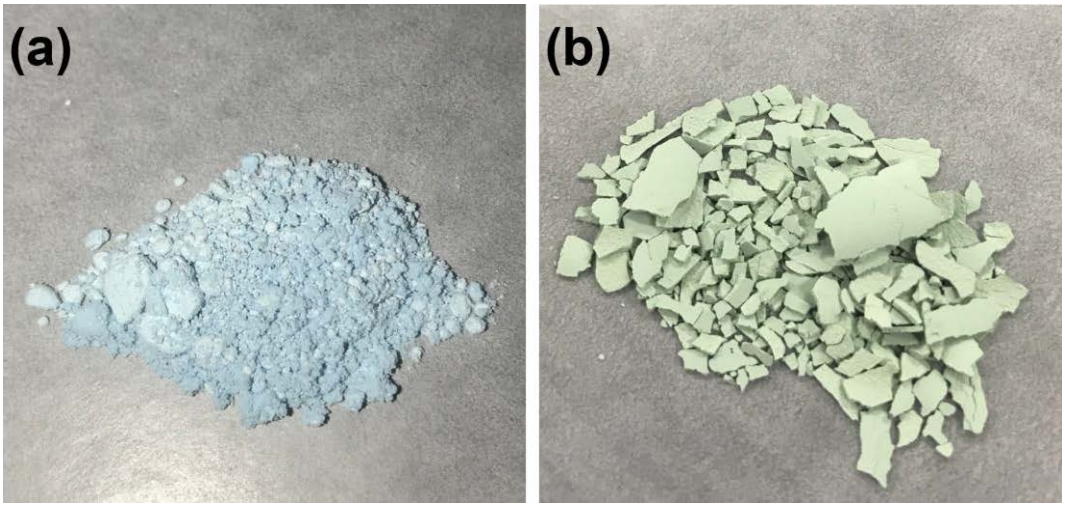

Figure 5.6. Digital photos of the (a) Zn/Mo-HZIF and (b) Fe-Zn/Mo-HZIF.

EDS analysis proves the existence of Fe, suggesting the successful trapping of Fe in the framework of Zn/Mo-HZIF (**Figure 5.7**).

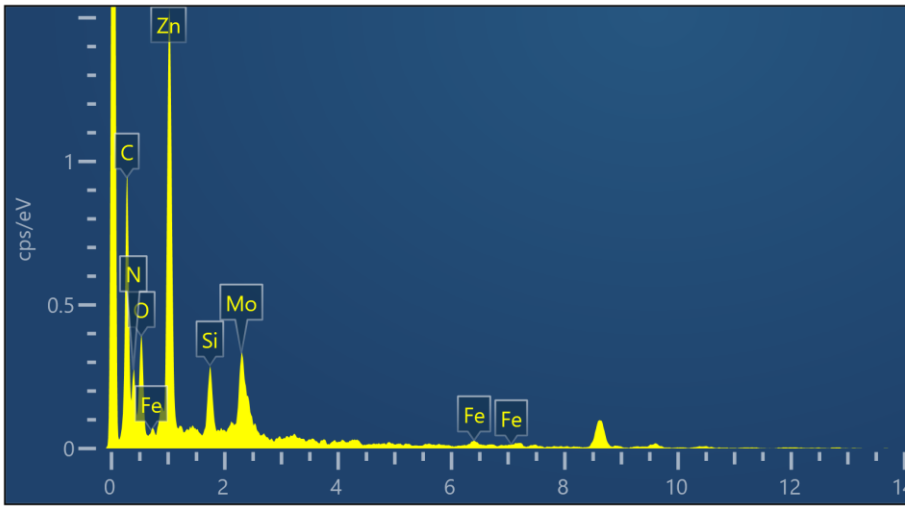

Figure 5.7. EDS spectrum of the as-prepared Fe-Zn/Mo-HZIF.

MoC-Fe@NCNTs were obtained via the pyrolysis of Fe-Zn/Mo-HZIF at 700 °C in an argon atmosphere. FESEM **(Figure 5.8a-c)** and TEM images **(Figure 5.8d-f)** indicate that MoC-Fe@NCNTs inherit the original morphology but with many nanocrystals confined in porous carbon nanocubes, and the surfaces of the particles become much rougher. An interesting feature is that numerous short CNTs wrapping NPs, especially at the tip of the CNTs, can be observed on the rough surfaces **(Figure 5.8 c,e)**. The HRTEM

image (**Figure 5.8f**) reveals fringe spacing of 0.214 nm and 0.201 nm which can be assigned to the (200) planes of MoC and (110) planes of Fe nanoparticles, respectively, whereas the distance of 0.341 nm is associated with the graphite carbon shells. HAADF-STEM image and EDS mapping **(Figure 5.8g)** show that C, N, and Mo are distributed evenly over the entire nanocubes, while Fe is mainly located at the outer shell, which suggest the successful synthesis of the core-shell structure of MoC-Fe@NCNTs. As a control experiment, Fe-NC and MoC NCs were prepared by a similar method using Fe-ZIF-8 and Zn/Mo-HZIF precursors, respectively.

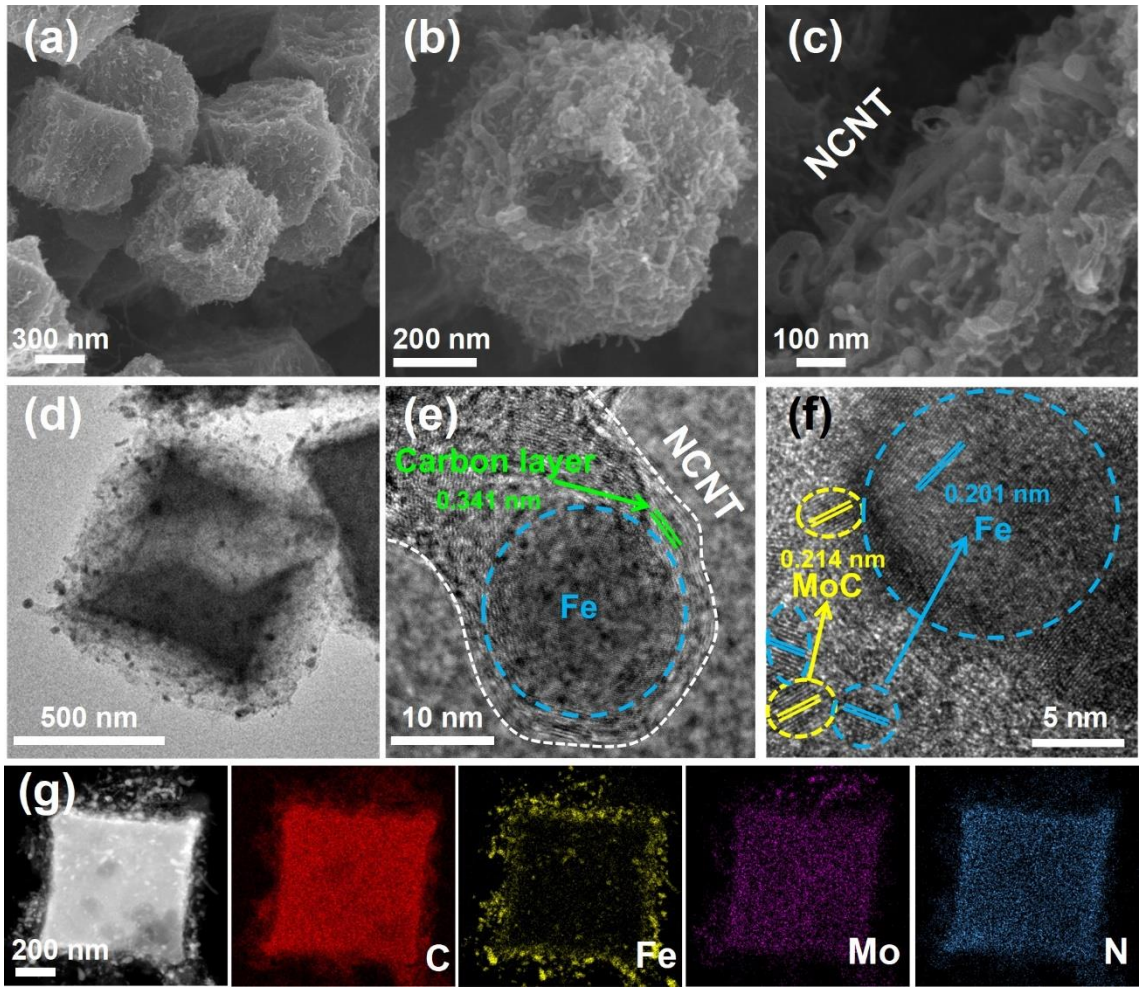

Figure 5.8. (a-c) FESEM and (d-f) TEM images of the obtained MoC-Fe@NCNTs; (g) HAADF-STEM image and the EDS mapping of MoC-Fe@NCNTs.

The formation of NCNTs is known due to the catalytic effect of TM NPs [182]. However, it was found that the same pyrolysis treatment on Fe-ZIF-8 and Zn/Mo-HZIF control samples could not produce NCNTs (**Figure 5.9 and Figure 5.10**). This indicates that the co-existence of Fe and Mo species plays a critical role in the growth of NCNTs.

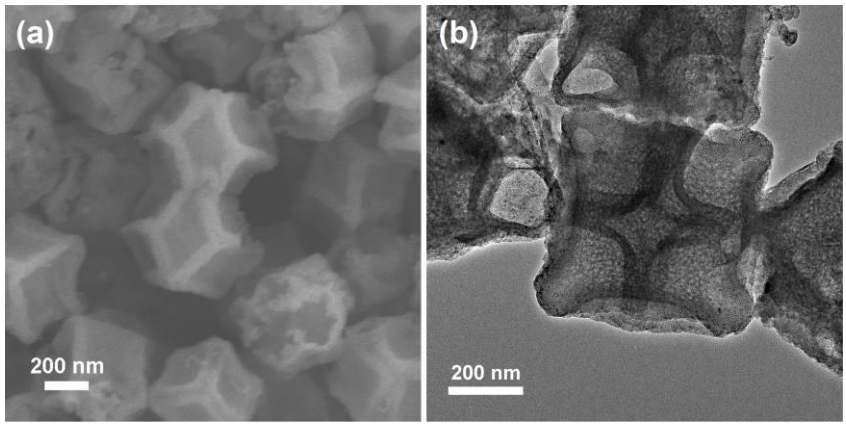

Figure 5.9. (a) FESEM and (b) TEM images of Fe-NC dodecahedrons.

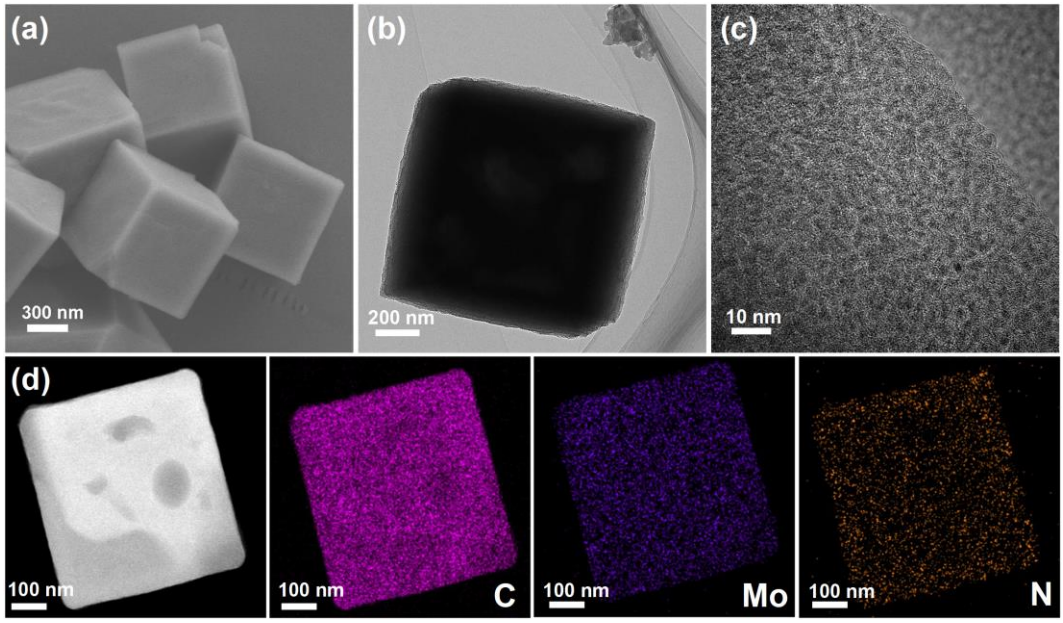

Figure 5.10. (a) FESEM and (b-d) TEM images of MoC NCs.

To gain further insight into the formation of hierarchical structures, the morphological evolution was monitored when annealing the Fe-HZIF but with different Fe contents. Indeed, the introduction of Fe contributes to the formation of NCNTs

(**Figure 5.11a**), and the amount of Fe dopant has a significant effect on the morphology of the products. As shown in **Figure 5.11b**, low Fe dopant does not contribute to the formation of NCNTs during the heat treatment. An excessive amount of Fe, however, will over-etch HZIF and eventually lead to the collapse of the nanocubes (**Figure 5.11d**).

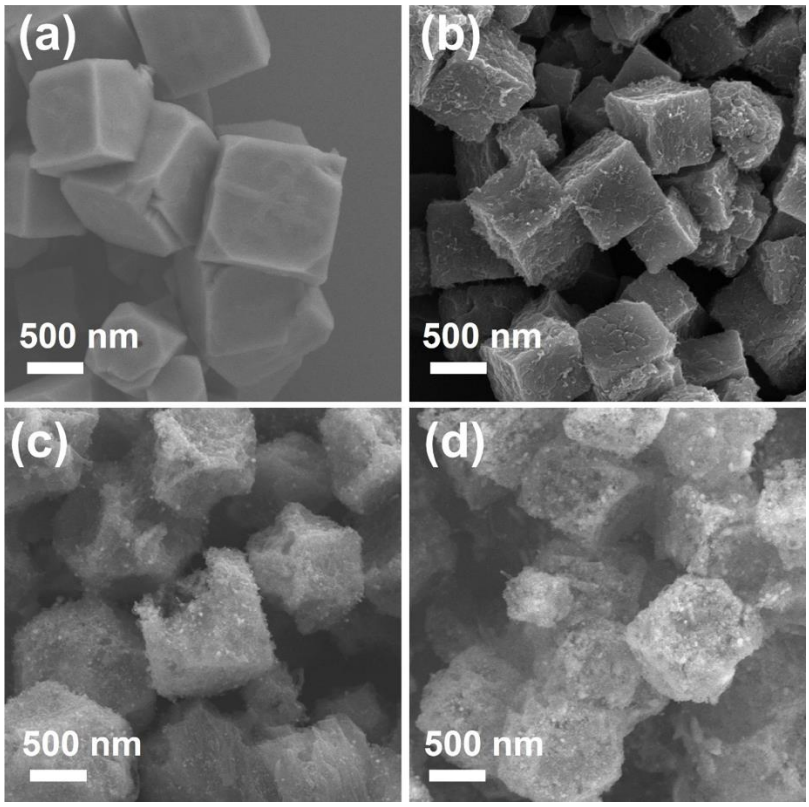

Figure 5.11. FESEM images of the products obtained by pyrolyzing Fe-HZIF particles with different Fe contents at 700 ℃: (a) 0 mg, (b) 10 mg, (b) 60 mg, and (c) 100 mg.

Additionally, a suitable temperature is also indispensable for the formation of hierarchical frameworks. At a lower temperature of 500 ℃, only solid cube-shaped particles with smooth surfaces could be obtained due to the incomplete pyrolysis of HZIFs and insufficient growth of NCNTs (**Figure 5.12a**). For treatment at 900 ℃, more complete pyrolysis led to longer NCNTs, and the particles started to agglomerate at the same time. Based on the above results, it can be speculated that Fe^{3+} is first reduced to metallic Fe during the heat treatment, followed by the catalytic growth of NCNTs.

Meanwhile, the MoO_4^{2-} units react with carbonaceous species derived from 2-methylimidazolate ligands to form MoC_x nanocrystallites. In this process, Zn/Mo-HZIF serves not only as the C and N sources for the growth of NCNTs but also as the template for the resultant product. The carbonization and the growth of NCNTs take place simultaneously, leading to the formation of the porous interconnected heterostructure. Such a porous structure typically enhances the access to the active sites and enables good contact between inner MoC particles and electrolytes, thereby promoting catalytic activity.

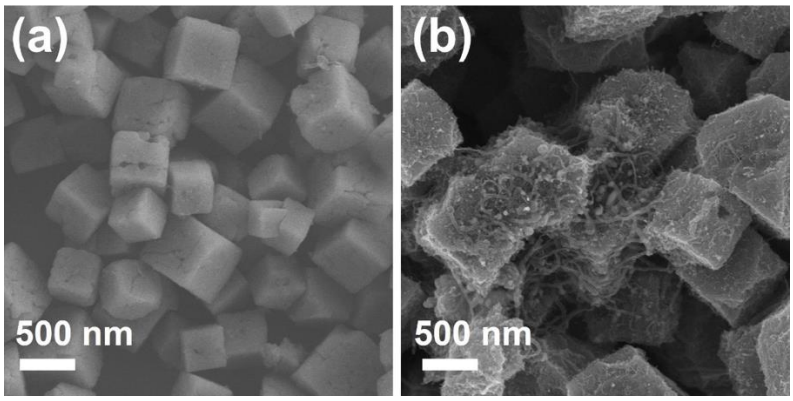

Figure 5.12. FESEM images of products obtained by heating Fe_{30}-HZIF particles at (a) 500 °C and (b) 900 °C.

The composites were further analyzed by PXRD **(Figure 5.13a**). In addition to the carbon matrix (≈ 25°), the PXRD pattern of MoCx shows two peaks around 36.4° and 43.3°, corresponding to the planes of MoC (JCPDS, no. 65-0280). As for MoC-Fe@NCNTs, the diffraction pattern confirms the presence of MoC and Fe (JCPDS, no. 01-1262) phases. More structural information about the resultant heterostructures can be gain from the Raman spectra. As shown in **Figure 5.13b,** the bands at the low range (900-1000 cm^{-1}) can be assigned to MoC species. The bands at 1343 and 1583 cm^{-1} are attributed to the D band and G band of the graphite carbon, which is related to

disordered/defective carbon and the graphitic sp^2-carbon, respectively. In addition, the higher intensity ratio (I_G/I_D) indicates the enhanced graphitization degree in the MoC-Fe@NCNTs, which may contributed to a better electrical conductivity while stabilizing the Fe and MoC NPs [183]. The N_2 adsorption isotherms reveal that both samples have typical micro-/mesoporous features, as evidenced by the characteristics of type-IV isotherms **(Figure 5.13c)**. After adding Fe, the BET surface area decreased from 326 (MoC NCs) to 265 $m^2\ g^{-1}$ (MoC-Fe@NCNTs) as a result of consumption of carbon materials. Unlike MoC NCs, MoC-Fe@NCNTs has a broader mesopore distribution range from 2 nm to 10 nm **(Figure 5.13c, inset)**. The difference in pore size between MoC-Fe@NCNTs and MoC NCs may be ascribed to the unique mesopore-forming role of Fe in the HZIF precursors.

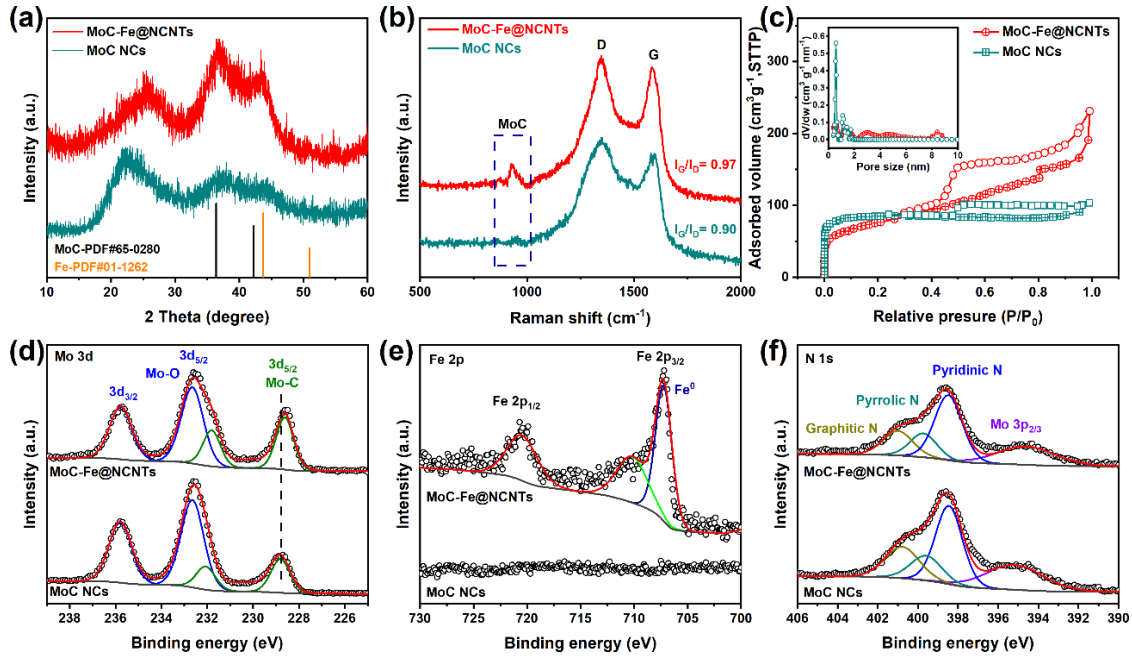

Figure 5.13. (a) PXRD patterns; (b) Raman spectra; (c) N_2 sorption isotherms; (d–f) High-resolution Mo 3d, Fe 2p, and N 1s XPS spectra of MoC-Fe@NCNTs and MoC NCs.

XPS was performed to further analyze the surface composition and chemical states. The XPS survey spectrum of MoC-Fe@NCNTs show the presence of Fe, Mo, C, N, and O, whereas no Fe was detected in MoC NCs **(Figure 5.14)**. The Mo 3d XPS spectra

(**Figure 5.13d**) contain two pairs of peaks in both MoC-Fe@NCNTs and MoC NCs, which can be attributed to Mo-C bonds (228.6 eV, 231.8 eV) and Mo-O bonds (232.6 eV, 235.7 eV), respectively [184]. In comparison with MoC NCs, the peaks of Mo-C in MoC-Fe@NCNTs shift to lower energy, which may be caused by the interactions between MoC and Fe. The Fe 2p spectra can be clearly deconvoluted into two pairs of $2p_{3/2}$-$2p_{1/2}$ doublets **(Figure 5.13e)**, corresponding to the metallic Fe and the high valence N-coordinated Fe component (Fe-N_x) [185]. The presence of nitrogen atoms with different chemical states in both MoC-Fe@NCNTs and MoC NCs can be found by deconvoluting N 1s signals into three subpeaks, corresponding to pyridinic N, pyrrolic N and graphitic N **(Figure 5.13f)**, indicating the formation N-doped C.

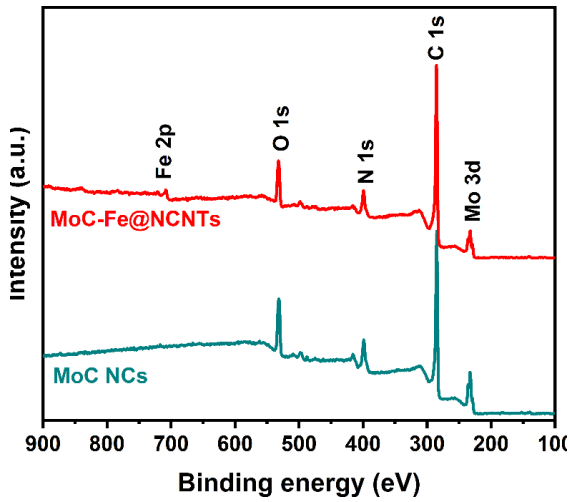

Figure 5.14. XPS survey spectra of MoC-Fe@NCNTs and MoC NCs.

The electrocatalytic HER and OER activity of MoC-Fe@NCNTs was evaluated in 1.0 M KOH. **Figure 5.15a** shows the HER polarization curves of different electrodes. As expected, the MoC-Fe@NCNTs catalyst delivers remarkable HER activity. To reach a high current density of 50 mA cm^{-2}, the required overpotential for MoC-Fe@NCNTs is only 252 mV. In contrast, 83 and 134 mV higher overpotentials are needed for MoC NCs and Fe-NC, respectively, to afford the same current density. In addition, the current

density of MoC-Fe@NCNTs rises much faster than that of MoC NCs and Fe-NC. Specifically, at an overpotential of 300 mV, the current density of MoC-Fe@NCNTs reached 182 mA cm^{-2}, which is 5.7-fold and 10.1-fold those of MoC NCs (32 mA cm^{-2}) and Fe-NC (18 mA cm^{-2}), respectively (**Figure 5.15b**). **Figure 5.15c** displays the Tafel plots of the corresponding polarization curves. It can be seen that the Tafel slope of the MoC-Fe@NCNTs electrode is 144 mV dec^{-1}, smaller than that of MoC NCs (150 mV dec^{-1}) and Fe-NC (182 mV dec^{-1}), demonstrating rapid reaction kinetics of MoC-Fe@NCNTs. Additionally, the Fe content in MoC-Fe@NCNTs and the pyrolysis temperature also show a noticeable influence on the catalytic performance.

OER is another key half-reaction for water-splitting. **Figure 5.15d** displays OER polarization curves of MoC-Fe@NCNTs, MoC NCs, Fe-NC, commercial RuO_2, and Ni form substrate. Bare Ni foam shows negligible OER activity. MoC-Fe@NCNTs shows better catalytic activity with respect to MoC NCs and Fe-NC. More specifically, to reach j of 50 mA cm^{-2}, the required overpotentials (η) are 304, 407, and 328 mV for MoC-Fe@NCNTs, MoC NCs, Fe-NC, respectively, and at η = 300 mV, the recorded j are 42.3, 3.2, and 15.0 mA cm^{-2}, respectively **(Figure 5.15e)**. Such a result is even superior to the benchmarking RuO_2 catalyst. Furthermore, MoC-Fe@NCNTs has a Tafel slope of 57 mV dec^{-1}, which is much smaller than those of MoC NCs (103 mV dec^{-1}) and Fe-NC (62 mV dec^{-1}), thus indicating the greatly accelerated reaction kinetics due to Fe doping.

The electrochemical double layer capacitance (C_{dl}) value of MoC-Fe@NCNTs and MoC NCs was calculated to be 1.35 and 1.0 mF cm^{-2}, respectively **(Figure 5.15g and Figure 5.17)**. When the geometric current density at η = 300 mV was further normalized to the corresponding C_{dl} value, the OER catalytic activity of MoC-Fe@NCNTs was 9.4-fold higher than that of MoC NCs (**Figure 5.18b**). The much smaller diameter of the semicircle in the Nyquist plot of MoC-Fe@NCNTs suggests its low reaction resistance

and fast electron-transfer rate **(Figure 5.15h)**. Besides the catalytic activity, durability is an important criterion for an efficient electrocatalyst. In the long-term stability tests at 10 mA cm^{-2} for HER and OER, MoC-Fe@NCNTs displays a negligible potential change over 24 h, indicating outstanding stability **(Figure 5.15i)**. Moreover, compared with the bifunctional Mo-based electrocatalysts reported in the past three years, the catalytic activity of the as-designed MoC-Fe@NCNTs is better **(Table 5.1)**.

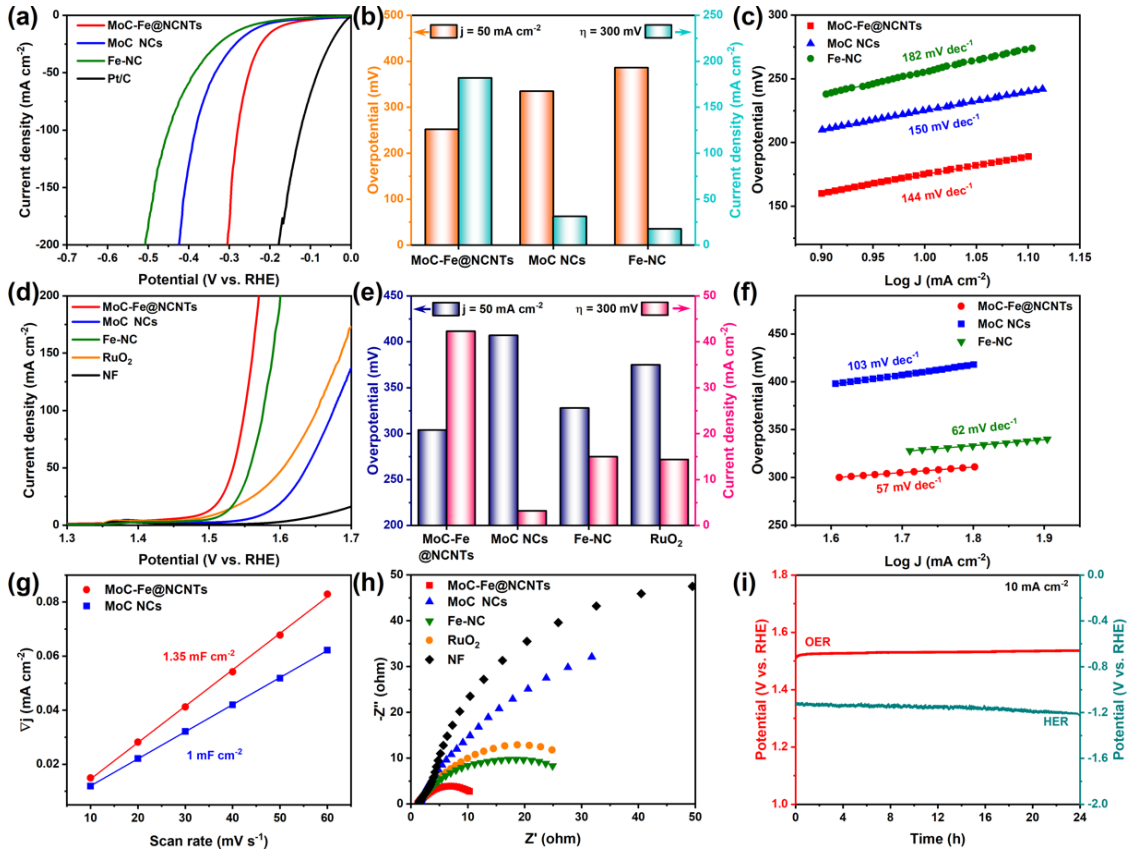

Figure 5.15. Bifunctional electrocatalytic evaluation toward HER and OER. (a) LSV curves for HER; (b) Comparison of η_{50} and current density under the 300 mV overpotential for HER; (c) Tafel plots for HER; (d) LSV curves for OER; (e) Comparison of η_{50} and current density under the 300 mV overpotential for OER; (f) Tafel plots for OER; (g) C_{dl} plots inferred from CV curves; (h) Nyquist plots; (i) Durability evaluation of MoC-Fe@NCNTs via CA test at j=10 mA cm^{-2} for both HER and OER.

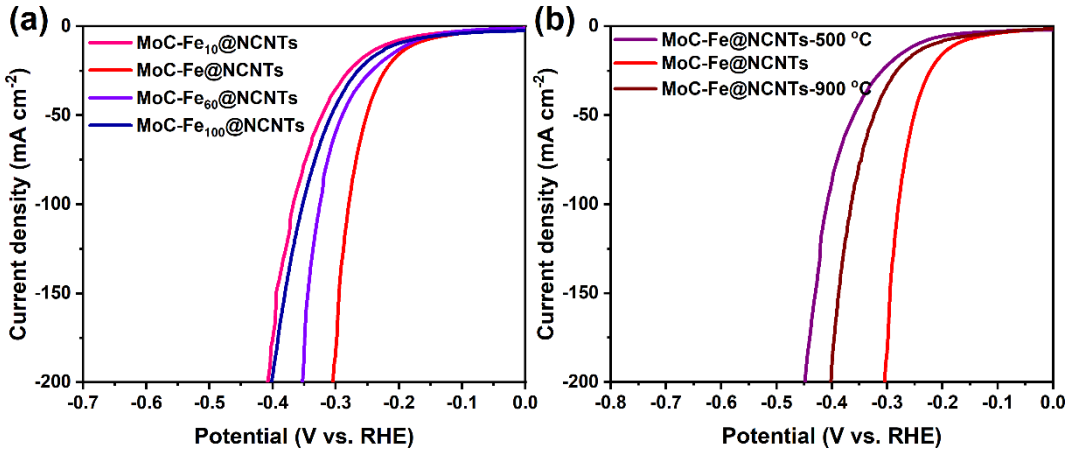

Figure 5.16. Polarization curves of MoC-Fe$_x$@NCNTs with (a) different Fe content and (b) different temperature.

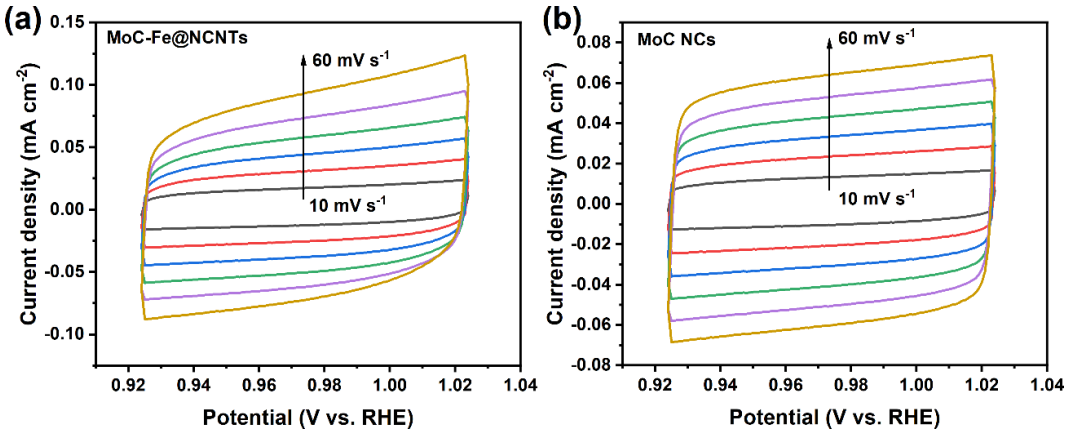

Figure 5.17. Cyclic voltammetry curves in a non-faradaic potential region under different scan rates for (a) MoC-Fe@NCNTs and (b) MoC NCs.

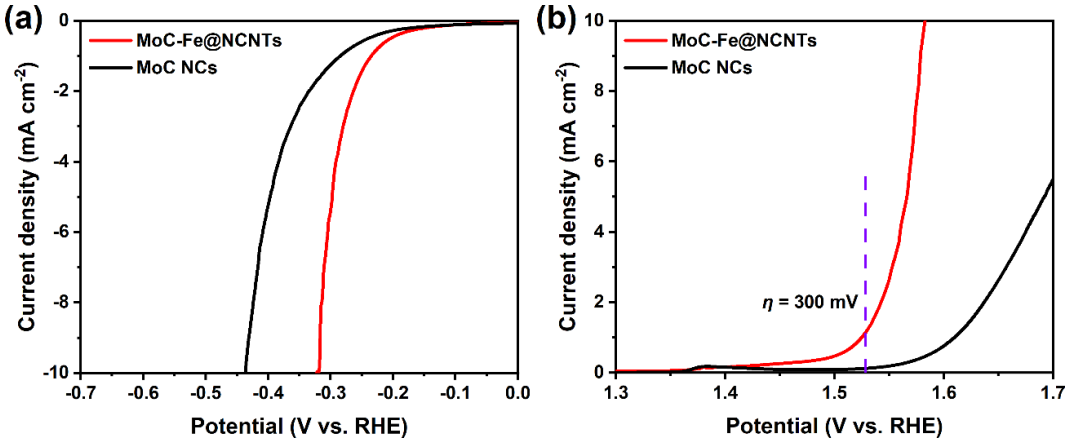

Figure 5.18. (a) HER and (b) OER LSV curves normalized by corresponding ECSA.

Table 5.1. Comparison of OER and HER activities in 1.0 M KOH between MoC-Fe@NCNTs and reported MoC_x-based electrocatalysts.

Electrocatalyst	η_{10}@OER (mV)	η_{10}@HER (mV)	References
MoC-Fe@NCNTs	**235** **304 (η_{50})**	**176** **252 (η_{50})**	**This work**
Co/β-Mo_2C@N-CNTs	356	170	[186]
B, N: Mo_2C@BCN NPs	290	94	[187]
Ni/Mo_2C (1:2)-NCNFs	270	133	[188]
Co_xMo_y@NC	330	218	[189]
MoO_2-FeP@C	244	103	[53]
PMo/ZIF-67-6-6N PMo/ZIF-67-6-7N	- 295	83 -	[190]
Co-Mo_2C-CN_x-2	338	92	[55]
Co_2P/Mo_3Co_3C/Mo_2C@C	362	186	[191]
Co@IC/MoC@PC	277	68	[166]
NG-NiFe@MoC_2	320	150	[192]
Co@β-Mo_2C-NC	330	188	[193]

Encouraged by the exceptional catalytic activities and durability of MoC-Fe@NCNTs in both HER and OER, an alkaline electrolyze was assembled using MoC-Fe@NCNTs as both anode and cathode (**Figure 5.19a**). As shown in **Figure 5.19b and c**, the MoC-Fe@NCNTs-based electrolyzer only required 1.66 V to achieve a water-splitting current density of 10 mA cm^{-2}, which is superior to that of MoC NCs (1.82). The i-t curves also show the excellent stability of the electrodes after 24 h (**Figure 5.19d**).

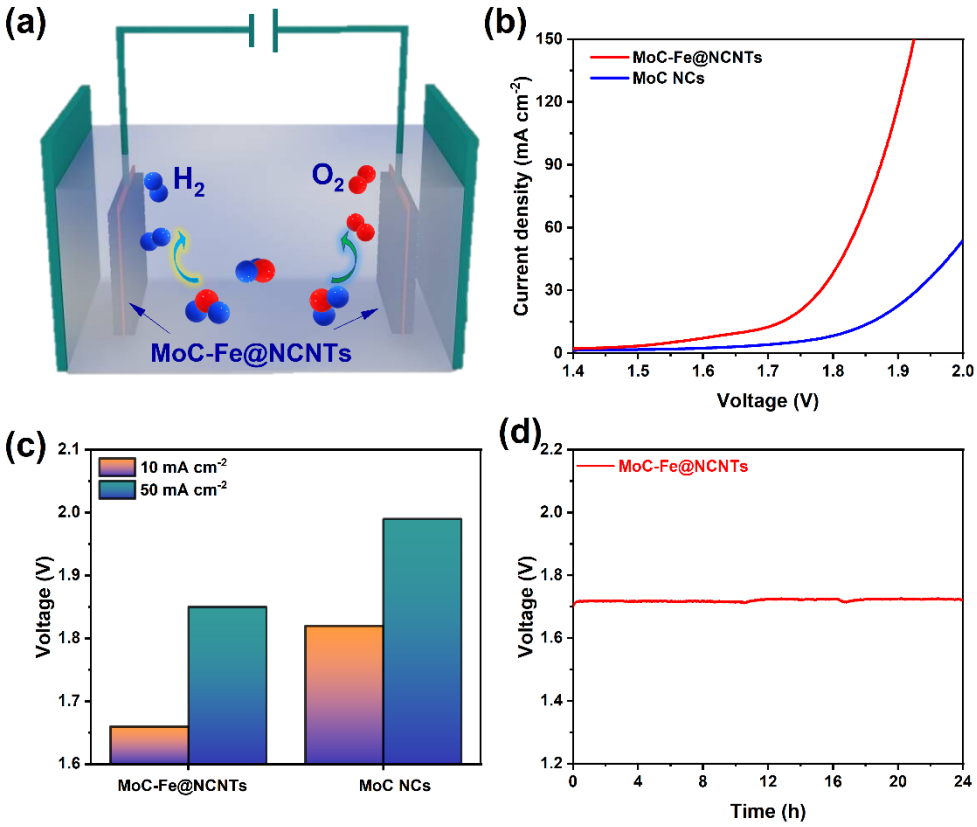

Figure 5.19. (a) Schematic illustration of water splitting; (b) polarization curves of MoC-Fe@NCNTs and MoC NCs toward overall water splitting; (c) comparison of the cell voltage at the current density of 10, 50 mA cm^{-2}; (d) i-t curve of MoC-Fe@NCNTs at 10 mA cm^{-2} for 24 h.

It also shows a faster rise in current density with increasing overpotential than that of noble Pt/C+RuO_2 catalyst, suggesting its potential applications where large current density is needed (**Figure 5.20**). The performance of MoC-Fe@NCNTs as a dual catalyst for overall water splitting is comparable to most non-precious metal-based catalysts **(Table 5.2)**.

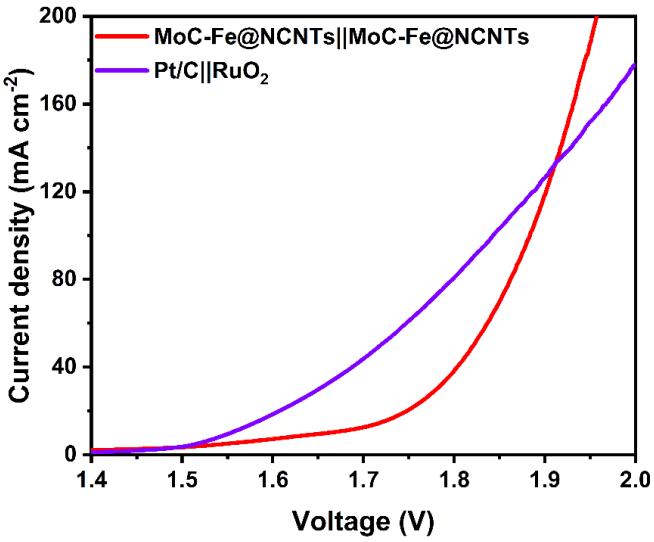

Figure 5.20. LSV curves towards overall water splitting in alkaline.

Additionally, TEM and HAADF-EDS mapping images of MoC-Fe@NCNTs after long-term electrolysis reveal that their structural integrity and cubical morphology are well maintained (**Figure 5.21**).

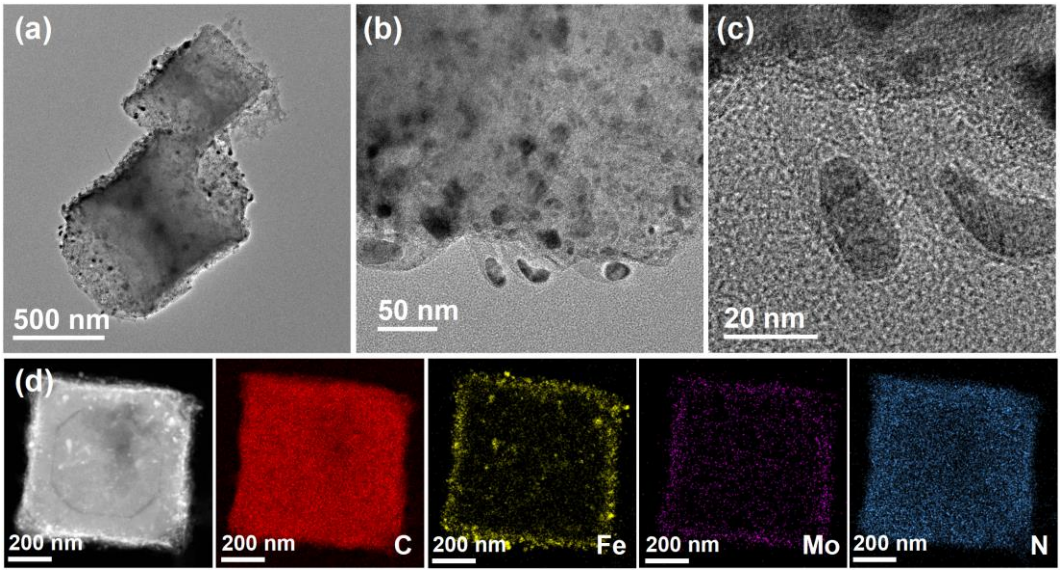

Figure 5.21. TEM and HAADF-EDS mapping images of MoC-Fe@NCNTs after long-term stability test.

Table 5.2. Comparison of the bifunctional water-splitting activity in 1.0 M KOH between MoC-Fe@NCNTs and other electrocatalysts.

Electrocatalyst	E_{10} (V)	References
MoC-Fe@NCNTs	**1.66**	**This work**
Co/β-Mo_2C@N-CNTs	1.64	*[186]*
Co_xMo_y@NC	1.74	[189]
Ni/Mo_2C (1:2)-NCNFs	1.64	[188]
MoO_2-FeP@C	1.592	[53]
Co-Mo_2C-CN_x-2	1.68	[55]
Co_2P/Mo_3Co_3C/Mo_2C@C	1.74	[191]
Co@IC/MoC@PC	1.57	[166]
Co@β-Mo_2C-NC	1.72	[193]
Ni/Ni_2P/Mo_2C@C	1.78	[191]
NG-NiFe@MoC_2	1.53	[192]

The outstanding stability of Fe and MoC nanoparticles can be ascribed to the protective graphite layers with solid adhesion. XPS analysis (**Figure 5.22**) suggests no change in chemical compositions after electrochemical testing, demonstrating the good stability of the MoC-Fe@NCNTs catalyst. Fe 2p XPS spectrum recorded after the stability test (**Figure 5.22c**) showed a broad peak consisting of several deconvoluted peaks corresponding to Fe^{2+}, Fe^{3+}, and a satellite peak, suggesting an inevitable surface oxidation during the electrocatalytic process.

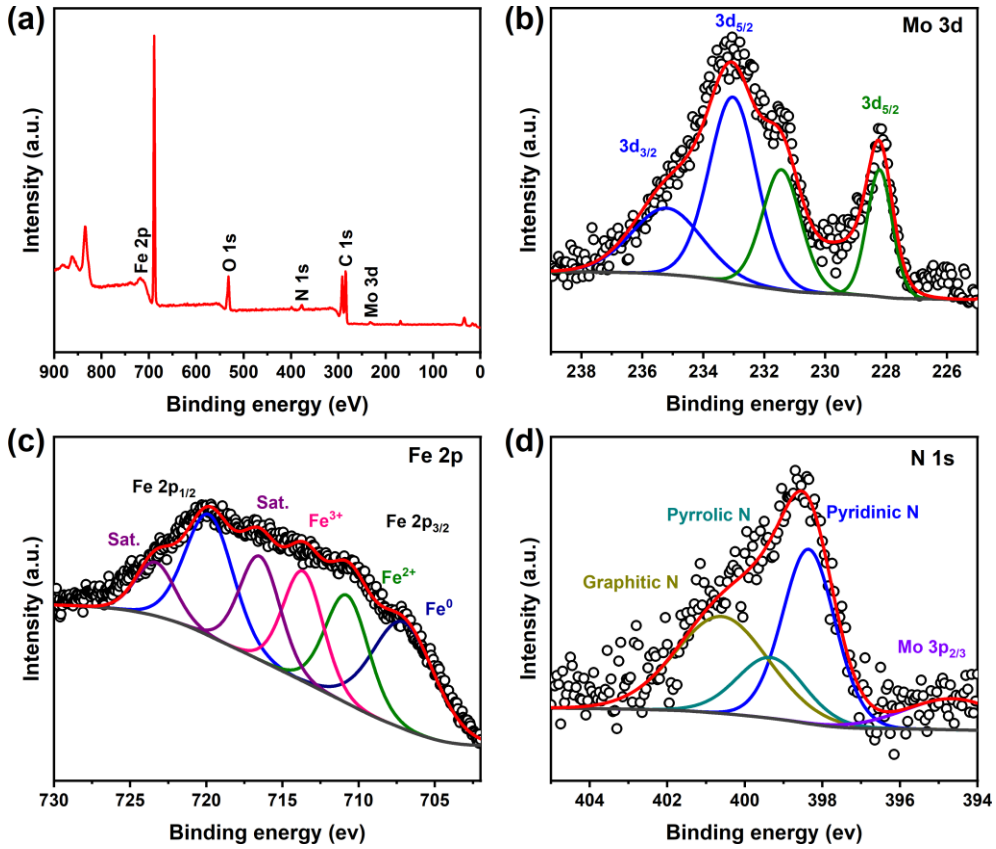

Figure 5.22. (a) Survey and high-resolution (b) Mo 3d, (c) Fe 2p, and (d) N 1s XPS spectra of MoC-Fe@NCNTs after long-term stability test.

To unveil the origin of bifunctional activity of MoC-Fe@NCNTs, density functional theory (DFT) calculations were performed. As shown in **Figure 5.23a**, an optimized framework of MoC-Fe heterojunction was built using MoC and Fe fragments. Models of MoC and Fe were also built separately for comparison, respectively (**Figure 5.23b and c**). The electron redistribution at the interface is described by the charge density difference of MoC-Fe in **Figure 5.23d**. There are lots of electrons accumulated at the interface, suggesting a strong electronic interaction between Fe and MoC, consistent with the XPS result, which is beneficial for water splitting. The total density of states (TDOS) was calculated in **Figure 5.23e**. MoC-Fe show a stronger delocalization of the electronic state at the Fermi level than those of both MoC and Fe, demonstrating an enrichment of charge

at the interfaces, which can facilitate for the intermediate adsorption and the oxidation reaction in HER/OER process.

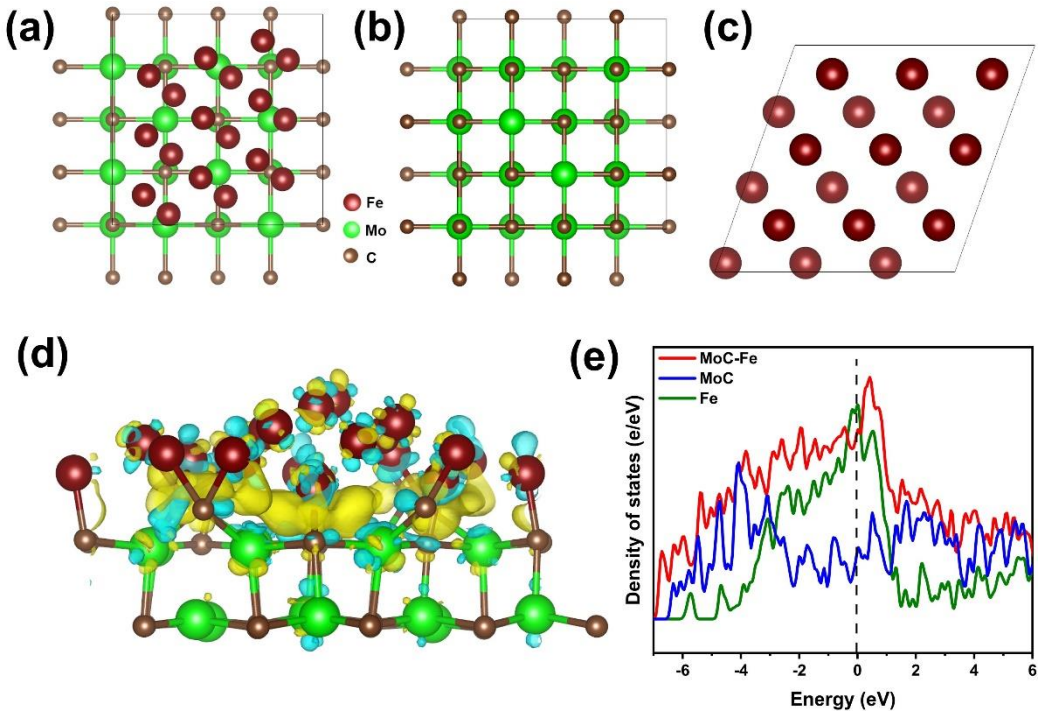

Figure 5.23. Schematic diagram of (a) MoC-Fe, (b) MoC and (c) Fe; (d) charge density distribution of MoC-Fe and (f) TDOS of MoC-Fe, MoC, and Fe.

The optimized models of H adsorption on MoC-Fe and corresponding hydrogen adsorption free energy (ΔG_{H*}), as an indicator of HER activity, are shown in **Figure 5.24a-d**. Clearly, the ΔG_{*H} for MoC-Fe is much smaller than those on MoC and Fe, indicating that H* adsorption on MoC-Fe is favorable for the HER process. Besides, the more negative ΔG_{H2O} value of MoC-Fe than that of MoC and Fe ensures thermodynamically favorable water adsorption on MoC-Fe and subsequent H_2O dissociation (**Figure 5.24e**) [194]. Therefore, the DFT calculations confirm the enhanced activity in dual-phase MoC-Fe is associated with the interface between MoC and Fe, which matches well with the above experimental results.

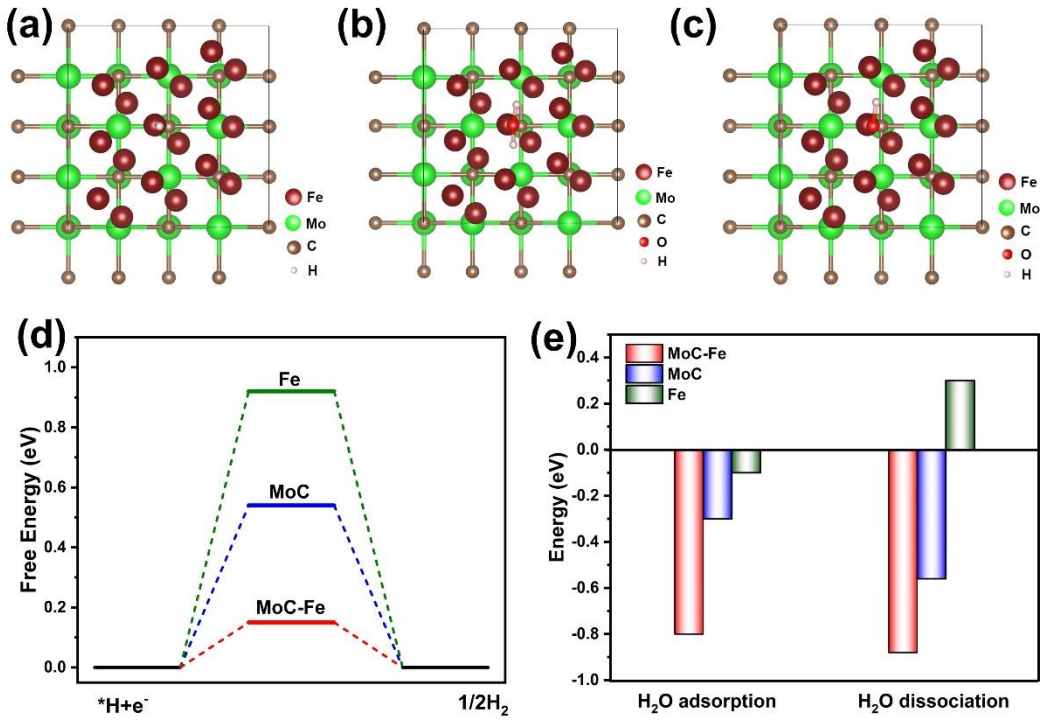

Figure 5.24. System of (a) H, (b) OH, and (c) H_2O adsorption on MoC-Fe. (d) Reaction free energies diagram of hydrogen evolution on MoC-Fe, MoC, and Fe. (e) H_2O adsorption and dissociation-free energies in various configuration.

5.4. Conclusion

In summary, for the first time, a novel hybrid nanocomposite MoC-Fe@NCNTs was prepared as an efficient and stable bifunctional electrocatalyst for water splitting. Introducing guest Fe species into the Zn/Mo-MOF framework results in the in-situ formation of N-doped carbon nanotubes on the Fe NPs during the pyrolysis process, which are beneficial for creating heterointerfaces between Fe and MoC NPs. Taking advantage of the strong synergistic effects between Fe and MoC NPs, porous structures with high accessibility to active sites, and the presence of NCNTs, the resultant MoC-Fe@NCNTs exhibited robust electrochemical performance with η_{50} values of 252 and 304 mV and Tafel slopes of 144 and 57 mV dec^{-1} for HER and OER, respectively. Remarkably, they afforded a stable current density of 10 mA cm^{-2} for overall water

splitting at 1.66 V with excellent stability. This work offers some guidelines for the fabrication of efficient MOF-derived bifunctional catalysts.

CHAPTER 6 Iron-Selenium Dual-Single-Atom Electrocatalysts for CO_2 Reduction

6.1. Introduction

Electrocatalytic CO_2 reduction reaction (CO_2RR) holds extraordinary significance for reducing anthropogenic CO_2 emission while producing valuable chemicals and fuels, such as CO, formic acid, CH_4, ethylene, and ethanol [8, 65]. Among these products, CO is the most desirable target since it is an economically practical feedstock in chemical and industrial applications [195]. To date, considerable efforts have been made to develop noble metal-based or molecular electrocatalysts for the electrochemical CO_2 reduction to CO in aqueous solutions [196, 197]. However, their catalytic performance is still unsatisfactory and substantially limited by the slow kinetic, poor durability, and competitive HER. Thus, it is of great interest to develop highly active and cost-effective electrocatalysts for practical CO_2 conversion.

Among various materials, single-atom catalysts (SACs) with isolated metal atoms anchored on conductive N-doped carbon substrates have become a new frontier in CO_2RR catalysis due to their maximum atomic efficiency and distinctive catalytic features [198-200]. Many SACs, such as Fe [201], Co [202], Ni [75], Zn [203], Bi [204], Mg [205], Mo [74], In [206] and Ag [207] single-atom catalysts, have been explored to selectively convert CO_2 into CO. However, the reported SACs still suffer from low metal loadings, high overpotential, low selectivity, and limited current density. To address the predicament of SACs, numerous approaches have been proposed to regulate the coordination of SACs to improve their electrocatalytic performance [82, 208, 209].

Recently, the construction of heteronuclear dual-single-atom electrocatalysts has been found effective in modifying the local environment around metal centers in SACs and offering extra accommodation sites, thereby greatly boosting CO_2 conversion [85, 89, 210, 211]. A second transition metal site adjacent to the first one could act as a promoter, enabling new reaction pathways. For example, Ren *et al.* reported a Ni/Fe-N-C catalyst with isolated Ni-Fe sites which exhibited better CO_2RR performance with high FE_{CO} (>90%) over a wide potential range, outperforming the single component-based catalysts [211]. Besides, axial heteroatom bridging can modulate the geometric and electronic structure of DACs, which can not only reduce the reaction barrier of key intermediates, but also retard the undesired HER, thereby boosting the catalytic performance [89, 212]. However, the development of DACs still suffers from the complex synthetic procedure and lack of understanding on the atomic configurations and interactions of dual sites. Therefore, it is highly desirable to develop novel methods to fabricate diatomic catalysts with highly active sites at the atomic scale and reveal their structure-performance relationship.

Herein, an electrocatalyst with atomically dispersed FeSA and SeSA was designed and synthesized, where two metal atoms were anchored on an N-doped carbon matrix derived from zeolitic imidazolate framework (ZIF-8). The critical role of SeSA as promoter atoms was revealed in enhancing the CO_2RR activity and selectivity by regulating the electronic structure of the atomic Fe centers and interaction between the intermediate and catalyst. A distinct synergistic effect was observed in the resultant FeSe-NC, which achieved a boosted CO_2 electroreduction performance affording industrial-level j_{CO} (>235.0 mA cm^{-2}) and high FE_{CO} (>95 %). Additionally, the as-prepared FeSe-NC used as the cathode for rechargeable Zn-CO_2 batteries (ZCB) delivered a power

density of up to 2.01 mW cm^{-2} at 0.27 V and high FE_{CO} (> 90%), further demonstrating its potential for practical application.

6.2. Experimental section

6.2.1. Catalyst synthesis

Synthesis of SeO_2-ZIF-8. First, 400 mg ZIF-8 (synthesis details are described in Chapter 5) was dispersed in 20 mL MeOH, and 20 mL aqueous solution containing 50 mg of SeO_2 was then added and aged for 30 min. After that, the SeO_2-ZIF-8 was collected by centrifugation, washed with methanol, and dried overnight at 60 under vacuum.

Synthesis of Se@NC. In a typical synthesis, SeO_2-ZIF-8 was transferred to a quartz tube and pyrolyzed at 1000 °C for 2 h with a ramping rate of 5 °C min^{-1} under Ar flow. After the sample was cooled down to room temperature naturally, the Se@NC was finally harvested. For comparison, NCs were also synthesized by a similar method in the absence of SeO_2.

Synthesis of FeSe-NC and Fe-NC. The as-prepared Se@NC was immersed in HCl solution (2.0 M) and stirred at 80 ℃ for 12 h to remove Zn species. The FeSe-NC catalyst was prepared via metal ions adsorption followed by thermal activation treatment by employing the Se@NC as a porous carbon host. For example, 50 mg of Se@NC powder was dispersed in 5 mL of isopropanol that contained 2.5 mg of $Fe(NO_3)_3{\cdot}9H_2O$. The as-obtained mixture was then sonicated for 1.0 h and stirred 2.0 h before being washed with methanol, centrifuged, and dried at 60 °C overnight to prepare the Se@NC-Fe^{3+} sample. Afterward, the obtained Se@NC-Fe^{3+} was subjected to heat treatment at 900 °C with a ramp rate of 10 °C min^{-1} for 1.0 h under Ar and cooled naturally to generate the final FeSe-NC catalyst. As another control, Fe-NC was obtained following almost the same procedure as FeSe-NC except that NC was used as the carbon host.

Synthesis of Se-NC. Se@NC was heated to 900 °C with a ramp rate of 10 °C min^{-1} for 1.0 h under Ar and cooled naturally to generate the final Se-NC catalyst.

6.2.2. Electrochemical measurement

H-type cell system. Electrochemical CO_2RR measurements were conducted in a gas-tight H-type cell, in which the anodic and cathodic chambers was separated by a proton exchange membrane (Nafion 117). Ag/AgCl (saturated KCl aqueous) electrode and Pt net were used as reference and counter electrodes, respectively. Before each experiment, CO_2 (99.999%) was constantly purged into the catholyte (30 mL) for 30 minutes to form a CO_2-saturated electrolyte. LSV curves was recorded in Ar or CO_2-saturated 0.5 M $KHCO_3$ electrolyte with a scan rate of 10 mV s^{-1}. All potentials reported here were converted to the RHE.

Flow cell system. Electrochemical experiments were performed in a flow cell reactor with gas, cathode, and anode chambers. The catalyst-supported gas diffusion electrode (GDE) with a mass loading of 1 mg cm^{-2}, Ag/AgCl (saturated KCl aqueous) electrode, and nickel foam were used as the cathode, reference electrode, and anode, respectively. Copper tapes were used to connect the cathode and anode respectively. The anolyte and catholyte chamber was separated by a piece of anionic exchange membrane (Fumasep FAB-PK-130). 80 mL electrolyte (1 M KOH, pH ≈14.0) was circulated in the cathode and anode chamber using a peristaltic pump at a constant flow of 30 mL min^{-1}. High-purity CO_2 was directly fed to the backside of the cathode GDE at a constant flow of 40.0 sccm using a digital mass flow controller, and CO_2 output was connected to a GC system.

6.2.3. Rechargeable Zn-CO_2 battery measurement

The aqueous rechargeable Zn-CO_2 electrochemical cell was assembled using single atom catalysts as the cathode, and a Zn plate with an area of 2 × 5 cm^2 as the anode. CO_2-saturated 1 M $KHCO_3$ and 6 M KOH + 0.2 M $Zn(CH_3COO)_2$ were used as catholyte and anolyte, respectively. The two compartments were separated by a bipolar membrane. During the discharging process, CO_2 was flew into the cathode compartment at a rate of 20 mL min^{-1}. All the tests were conducted in a double-electrolyte system.

During the discharge process, the half-reactions on the electrode can be described as follow [213]:

Cathode (1 M $KHCO_3$ sat. CO_2):

$CO_2 + 2H^+ + 2e^- \rightarrow CO + H_2O$ $\quad E°= -0.106$ V vs SHE

Anode (6 M KOH with 0.2 M $Zn(CH_3COO)_2$):

$Zn - 2e^- \rightarrow Zn^{2+}$

$Zn^{2+} + 4OH^- \rightarrow Zn(OH)_4^{2-}$ $\quad E°= -1.199$ V vs SHE

Overall reaction: $Zn + CO_2 + 2H^+ + 4OH^- \rightarrow Zn(OH)_4^{2-} + CO + H_2O$

6.3. Results and discussion

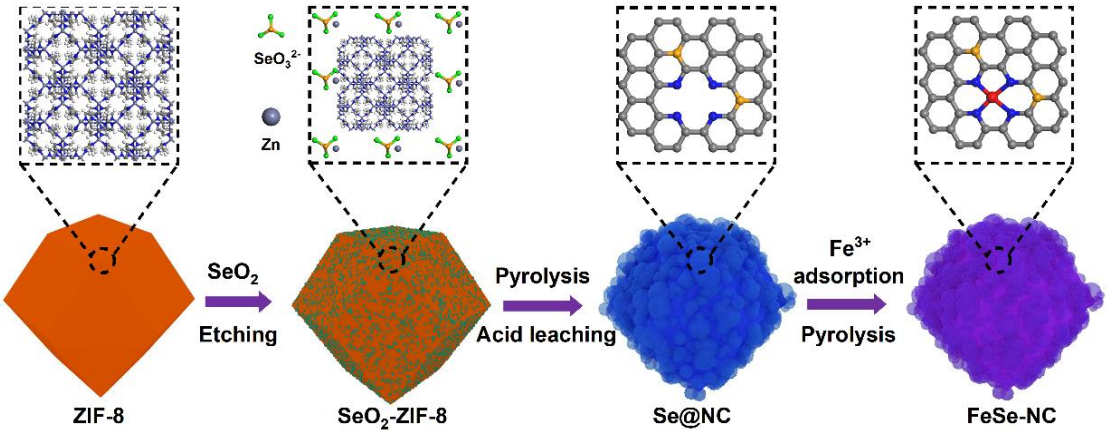

Figure 6.1. Schematic illustration of the synthesis for FeSe-N-C.

The FeSe-N-C electrocatalyst was prepared through a three-step process (**Figure 6.1**). Specifically, ZIF-8 etched by SeO_2 (SeO_2-ZIF-8) was first prepared through the mechanical stirring of SeO_2 and ZIF-8 in a methanol aqueous solution. The aqueous solution of SeO_2 is a weak selenous acid, which can gradually etch the ZIF-8 framework to produce SeO_2-ZIF-8. PXRD patterns of (**Figure 6.2**) the products after etching for 30 min reveal only the crystal structure ZIF-8 and no diffraction peaks corresponding to SeO_2 can be observed, demonstrating its amorphous nature.

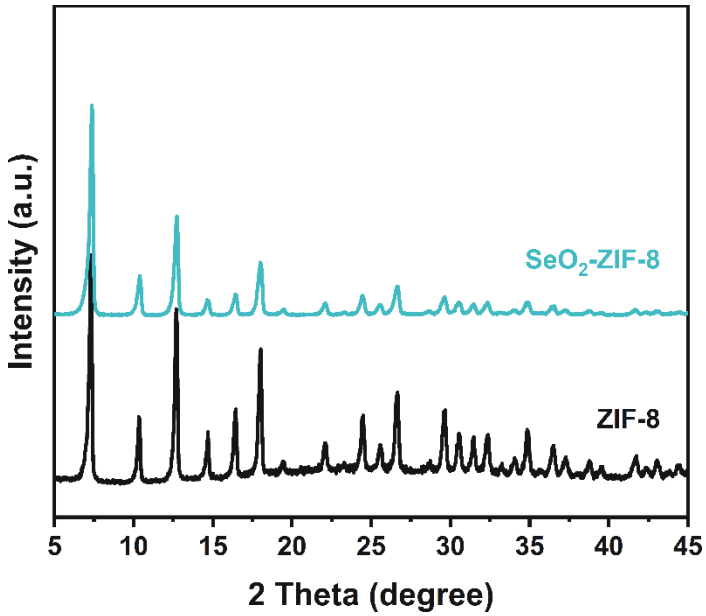

Figure 6.2. PXRD patterns of ZIF-8 and SeO_2-ZIF-8.

Compared with pristine ZIF-8 which features a rhombic dodecahedron morphology and smooth surface (**Figure 6.3a**), the as-obtained SeO_2-ZIF-8 maintained the dodecahedral morphology but with rougher surfaces (**Figure 6.3b**). The representative EDS elemental analysis (**Figure 6.3c**) also confirmed the existence of Se, suggesting the successful etching of ZIF-8 by SeO_2.

Subsequently, the SeO_2-ZIF-8 precursor was annealed at 1000 °C and the product was collected and then analyzed by PXRD. As shown in the PXRD pattern (**Figure 6.4**), the resultant product displays no peaks of SeO_2 but typical diffraction peaks of Se,

indicating the formation of Se species in the NC substrates during the pyrolysis. During the treatment, SeO_2 was first evaporated and then reduced to Se by NC at a high temperature. The formed Se species were trapped and anchored on the NC skeleton, thus yielding the Se@NC.

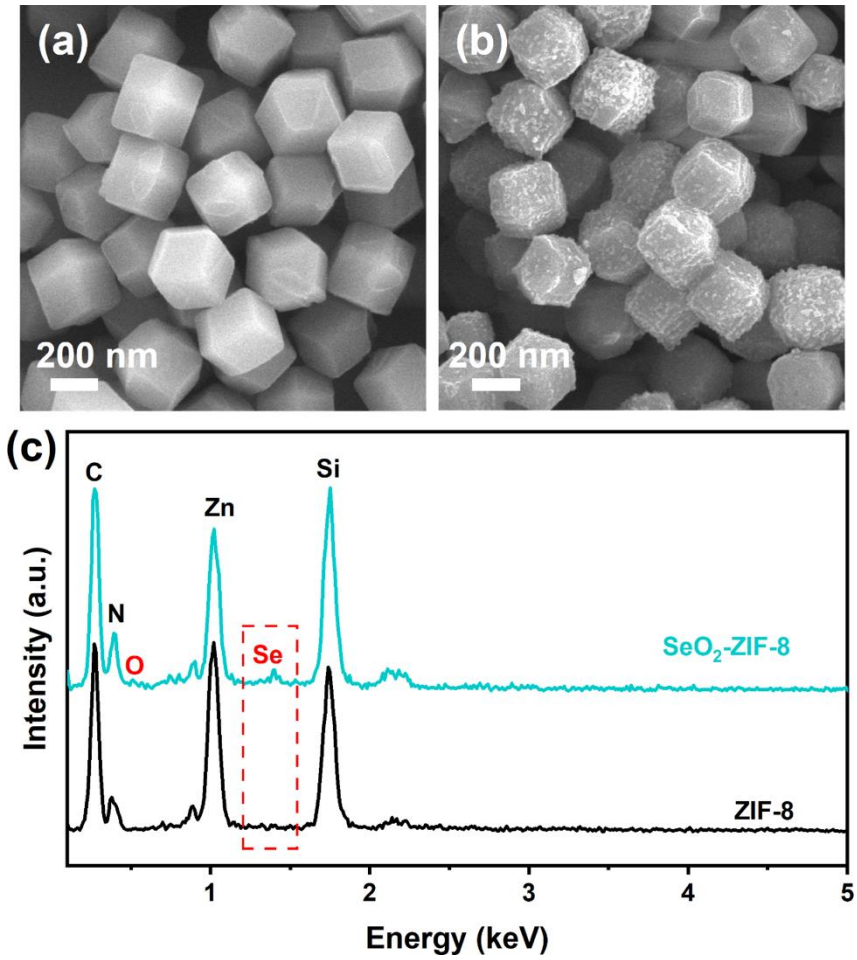

Figure 6.3. FESEM images of (a) ZIF-8, (b) SeO_2-ZIF-8, and (c) the representative EDS elemental analysis.

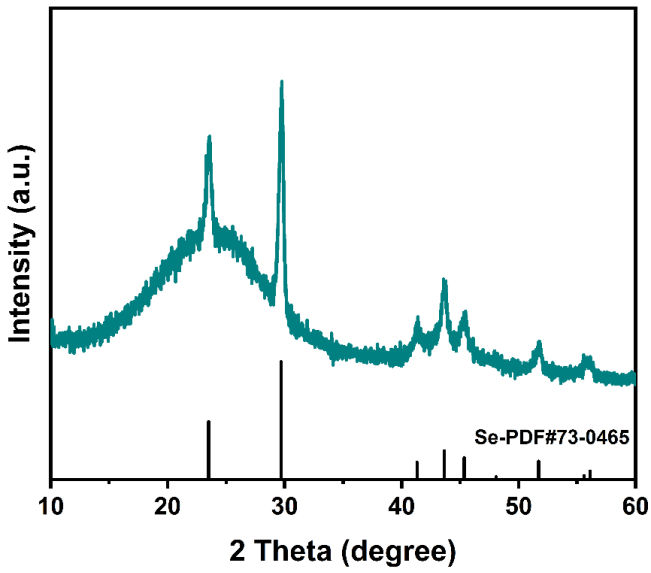

Figure 6.4. PXRD pattern of the obtained Se@NC.

The resultant Se@NC was used to adsorb Fe^{3+} ions through trapping by nitrogen dopants and micropores, which was denoted as Se@NC-Fe^{3+}. A final thermal activation promotes the embedding of Fe and Se into the N-doped carbon skeleton (**Figure 6.1**). Similarly, the Fe-NC without Se source was also prepared for comparison. FESEM and TEM images show that FeSe-NC well inherits the original shape and morphology with some shrinkage (**Figure 6.5a, b**). Moreover, compared with smooth Fe-NC particles, the surface of FeSe-NC and Se-NC particles are much rougher as a result of SeO_2 etching. A large number of cavities appear on the surface of FeSe-NC, which can increase the exposure of Fe/Se sites and facilitate the mass transfer during CO_2RR.

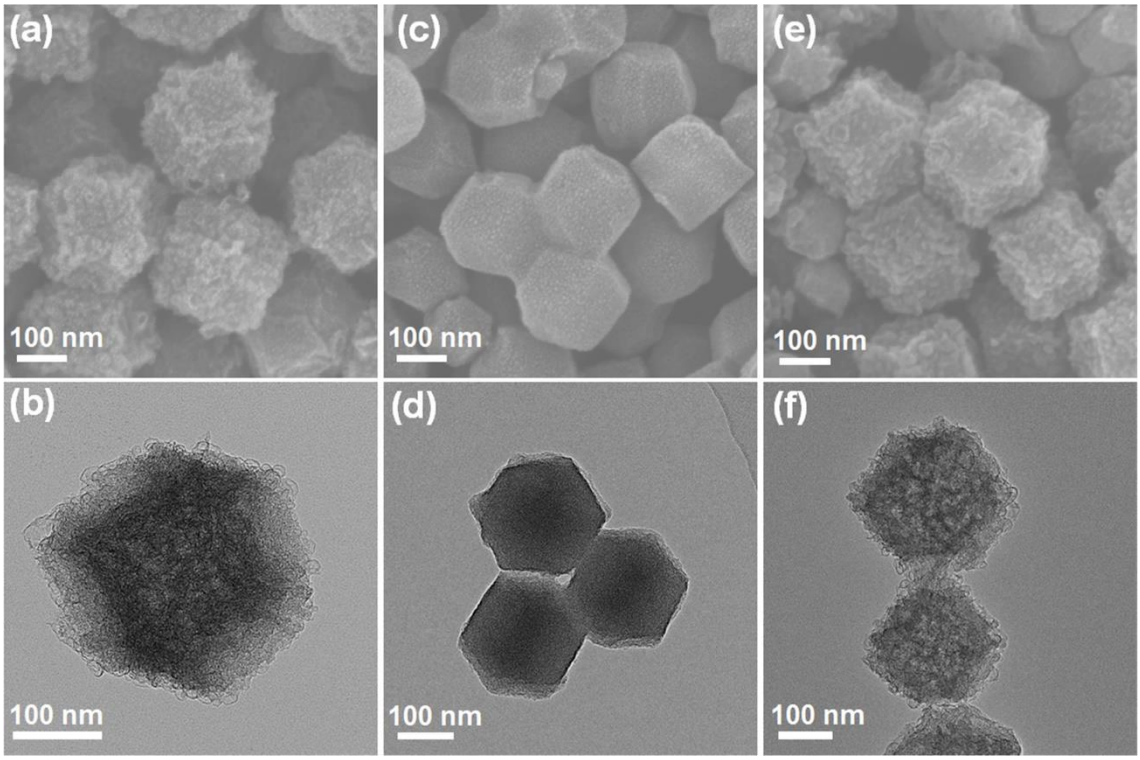

Figure 6.5. FESEM and TEM images of (a, b) FeSe-NC, (c, d) Fe-NC and (e, f) Se-NC.

Besides, as shown in **Figure 6.6a**, large Fe/Se nanoparticles or clusters were not observed in these catalysts by HRTEM, suggesting Fe, Se, and Fe-Se moieties exist as a monodispersed state. To further confirm this, AC HAADF-STEM was employed, and only bright spots in the atomic range could be found in the matrix, reflecting the atomic dispersion of Fe and Se atoms in FeSe-NC (**Figure 6.6b**). Especially in FeSe-NC, there are many adjacent dual dots with different contrasts at a distance of 2-4 Å, marked by yellow frames, indicating the formation of diatomic configurations. Meanwhile, the HAADF-STEM image and corresponding EDS elemental mappings show a uniform distribution of C, N, Se and Fe throughout the polyhedra of FeSe-NC (**Figure 6.6c-g**). Similarly, TEM and EDS mapping images also verify the atomic dispersion of Fe, Se atoms in the shrinked rhombic dodecahedral Fe-N-C (**Figure 6.6.** (a) HRTEM, (b) AC HAADF-STEM and (c-g) EDS elemental mapping images of FeSe-NC; (h-k) EDS elemental mapping images of Fe-NC; (i-o) EDS elemental mapping images of Se-NC.)

and Se-NC (**Figure 6.6.** (a) HRTEM, (b) AC HAADF-STEM and (c-g) EDS elemental mapping images of FeSe-NC; (h-k) EDS elemental mapping images of Fe-NC; (i-o) EDS elemental mapping images of Se-NC.), respectively.

Besides, only two broad diffraction peaks (24° and 42°) can be observed in PXRD patterns (**Figure 6.7**), which can be assigned to (002) and (101) planes of graphitic carbon, further excluding the presence of crystalline metallic or oxide crystals.

Raman spectra of all samples exhibit characteristic D band (1350 cm^{-1}) and G band (1592 cm^{-1}) (**Figure 6.8**) of carbon. The I_D/I_G values of FeSe-NC and Se-NC are higher than that of Fe-NC, demonstrating that selenic-acid etching and subsequent Se doping in the carbon matrix introduced additional defects, which is consistent with the above TEM results.

Additionally, N_2 adsorption-desorption isotherms indicate that these products with hierarchically porous structures possess large surface areas (**Figure 6.9**), which is beneficial to the exposure of more active sites and accelerate substrates penetration, thereby improving the electrocatalytic performance.

The ICP-OES analysis reveals that the mass loadings of Fe and Se in FeSe-NC are 0.51 wt% and 1.89 wt% (**Table 6.1**), respectively, which is similar to that of Fe-NC (Fe: 0.48 wt%) and Se-NC (Se: 2.29 wt%).

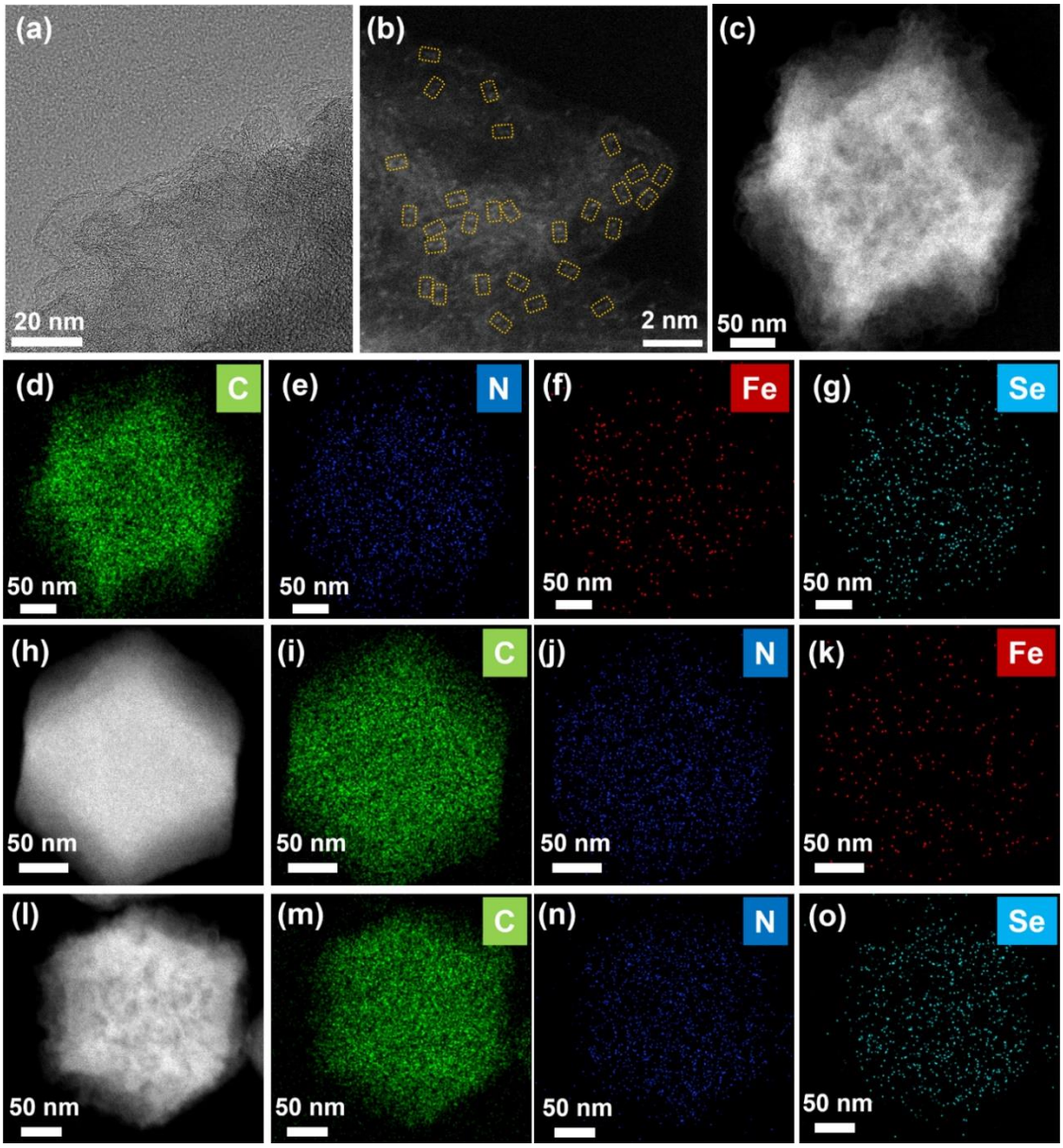

Figure 6.6. (a) HRTEM, (b) AC HAADF-STEM and (c-g) EDS elemental mapping images of FeSe-NC; (h-k) EDS elemental mapping images of Fe-NC; (i-o) EDS elemental mapping images of Se-NC.

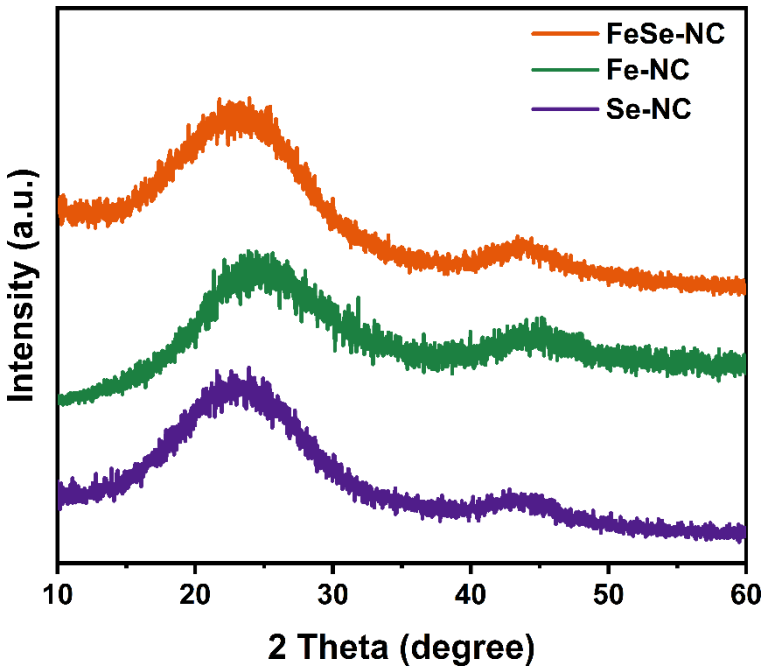

Figure 6.7. Powder XRD patterns of FeSe-NC, Fe-NC, and Se-NC.

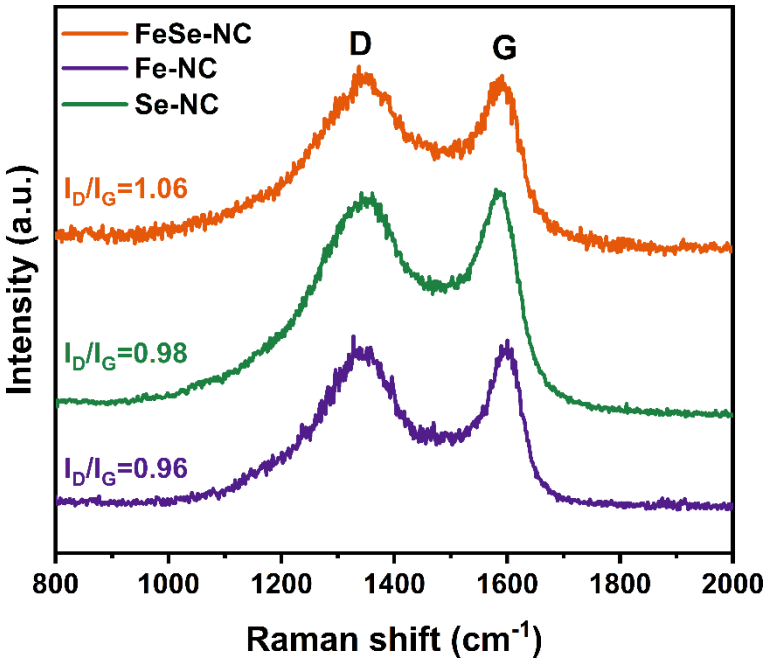

Figure 6.8. Raman spectra of FeSe-NC, Fe-NC and Se-NC.

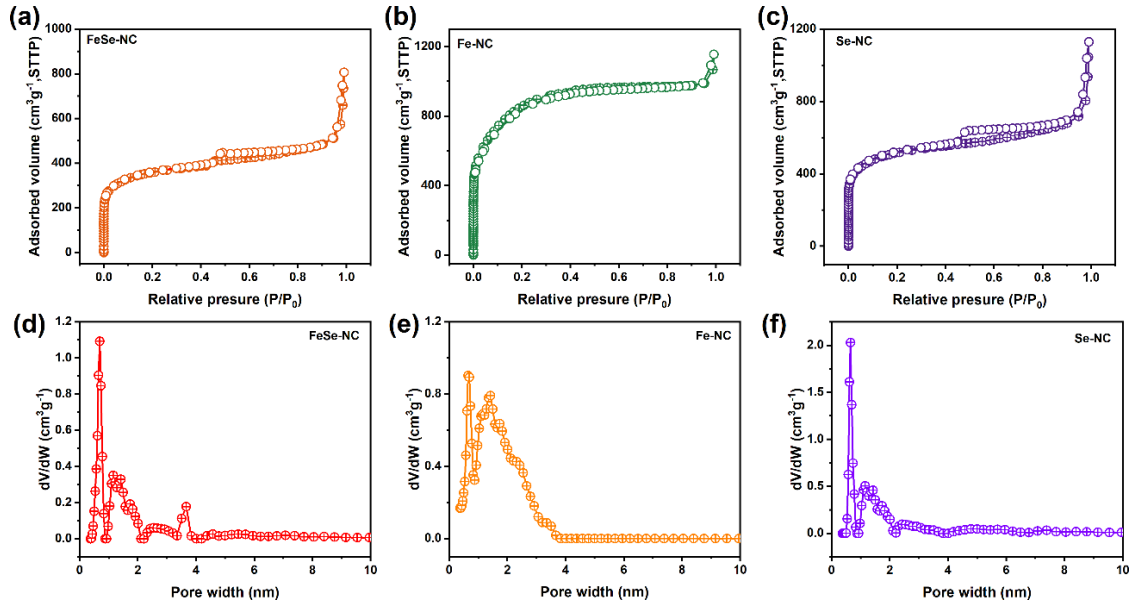

Figure 6.9. N_2 sorption isotherms and the corresponding pore size distributions of (a,d) FeSe-NC, (b,e) Fe-NC and (c,f) Se-NC at 77 K.

Table 6.1. Content of elements in the as-synthesized samples obtained from ICP-OES.

Catalyst	FeSe-NC	Fe-NC	Se-NC
Se (wt%)	1.89	-	2.29
Fe (wt%)	0.51	0.48	-

The elemental composition and chemical states were explored by XPS, as shown in **Figure 6.10a**. Survey spectra demonstrate the presence of C, O, and N in all samples, while Se only exists in FeSe-NC and Se-NC. However, the signal of Fe is very weak due to its low content. The high-resolution N 1s XPS spectra suggest all three samples possess pyridinic N (398.5 eV), pyrrolic N (400.6 eV), graphitic N (401.4 eV), and oxidized N (403.1 eV) species (**Figure 6.10b**). Compared with Se-NC, the extra peak (399.5 eV) in FeSe-NC and Fe-NC products can be assigned to Fe-N. Regarding Se 3d spectra (**Figure**

6.10c), the main peak at 56.4 eV can be assigned to Se-C bond. The minor peak at 58.4 eV is ascribed to the oxidized Se moiety. The Fe 2p XPS spectrum reveals the oxidation states of Fe in both FeSe-NC and Fe-NC are close to +2 (**Figure 6.10d**). Moreover, compared with Fe-NC, the binding energy of Fe $2p_{3/2}$ peak of FeSe-NC slightly shifts to lower energy, suggesting a low-valence state. Similar observations have also been observed in previous studies, which may be induced by the neighboring heteroatoms doping.

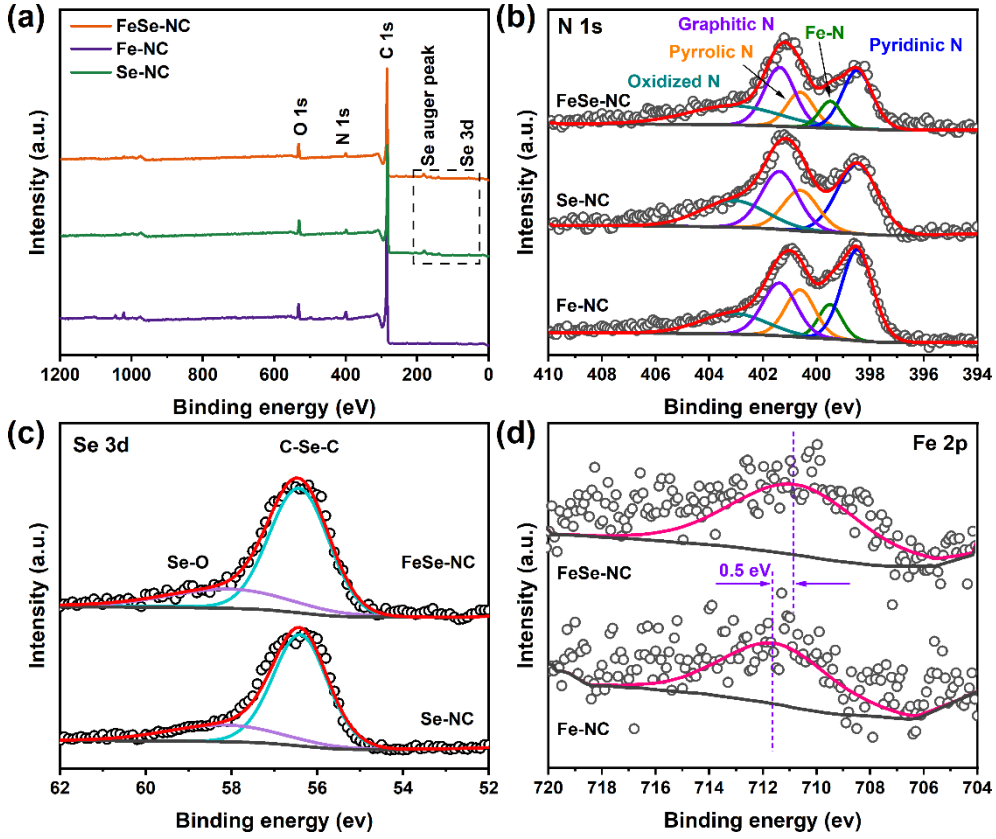

Figure 6.10. XPS analysis of as-obtained products: (a) survey and (b) N 1s spectra of FeSe-NC, Fe-NC and Se-NC; (c) Se 3d spectra of FeSe-NC and Se-NC; (d) Fe 2p spectra of FeSe-NC and Fe-NC.

The electrocatalytic CO_2RR performance over the as-prepared catalysts was first evaluated in a typical H-type cell. CO_2-saturated 0.5 M $KHCO_3$ was used as the electrolyte in H-cell. As illustrated by the polarization curves in **Figure 6.11a**, FeSe-NC presented

the smallest onset potential and highest total current density over the entire potential range compared to Fe-NC and Se-NC. Meanwhile, FeSe-NC delivered a much higher current density than the value recorded in the Ar-saturated $KHCO_3$ solution, manifesting its efficient CO_2RR activity. Moreover, constant potential electrolysis was performed to investigate the FE of the products. The gas- and liquid-phase products for CO_2RR were quantitatively analyzed via online GC and offline ^1H NMR spectroscopy, respectively, and the results indicate that H_2 and CO are the only detectable products. As shown in **Figure 6.11b**, FeSe-NC exhibits superior CO selectivity with the highest FE_{CO} in comparison with Fe-NC and Se-NC across all test potentials. Specifically, FE_{CO} of FeSe-NC reached a maximum of 96.4% at −0.48 V (vs. RHE, the same below), outperforming that of Fe-NC (93%) and Se-NC (90%), and maintained >90% in a wide potential window from −0.38 to −0.68 V. Moreover, the CO partial current density (j_{CO}) of FeSe-NC is much higher than the other two comparison samples across the entire potential window (**Figure 6.11c**). Specifically, FeSe-NC delivered a j_{CO} of about −33.2 mA cm^{-2} at −0.78 V, which is 2.14 times and 3.49 times higher than that of Fe-NC (−15.5 mA cm^{-2}) and Se-NC (−9.5 mA cm^{-2}), respectively, indicating its superior CO_2RR activity. The Tafel slope of FeSe-NC was determined to be 228 mV dec^{-1} (**Figure 6.11d**), which is significantly lower than those of Fe-NC (240 mV dec^{-1}) and Se-NC (325 mV dec^{-1}), indicating a greatly accelerated kinetics for CO production over FeSe-NC. Besides, ECSA based on the electrochemical double layer accords well with the trend of CO_2RR activity (**Figure 6.11e-h**). Besides, the long-term electrolysis stability of FeSe-NC and Fe-NC was further measured and there was no obvious change in the current density and FE_{CO} of FeSe-NC under continuous 12 h potentiostatic electrolysis (**Figure 6.11i**). The combined XRD, TEM and XPS results of the FeSe-NC catalyst after electrochemical

testing reveals no change in crystal structure, morphology and chemical states of the elements, proving its chemical stability.

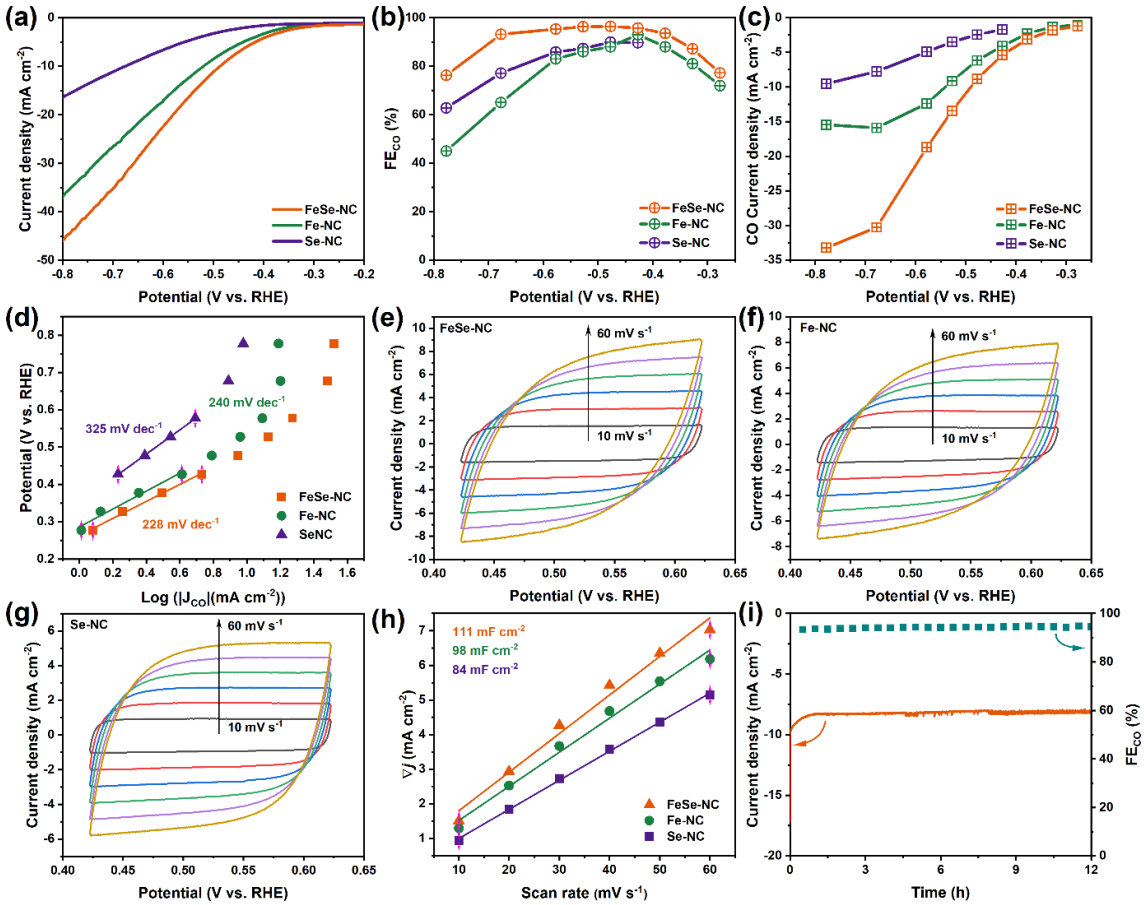

Figure 6.11. (a) LSV curves, (b) CO Faradaic efficiencies, (c) CO partial current densities and (d) Tafel plots, (e-g) CV curves at various scan rates, (h) the corresponding C_{dl} of three catalysts and (i) long-term stability test of FeSe-NC in H-type cell.

Control experiments indisputably indicate that the atomic Fe-N_x centers should be the intrinsically active sites, and the content of the doped Se, as well as the etching time, has little effect on the structure, morphology and CO_2RR performance of FeSe-N-C catalysts (**Figure 6.12**).

To overcome the mass transfer limitation of CO_2, the electrocatalytic activities of the as-prepared catalysts were evaluated in a self-designed flow cell reactor (**Figure 6.13a**), in which the electrocatalyst loading on the GDE was used as the cathode, nickel foam as

anode and 1.0 M KOH as the electrolyte. As displayed in LSV curves (**Figure 6.13b**), the reaction current density of FeSe-NC and Fe-NC were significantly increased in the flow cell, as compared to those obtained in the H-type cell, proving the superiority of this flow cell configuration. Compared with Fe-NC and Se-NC, FeSe-NC exhibited the highest FE_{CO} and j_{CO} at any potential. Moreover, the FE_{CO} of FeSe-NC reached 99.3% at 50 mA cm^{-2} and maintained above 95% in the potential range from −0.08 to −0.78 V (**Figure 6.13c**). Not only that, the j_{CO} of FeSe-NC reached 236 mA cm^{-2} at −0.88 V, which is more than 7 times that in the H-type cell (**Figure 6.13d**). As for Fe-NC, despite with a similar maximum FE_{CO} (99.2%), the FE_{CO} of Fe-NC dropped sharply as the potential exceeded −0.6 V, which may be due to the higher CO coverage that caused the poisoning of the Fe-N sites at high potentials, consistent with a reported observation [214]. The enhanced CO_2RR performance of FeSe-NC, especially at high CO coverage, can be attributed to the inhibition of the poisoning of the single-atom Fe sites through electronic structure regulation induced by SeSA [74]. FeSe-NC also exhibited outstanding durability for CO_2RR, maintaining FE_{CO} at a high level (>90%) after 7 hours of continuous electrolysis (**Figure 6.13e**).

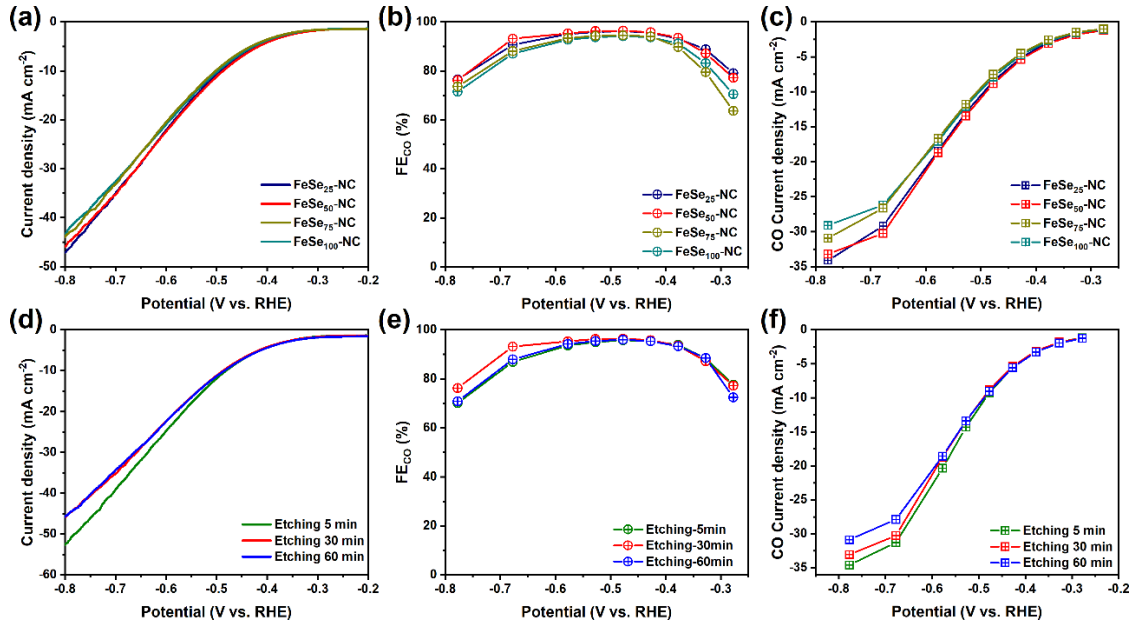

Figure 6.12. The CO_2RR performance of FeSe-NC catalysts prepared with (a-c) different content of Se and (d-f) different etching times.

Table 6.2. Comparison of the electrocatalytic CO_2RR performance in H-type cell of FeSe-NC with other carbon-based single-atom electrocatalysts.

Electrocatalysts	Electrolyte	[a]E_{app}	[b]FE_{CO} (%)	[c]j_{CO} (mA cm^{-2})	Refs.
FeSe-NC	**0.5 M $KHCO_3$**	**−0.48**	**96.4**	**8.9**	**This work**
Fe-NS-C	0.5 M $KHCO_3$	−0.56	93	12.1	[215]
Fe-N-C	0.5 M $KHCO_3$	−0.47	85	1.28	[216]
Fe-NC-S	0.5 M $KHCO_3$	−0.4	93	4	[217]
Fe_3C/Fe_1N_4	0.5 M $KHCO_3$	−0.5	94.6	1	[218]
Fe_1NC/S_1-1000	0.5 M $KHCO_3$	−0.5	96	5	[219]
Fe^{3+}-N-C	0.5 M $KHCO_3$	−0.45	94	16	[214]
Fe-SAC/NPC	0.5 M $KHCO_3$	−0.53	98	11	[220]
$FeN_4Cl/_{NC}$-7.5	0.5 M $KHCO_3$	−0.6	90.5	9.8	[221]
Fe-N-C	0.5 M $KHCO_3$	−0.56	49.7	~3	[222]
O-Fe-N-C	0.5 M $KHCO_3$	−0.5	95	4.4	[209]
Ni SAs/N-C	0.5 M $KHCO_3$	−1	70.3	7.36	[75]
Se-CNs	0.1 M $KHCO_3$	−0.6	78	11.5	[223]
MoSA-SeSA	0.1 M $KHCO_3$	−0.6	98.3		[74]
ZIF-NC-Ni-Fe	0.1 M $KHCO_3$	−0.6	97.8	~7.5	[85]
InNi DS/NC	0.5 M $KHCO_3$	−0.7	96.7	-	[89]
Ni/Fe-N-C	0.5 M $KHCO_3$	−0.7	98	7.4	[211]

[a]***E*app.**: The applied potential to get the maximum FECO; [b]$\mathbf{FE_{CO}}$: The maximum FE_{CO} values; [c]***jCO***: The *jCO* at the maximum FE_{CO}.

Meanwhile, SEM and TEM images show that the morphology and structure of FeSe-NC maintained the same during long-term electrolysis at high current density (**Figure 6.14**).

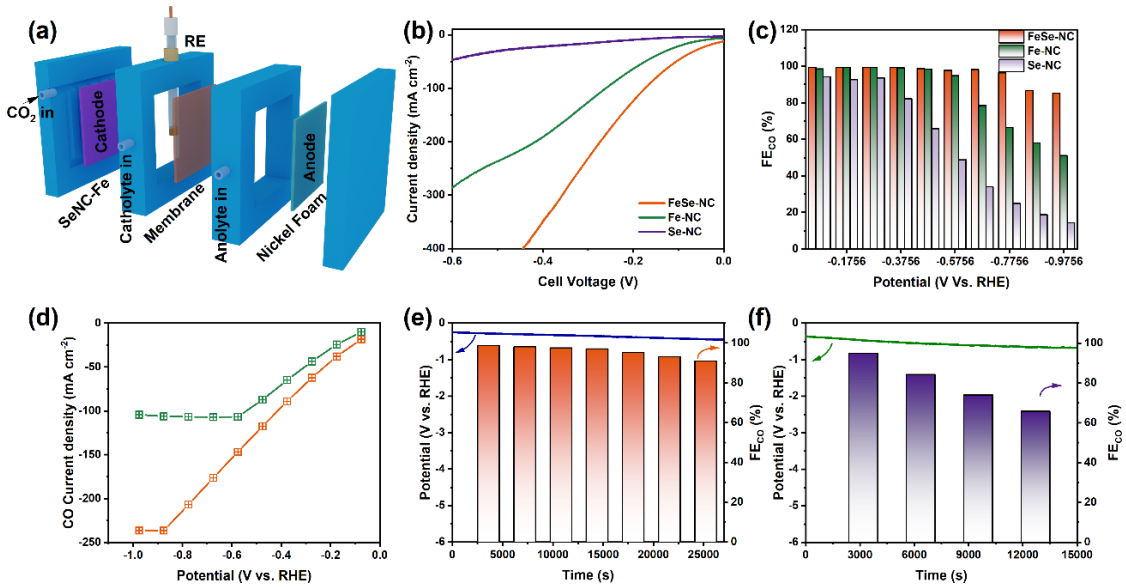

Figure 6.13. (a) Schematic illustration of the self-designed flow cell. (b) LSV curves. (c) FEs and (d) CO partial current densities at different potentials for CO generation. Long-term test of (e) FeSe-NC and (f) Fe-NC using 1.0 M KOH as the electrolyte.

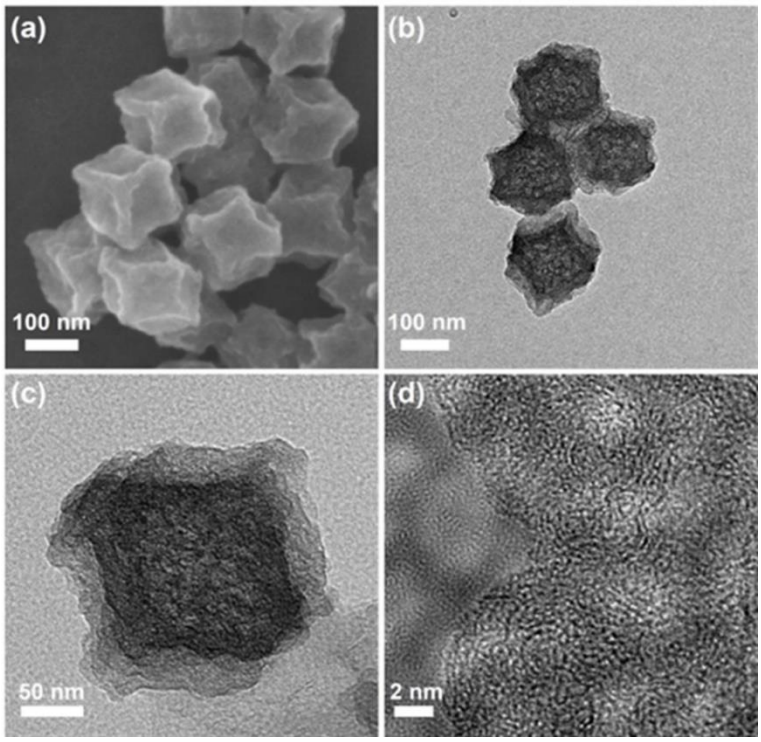

Figure 6.14. (a) SEM and (b-d) TEM of FeSe-NC after long-term stability test.

Given the excellent CO_2RR performance, liquid rechargeable Zn-CO_2 batteries (ZCB) with FeSe-NC as the cathode were assembled to assess its performance (**Figure 6.15**). As shown in **Figure 6.15b**, the ZCB with FeSe-NC cathode exhibited the best performance. Specifically, ZCB driven by FeSe-NC achieved a peak power density of 2.01 mW cm^{-2} at 0.27 V with a current density of 7.43 mA cm^{-2}, much higher than those of Fe-NC cathodic catalyst (1.83 mW cm^{-2}, 6.68 mA cm^{-2}). Moreover, compared with Fe-NC, FeSe-NC possessed higher output potential and FE_{CO} (94.1-97.3%) when discharged at various current densities ranging from 0.5 to 10 mA cm^{-2}. (**Figure 6.15c**). Furthermore, as displayed in **Figure 6.15d**, superior durability was demonstrated for FeSe-NC-based ZCB with a stable output voltage and high FE_{CO} over 12 h during the discharge process at a constant current density of 2 mA cm^{-2}. Moreover, the comparison of discharge and charge polarization curves shown in **Figure 6.15e** suggests a smaller voltage gap of FeSe-NC. Consequently, FeSe-NC-based ZCB exhibit an impressive

rechargeable durability with a stable narrow charge-discharge gap of only 1.34 V at 0.5 mA cm^{-2} over continuous operation for 40000 s (**Figure 6.15f**).

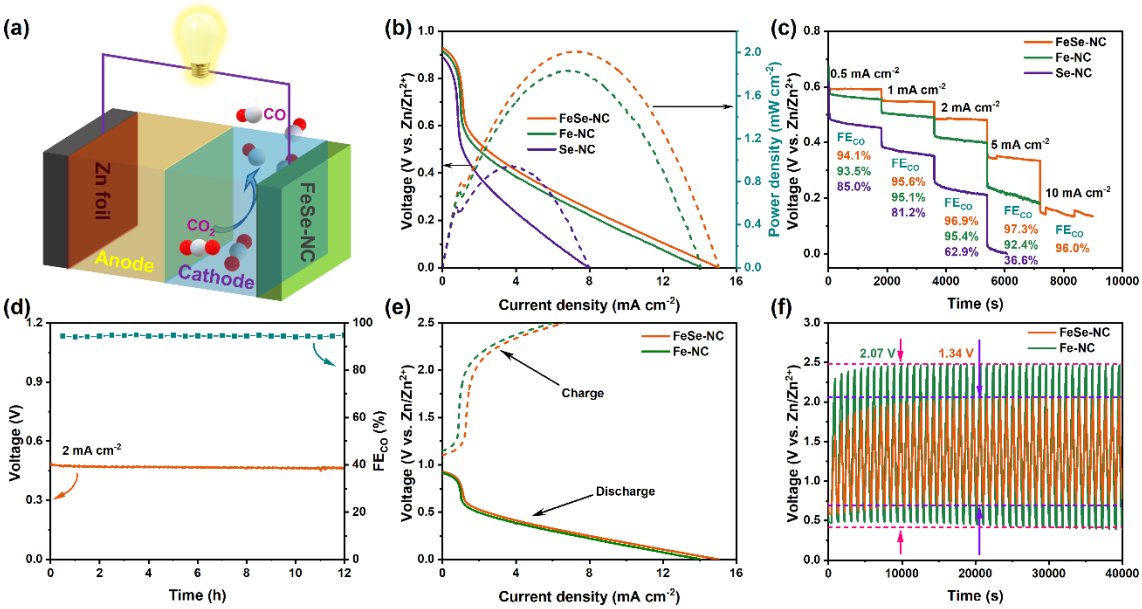

Figure 6.15. Zn-CO_2 battery measurements. (a) Schematic configuration of the ZCB with FeSe-NC cathode. (b) Discharge polarization and power density curves. (c) Discharge curves at different current densities and corresponding FE_{CO}. (d) Galvanostatic discharge curves and corresponding FE_{CO} at 2 mA cm^{-2}. (e) Discharge-charge polarization curves. (f) Galvanostatic discharge-charge cycling curves at 0.5 mA cm^{-2}.

6.4. Conclusion

In summary, a MOF-derived Fe-Se dual-single-atom catalyst was prepared via selenic-acid-assisted pre-etching and subsequent thermal activation. Notably, the as-obtained FeSe-NC exhibited an exceptional CO selectivity with high FE_{CO} (>95%) and simultaneously delivered an industrial-level j_{CO} up to 236 mA cm^{-2} at −0.88 V, which is much better than that of Fe-NC without Se doping and also outperformed the state-of-the-art Fe-based single-atom electrocatalysts. Comprehensive analyses reveal the important role of Se atoms in modulating the electronic structure of central Fe atoms, which can enable the desorption of *CO intermediate so to inhibit the poison of Fe-N_x

site under high CO coverage, thereby significantly boosting electrochemical CO_2 conversion, especially at high current densities. This work not only provides a new opportunity to realize impressive CO_2RR electrocatalysts but also sheds light on atomic-level structure engineering of dual-site catalysts for energy catalytic conversion.

CHAPTER 7 Conclusions and outlooks

7.1. Conclusion

In this thesis, the design and synthesis of MOF-derived high-performance electrocatalysts are aimed to be accomplished for water splitting and CO_2 reduction. Using structural, interfacial, and atomic engineering, several efficient MOF-derived catalysts including TM-based LDHs, carbide, and SACs, have been successfully prepared and tested. The conclusions are summarized as below.

First, novel bimetallic LDH nanocages with functional oxalate groups have been developed. A facile etching-doping-coordination strategy was put forward to synthesize MOF-derived CoFe oxalate nanocages starting from a ZIF-67 precursor. By controlling etching time and temperature, nanocages with different structures (hollow and yolk-shell) can be easily obtained. The ultrathin nanosheet subunits, Fe incorporation, and the presence of electron-rich oxalate group, all work together endowing CoFe LDH nanocages with high density of active sites, increased electrical conductivity, and enhanced intrinsic electroactivity. Specifically, the hollow h-CoFe-LDH NCs showed an excellent OER performance with a small overpotential of 278 mV to reach 50 mA cm^{-2}, while the yolk-shell ys-ZIF@CoFe-LDH NCs showed an outstanding electrocatalytic activity for the selective EG oxidation toward formate with a Faradaic efficiency (FE) up to 91%. In the EG-assisted water electrolysis system featuring the ys-ZIF@CoFe-LDH NCs nanocages and Pt/C (anode and cathode), a smaller cell voltage was required to achieve simultaneous H_2 production and EG-to-formate conversion, which significantly reduces energy input compared to conventional water electrolysis. This work provides a

new rational way to design advanced MOF-derived electrocatalysts for water oxidation or other oxidative reactions.

Second, a rational synthesis of composites with TM NPs, carbide nanocrystals, and porous NCNTs derived from MOF is reported. By trapping $[Fe(C_2O_4)_3]^{3-}$ units in the Zn/Mo-HZIF framework followed by pyrolysis, dual-phase MoC nanocrystals and Fe NPs confined in NCNTs (denoted as MoC-Fe@NCNTs) has been obtained, which exhibited remarkable electrocatalytic activity and stability for hydrogen and oxygen evolution. The MoC-Fe@NCNTs catalyst displayed fast kinetics and low overpotentials of 252 and 304 mV at 50 mA cm^{-2} for the HER and OER in 1.0 M KOH solution, respectively. DFT calculations and experimental observation indicate that Fe acts as an efficient water-dissociation promoter, while MoC has favorable hydrogen adsorption energy, leading to enhanced bifunctional activity. Moreover, NCNTs can facilitate charge transfer and protect the nanocrystals from aggregation and corrosion during the electrolysis. The strategy for controlled design and fabrication of MOF-derived heterostructures offers insights on developing electrocatalysts for highly efficient water splitting.

Third, MOF-derived dual-metal SACs, where Fe SA and Se SA are atomically dispersed on an N-doped carbon matrix, were also prepared. Se SA, as a promoter atom, contributes to the activity and selectivity of CO_2RR by affecting the central electronic structure of Fe and the interaction between intermediates and catalysts. FeSe-NC displayed an excellent CO_2RR performance affording an industrial-level j_{CO} (>235.0 mA cm^{-2}) and high FE_{CO} (>95 %). Using FeSe-NC as the cathode in a rechargeable Zn-CO_2 battery, competitive performance was realized with a peak power density of 2.01 mW cm^{-2} at the output voltage of 0.27 V. This work provides an effective atomic engineering strategy to improve the durability and activity of Fe-SACs in CO_2RR.

7.2. Outlooks

Despite these achievements in this thesis, great efforts are still needed to improve the understanding of the processes involving water electrolysis, selective small organic molecules oxidation, and carbon dioxide reduction. Below are some key tasks for further research on these topics.

Optimized design and synthesis. The design of highly active MOF derivatives as electrocatalysts requires innovative strategies to increase the exposure of the active sites, and improve intrinsic properties such as activity and conductivity, as well as stability. For SACs synthesis, the current conventional synthesis involves pyrolysis at high temperatures, which leads to inevitable agglomeration and uncontrollable coordination. These issues impact the catalytic performance of these MOF-derived SACs. Therefore, the development of "all-in-one" strategies for synthesizing MOF-derived catalysts with well-designed structures, compositions, and intrinsically enhanced activity is highly desired.

Development of advanced techniques. The microenvironment of MOF-derived catalysts, especially the SACs, plays an important role in electrocatalysis. To get an accurate view of their coordination structure, it is necessary to use advanced characterization techniques (e.g., XAS, atomic resolution TEM), which will help with the exploration of the reaction mechanism. However, these characterization techniques are expensive and very time consuming, and still under development. Besides, detailed *in-situ* analyses (e.g., IR, XPS, Raman, etc.) are needed to monitor the evolution of the active sites and detect the reaction intermediates, thus revealing the mechanism. Furthermore, theoretical calculation should be resorted to help with understanding.

Hence, elaborate design and synthesis of MOF-derived electrocatalysts with an optimal geometric and electronic structure, assisted with advanced *in-situ*/operando

characterization techniques and computational methods should be employed in developing MOF-derivatives used in electrocatalytic energy conversion fields.

References

[1] Z.W. Seh, J. Kibsgaard, C.F. Dickens, I. Chorkendorff, J.K. Nørskov, T.F. Jaramillo, Combining theory and experiment in electrocatalysis: Insights into materials design, Science, 355 (2017) eaad4998.

[2] J. Wu, H. Yang, Platinum-based oxygen reduction electrocatalysts, Accounts of chemical research, 46 (2013) 1848-1857.

[3] L. Zhang, G.-F. Chen, L.-X. Ding, H. Wang, Advanced Non-metallic Catalysts for Electrochemical Nitrogen Reduction under Ambient Conditions, Chemistry–A European Journal, (2019).

[4] C. Wang, L. Jin, H. Shang, H. Xu, Y. Shiraishi, Y. Du, Advances in engineering RuO_2 electrocatalysts towards oxygen evolution reaction, Chinese Chemical Letters, 32 (2021) 2108-2116.

[5] J.A. Trindell, J. Clausmeyer, R.M. Crooks, Size stability and H_2/CO selectivity for Au nanoparticles during electrocatalytic CO_2 reduction, Journal of the American Chemical Society, 139 (2017) 16161-16167.

[6] Y.-Z. Chen, R. Zhang, L. Jiao, H.-L. Jiang, Metal–organic framework-derived porous materials for catalysis, Coordination Chemistry Reviews, 362 (2018) 1-23.

[7] J.A. Turner, Sustainable hydrogen production, Science, 305 (2004) 972-974.

[8] G. Wang, J. Chen, Y. Ding, P. Cai, L. Yi, Y. Li, C. Tu, Y. Hou, Z. Wen, L. Dai, Electrocatalysis for CO_2 conversion: from fundamentals to value-added products, Chemical Society Reviews, 50 (2021) 4993-5061.

[9] S.Y. Tee, K.Y. Win, W.S. Teo, L.-D. Koh, S. Liu, C.P. Teng, M.-Y. Han, Recent Progress in Energy-Driven Water Splitting, Advanced Science, 4 (2017) 1600337.

[10] F. Dai, W. Fan, J. Bi, P. Jiang, D. Liu, X. Zhang, H. Lin, C. Gong, R. Wang, L. Zhang, A lead–porphyrin metal–organic framework: gas adsorption properties and electrocatalytic activity for water oxidation, Dalton Transactions, 45 (2016) 61-65.

[11] C. Liu, J. Wang, J. Wan, Y. Cheng, R. Huang, C. Zhang, W. Hu, G. Wei, C. Yu, Amorphous Metal–Organic Framework-Dominated Nanocomposites with Both Compositional and Structural Heterogeneity for Oxygen Evolution, Angewandte Chemie International Edition, 132 (2020) 3659-3666.

[12] K. Ge, S. Sun, Y. Zhao, K. Yang, S. Wang, Z. Zhang, J. Cao, Y. Yang, Y. Zhang,

M. Pan, L. Zhu, Facile Synthesis of Two-Dimensional Iron/Cobalt Metal–Organic Framework for Efficient Oxygen Evolution Electrocatalysis, Angew. Chem. Int. Ed., 60 (2021) 12097-12102.
[13] S. Li, Y. Gao, N. Li, L. Ge, X. Bu, P. Feng, Transition metal-based bimetallic MOFs and MOF-derived catalysts for electrochemical oxygen evolution reaction, Energy & Environmental Science, 14 (2021) 1897-1927.
[14] W. Cheng, Z.-P. Wu, D. Luan, S.-Q. Zang, X.W. Lou, Synergetic Cobalt-Copper-Based Bimetal–Organic Framework Nanoboxes toward Efficient Electrochemical Oxygen Evolution, Angewandte Chemie International Edition, 60 (2021) 26397-26402.
[15] L. Zhuang, L. Ge, H. Liu, Z. Jiang, Y. Jia, Z. Li, D. Yang, R.K. Hocking, M. Li, L. Zhang, X. Wang, X. Yao, Z. Zhu, A Surfactant-Free and Scalable General Strategy for Synthesizing Ultrathin Two-Dimensional Metal–Organic Framework Nanosheets for the Oxygen Evolution Reaction, Angewandte Chemie International Edition, 58 (2019) 13565-13572.
[16] X. Wang, Z. Na, D. Yin, C. Wang, Y. Wu, G. Huang, L. Wang, Phytic acid-assisted formation of hierarchical porous CoP/C nanoboxes for enhanced lithium storage and hydrogen generation, ACS Nano, 12 (2018) 12238-12246.
[17] S.A. Shah, Z. Ji, X. Shen, X. Yue, G. Zhu, K. Xu, A. Yuan, N. Ullah, J. Zhu, P. Song, X. Li, Thermal Synthesis of FeNi@Nitrogen-Doped Graphene Dispersed on Nitrogen-Doped Carbon Matrix as an Excellent Electrocatalyst for Oxygen Evolution Reaction, ACS Applied Energy Materials, 2 (2019) 4075-4083.
[18] C.-C. Hou, L. Zou, Q. Xu, A hydrangea-like superstructure of open carbon cages with hierarchical porosity and highly active metal sites, Adv. Mater., 31 (2019) 1904689.
[19] S. Liu, Z. Wang, S. Zhou, F. Yu, M. Yu, C.-Y. Chiang, W. Zhou, J. Zhao, J. Qiu, Metal–Organic-Framework-Derived Hybrid Carbon Nanocages as a Bifunctional Electrocatalyst for Oxygen Reduction and Evolution, Adv. Mater., 29 (2017) 1700874.
[20] K. Zhang, C. Qu, Z. Liang, S. Gao, H. Zhang, B. Zhu, W. Meng, E. Fu, R. Zou, Highly Dispersed Co–B/N Codoped Carbon Nanospheres on Graphene for Synergistic Effects as Bifunctional Oxygen Electrocatalysts, ACS Appl. Mater. Interfaces, 10 (2018) 30460-30469.
[21] Z. Pei, X.F. Lu, H. Zhang, Y. Li, D. Luan, X.W. Lou, Highly Efficient Electrocatalytic Oxygen Evolution Over Atomically Dispersed Synergistic Ni/Co Dual Sites, Angewandte Chemie International Edition, 61 (2022) e202207537.
[22] X. Han, X. Ling, D. Yu, D. Xie, L. Li, S. Peng, C. Zhong, N. Zhao, Y. Deng, W. Hu,

Atomically Dispersed Binary Co-Ni Sites in Nitrogen-Doped Hollow Carbon Nanocubes for Reversible Oxygen Reduction and Evolution, Advanced Materials, 31 (2019) 1905622.
[23] H. Hu, B. Guan, B. Xia, X.W. Lou, Designed Formation of Co3O4/NiCo2O4 Double-Shelled Nanocages with Enhanced Pseudocapacitive and Electrocatalytic Properties, J. Am. Chem. Soc., 137 (2015) 5590-5595.
[24] Y. Huang, S.L. Zhang, X.F. Lu, Z.-P. Wu, D. Luan, X.W. Lou, Trimetallic spinel $NiCo_{2-x}Fe_xO_4$ nanoboxes for highly efficient electrocatalytic oxygen evolution, Angew. Chem. Int. Ed., 60 (2021) 11841-11846.
[25] Z. Jiang, Z. Li, Z. Qin, H. Sun, X. Jiao, D. Chen, LDH nanocages synthesized with MOF templates and their high performance as supercapacitors, Nanoscale, 5 (2013) 11770-11775.
[26] G. Yilmaz, K.M. Yam, C. Zhang, H.J. Fan, G.W. Ho, In Situ Transformation of MOFs into Layered Double Hydroxide Embedded Metal Sulfides for Improved Electrocatalytic and Supercapacitive Performance, Adv. Mater., 29 (2017) 1606814.
[27] P. He, X.-Y. Yu, X.W. Lou, Carbon-Incorporated Nickel–Cobalt Mixed Metal Phosphide Nanoboxes with Enhanced Electrocatalytic Activity for Oxygen Evolution, Angew. Chem. Int. Ed., 56 (2017) 3897-3900.
[28] J. Lai, B. Huang, Y. Chao, X. Chen, S. Guo, Strongly Coupled Nickel–Cobalt Nitrides/Carbon Hybrid Nanocages with Pt-Like Activity for Hydrogen Evolution Catalysis, Adv. Mater., 31 (2019) 1805541.
[29] R. Shi, J. Wang, Z. Wang, T. Li, Y.-F. Song, Unique NiFeNiCoO2 hollow polyhedron as bifunctional electrocatalysts for water splitting, J. Energy Chem., 33 (2019) 74-80.
[30] H. Zhang, W. Zhou, J. Dong, X.F. Lu, X.W. Lou, Intramolecular electronic coupling in porous iron cobalt (oxy)phosphide nanoboxes enhances the electrocatalytic activity for oxygen evolution, Energy Environ. Sci., 12 (2019) 3348-3355.
[31] Y. Fu, W. Wang, J. Wang, X. Li, R. Shi, O. Peng, B.N. Chandrashekar, K. Liu, A. Amini, C. Cheng, MOFs-derived ZnCo–Fe core–shell nanocages with remarkable oxygen evolution reaction performance, J. Mater. Chem. A, 7 (2019) 17299-17305.
[32] L. Zhang, C. Lu, F. Ye, R. Pang, Y. Liu, Z. Wu, Z. Shao, Z. Sun, L. Hu, Selenic Acid Etching Assisted Vacancy Engineering for Designing Highly Active Electrocatalysts toward the Oxygen Evolution Reaction, Adv. Mater., 33 (2021) 2007523.
[33] X. Zhang, F. Yan, X.Z. Ma, C.L. Zhu, Y. Wang, Y. Xie, S.L. Chou, Y.J. Huang, Y.J.

Chen, Regulation of Morphology and Electronic Structure of FeCoNi Layered Double Hydroxides for Highly Active and Stable Water Oxidization Catalysts, Adv. Energy Mater., 11 (2021) 2102141.
[34] J. Zhang, L. Yu, Y. Chen, X.F. Lu, S. Gao, X.W. Lou, Designed formation of double-shelled Ni–Fe layered-double-hydroxide nanocages for efficient oxygen evolution reaction, Adv. Mater., 32 (2020) 1906432.
[35] L. Yu, J.F. Yang, B.Y. Guan, Y. Lu, X.W. Lou, Hierarchical Hollow Nanoprisms Based on Ultrathin Ni-Fe Layered Double Hydroxide Nanosheets with Enhanced Electrocatalytic Activity towards Oxygen Evolution, Angew. Chem. Int. Ed., 57 (2018) 172-176.
[36] Y. Qin, B. Wang, Y. Qiu, X. Liu, G. Qi, S. Zhang, A. Han, J. Luo, J. Liu, Multi-shelled hollow layered double hydroxides with enhanced performance for the oxygen evolution reaction, Chem. Commun., 57 (2021) 2752-2755.
[37] Z.-F. Huang, J. Song, Y. Du, S. Xi, S. Dou, J.M.V. Nsanzimana, C. Wang, Z.J. Xu, X. Wang, Chemical and structural origin of lattice oxygen oxidation in Co–Zn oxyhydroxide oxygen evolution electrocatalysts, Nat. Energy, 4 (2019) 329-338.
[38] N. Clament Sagaya Selvam, S.J. Kwak, G.H. Choi, M.J. Oh, H. Kim, W.-S. Yoon, W.B. Lee, P.J. Yoo, Unveiling the Impact of Fe Incorporation on Intrinsic Performance of Reconstructed Water Oxidation Electrocatalyst, ACS Energy Lett., (2021) 4345-4354.
[39] S.L. Zhang, B.Y. Guan, X.F. Lu, S. Xi, Y. Du, X.W. Lou, Metal Atom-Doped Co_3O_4 Hierarchical Nanoplates for Electrocatalytic Oxygen Evolution, Adv. Mater., 32 (2020) 2002235.
[40] Y. Hu, G. Luo, L. Wang, X. Liu, Y. Qu, Y. Zhou, F. Zhou, Z. Li, Y. Li, T. Yao, Single Ru Atoms Stabilized by Hybrid Amorphous/Crystalline FeCoNi Layered Double Hydroxide for Ultraefficient Oxygen Evolution, Adv. Energy Mater., 11 (2021) 2002816.
[41] D. Yan, C. Xia, W. Zhang, Q. Hu, C. He, B.Y. Xia, S. Wang, Cation Defect Engineering of Transition Metal Electrocatalysts for Oxygen Evolution Reaction, Advanced Energy Materials, 12 (2022) 2202317.
[42] W. Wang, H. Yan, U. Anand, U. Mirsaidov, Visualizing the conversion of metal–organic framework nanoparticles into hollow layered double hydroxide nanocages, J. Am. Chem. Soc., 143 (2021) 1854-1862.
[43] W. Sheng, H.A. Gasteiger, Y. Shao-Horn, Hydrogen oxidation and evolution reaction kinetics on platinum: acid vs alkaline electrolytes, Journal of The Electrochemical Society, 157 (2010) B1529.

[44] J. Durst, A. Siebel, C. Simon, F. Hasché, J. Herranz, H. Gasteiger, New insights into the electrochemical hydrogen oxidation and evolution reaction mechanism, Energy & Environmental Science, 7 (2014) 2255-2260.
[45] N. Danilovic, R. Subbaraman, D. Strmcnik, V. Stamenkovic, N. Markovic, Electrocatalysis of the HER in acid and alkaline media, Journal of the Serbian Chemical Society, 78 (2013).
[46] L. Yan, Y. Xu, P. Chen, S. Zhang, H. Jiang, L. Yang, Y. Wang, L. Zhang, J. Shen, X. Zhao, L. Wang, A Freestanding 3D Heterostructure Film Stitched by MOF-Derived Carbon Nanotube Microsphere Superstructure and Reduced Graphene Oxide Sheets: A Superior Multifunctional Electrode for Overall Water Splitting and Zn–Air Batteries, Adv. Mater., 32 (2020) 2003313.
[47] R. Wang, X.Y. Dong, J. Du, J.Y. Zhao, S.Q. Zang, MOF-Derived bifunctional Cu_3P nanoparticles coated by a N, P-codoped carbon shell for hydrogen evolution and oxygen reduction, Adv. Mater., 30 (2018) 1703711.
[48] Z.-H. Wang, X.-F. Wang, Z. Tan, X.-Z. Song, POM/MOF Hybrids and Their Derivatives for Hydrogen and Oxygen Evolution Electrocatalysis, Mater. Today Energy, (2020) 100618.
[49] H.B. Wu, B.Y. Xia, L. Yu, X.-Y. Yu, X.W.D. Lou, Porous molybdenum carbide nano-octahedrons synthesized via confined carburization in metal-organic frameworks for efficient hydrogen production, Nat. Commun., 6 (2015) 6512.
[50] Y. Zhu, G. Chen, X. Xu, G. Yang, M. Liu, Z. Shao, Enhancing electrocatalytic activity for hydrogen evolution by strongly coupled molybdenum nitride@ nitrogen-doped carbon porous nano-octahedrons, ACS Catalysis, 7 (2017) 3540-3547.
[51] J.-S. Li, S. Zhang, J.-Q. Sha, H. Wang, M.-Z. Liu, L.-X. Kong, G.-D. Liu, Confined molybdenum phosphide in P-doped porous carbon as efficient electrocatalysts for hydrogen evolution, ACS applied materials & interfaces, 10 (2018) 17140-17146.
[52] X.F. Lu, L. Yu, J. Zhang, X.W. Lou, Ultrafine Dual-Phased Carbide Nanocrystals Confined in Porous Nitrogen-Doped Carbon Dodecahedrons for Efficient Hydrogen Evolution Reaction, Adv. Mater., 31 (2019) 1900699.
[53] G. Yang, Y. Jiao, H. Yan, Y. Xie, A. Wu, X. Dong, D. Guo, C. Tian, H. Fu, Interfacial Engineering of MoO_2-FeP Heterojunction for Highly Efficient Hydrogen Evolution Coupled with Biomass Electrooxidation, Adv. Mater., 32 (2020) 2000455.
[54] T. Wang, P. Wang, W. Zang, X. Li, D. Chen, Z. Kou, S. Mu, J. Wang, Nanoframes of Co_3O_4–Mo_2N Heterointerfaces Enable High-Performance Bifunctionality toward Both

Electrocatalytic HER and OER, Adv. Funct. Mater., n/a (2021) 2107382.
[55] P. Zhang, Y. Liu, T. Liang, E.H. Ang, X. Zhang, F. Ma, Z. Dai, Nitrogen-doped carbon wrapped Co-Mo_2C dual Mott–Schottky nanosheets with large porosity for efficient water electrolysis, Appl. Catal., B, 284 (2021) 119738.
[56] Y. Pan, K. Sun, S. Liu, X. Cao, K. Wu, W.-C. Cheong, Z. Chen, Y. Wang, Y. Li, Y. Liu, Core–shell ZIF-8@ ZIF-67-derived CoP nanoparticle-embedded N-doped carbon nanotube hollow polyhedron for efficient overall water splitting, Journal of the American Chemical Society, 140 (2018) 2610-2618.
[57] W. Li, J. Liu, P. Guo, H. Li, B. Fei, Y. Guo, H. Pan, D. Sun, F. Fang, R. Wu, Co/CoP heterojunction on hierarchically ordered porous carbon as a highly efficient electrocatalyst for hydrogen and oxygen evolution, Advanced Energy Materials, 11 (2021) 2102134.
[58] N. Wang, X. Li, M.-K. Hu, W. Wei, S.-H. Zhou, X.-T. Wu, Q.-L. Zhu, Ordered macroporous superstructure of bifunctional cobalt phosphide with heteroatomic modification for paired hydrogen production and polyethylene terephthalate plastic recycling, Appl. Catal., B, 316 (2022) 121667.
[59] L. Yan, L. Cao, P. Dai, X. Gu, D. Liu, L. Li, Y. Wang, X. Zhao, Metal-organic frameworks derived nanotube of nickel–cobalt bimetal phosphides as highly efficient electrocatalysts for overall water splitting, Advanced Functional Materials, 27 (2017) 1703455.
[60] D. Li, Z. Zong, Z. Tang, Z. Liu, S. Chen, Y. Tian, X. Wang, Total water splitting catalyzed by Co@Ir core–shell nanoparticles encapsulated in nitrogen-doped porous carbon derived from metal–organic frameworks, ACS Sustainable Chemistry & Engineering, 6 (2018) 5105-5114.
[61] M.R. Singh, Y. Kwon, Y. Lum, J.W. Ager, III, A.T. Bell, Hydrolysis of Electrolyte Cations Enhances the Electrochemical Reduction of CO_2 over Ag and Cu, Journal of the American Chemical Society, 138 (2016) 13006-13012.
[62] Y. Hori, Electrochemical CO_2 Reduction on Metal Electrodes, in: C.G. Vayenas, R.E. White, M.E. Gamboa-Aldeco (Eds.) Modern Aspects of Electrochemistry, Springer New York, New York, NY, 2008, pp. 89-189.
[63] M.R. Singh, E.L. Clark, A.T. Bell, Effects of electrolyte, catalyst, and membrane composition and operating conditions on the performance of solar-driven electrochemical reduction of carbon dioxide, Physical Chemistry Chemical Physics, 17 (2015) 18924-18936.

[64] C.-T. Dinh, T. Burdyny, M.G. Kibria, A. Seifitokaldani, C.M. Gabardo, F.P. García de Arquer, A. Kiani, J.P. Edwards, P. De Luna, O.S. Bushuyev, C. Zou, R. Quintero-Bermudez, Y. Pang, D. Sinton, E.H. Sargent, CO_2 electroreduction to ethylene via hydroxide-mediated copper catalysis at an abrupt interface, Science, 360 (2018) 783-787.
[65] M.B. Ross, P. De Luna, Y. Li, C.-T. Dinh, D. Kim, P. Yang, E.H. Sargent, Designing materials for electrochemical carbon dioxide recycling, Nature Catalysis, 2 (2019) 648-658.
[66] S. Liu, H. Tao, L. Zeng, Q. Liu, Z. Xu, Q. Liu, J.-L. Luo, Shape-dependent electrocatalytic reduction of CO_2 to CO on triangular silver nanoplates, Journal of the American chemical society, 139 (2017) 2160-2163.
[67] W. Zhu, L. Zhang, P. Yang, C. Hu, Z. Luo, X. Chang, Z.J. Zhao, J. Gong, Low-coordinated edge sites on ultrathin palladium nanosheets boost carbon dioxide electroreduction performance, Angewandte Chemie International Edition, 57 (2018) 11544-11548.
[68] W. Zhu, Y.-J. Zhang, H. Zhang, H. Lv, Q. Li, R. Michalsky, A.A. Peterson, S. Sun, Active and selective conversion of CO_2 to CO on ultrathin Au nanowires, Journal of the American Chemical Society, 136 (2014) 16132-16135.
[69] S. Meshitsuka, M. Ichikawa, K. Tamaru, Electrocatalysis by metal phthalocyanines in the reduction of carbon dioxide, Journal of the Chemical Society, Chemical Communications, (1974) 158-159.
[70] D.-D. Ma, S.-G. Han, C. Cao, W. Wei, X. Li, B. Chen, X.-T. Wu, Q.-L. Zhu, Bifunctional single-molecular heterojunction enables completely selective CO_2-to-CO conversion integrated with oxidative 3D nano-polymerization, Energy & Environmental Science, 14 (2021) 1544-1552.
[71] S. Ren, D. Joulié, D. Salvatore, K. Torbensen, M. Wang, M. Robert, C.P. Berlinguette, Molecular electrocatalysts can mediate fast, selective CO_2 reduction in a flow cell, Science, 365 (2019) 367-369.
[72] Y. Chen, S. Ji, C. Chen, Q. Peng, D. Wang, Y. Li, Single-Atom Catalysts: Synthetic Strategies and Electrochemical Applications, Joule, 2 (2018) 1242-1264.
[73] H. Shang, T. Wang, J. Pei, Z. Jiang, D. Zhou, Y. Wang, H. Li, J. Dong, Z. Zhuang, W. Chen, D. Wang, J. Zhang, Y. Li, Design of a Single-Atom Indium$^{\delta+}$–N_4 Interface for Efficient Electroreduction of CO_2 to Formate, Angewandte Chemie International Edition, 59 (2020) 22465-22469.
[74] K. Sun, K. Yu, J. Fang, Z. Zhuang, X. Tan, Y. Wu, L. Zeng, Z. Zhuang, Y. Pan, C.

Chen, Nature-Inspired Design of Molybdenum-Selenium Dual-Single-Atom Electrocatalysts for CO_2 Reduction, Advanced Materials, 34 (2022) e2206478.
[75] C. Zhao, X. Dai, T. Yao, W. Chen, X. Wang, J. Wang, J. Yang, S. Wei, Y. Wu, Y. Li, Ionic Exchange of Metal–Organic Frameworks to Access Single Nickel Sites for Efficient Electroreduction of CO2, J. Am. Chem. Soc., 139 (2017) 8078-8081.
[76] F. Pan, H. Zhang, K. Liu, D. Cullen, K. More, M. Wang, Z. Feng, G. Wang, G. Wu, Y. Li, Unveiling active sites of CO_2 reduction on nitrogen-coordinated and atomically dispersed iron and cobalt catalysts, Acs Catalysis, 8 (2018) 3116-3122.
[77] C. Yan, H. Li, Y. Ye, H. Wu, F. Cai, R. Si, J. Xiao, S. Miao, S. Xie, F. Yang, Coordinatively unsaturated nickel–nitrogen sites towards selective and high-rate CO_2 electroreduction, Energy & Environmental Science, 11 (2018) 1204-1210.
[78] X. Wang, N. Fu, J.-C. Liu, K. Yu, Z. Li, Z. Xu, X. Liang, P. Zhu, C. Ye, A. Zhou, A. Li, L. Zheng, L.-M. Liu, C. Chen, D. Wang, Q. Peng, Y. Li, Atomic Replacement of PtNi Nanoalloys within Zn-ZIF-8 for the Fabrication of a Multisite CO_2 Reduction Electrocatalyst, Journal of the American Chemical Society, 144 (2022) 23223-23229.
[79] Y. Zhang, L. Jiao, W. Yang, C. Xie, H.-L. Jiang, Rational Fabrication of Low-Coordinate Single-Atom Ni Electrocatalysts by MOFs for Highly Selective CO_2 Reduction, Angew. Chem. Int. Ed., 60 (2021) 7607-7611.
[80] Q. Yang, C.C. Yang, C.H. Lin, H.L. Jiang, Metal–organic-framework-derived hollow N-doped porous carbon with ultrahigh concentrations of single Zn atoms for efficient carbon dioxide conversion, Angewandte Chemie, 131 (2019) 3549-3553.
[81] Q. Wang, T. Ina, W.-T. Chen, L. Shang, F. Sun, S. Wei, D. Sun-Waterhouse, S.G. Telfer, T. Zhang, G.I. Waterhouse, Evolution of Zn (II) single atom catalyst sites during the pyrolysis-induced transformation of ZIF-8 to N-doped carbons, Science Bulletin, 65 (2020) 1743-1751.
[82] S. Chen, X. Li, C.W. Kao, T. Luo, K. Chen, J. Fu, C. Ma, H. Li, M. Li, T.S. Chan, M. Liu, Unveiling the Proton-Feeding Effect in Sulfur-Doped Fe-N-C Single-Atom Catalyst for Enhanced CO_2 Electroreduction, Angewandte Chemie International Edition, 61 (2022) e202206233.
[83] X. Sun, Y. Tuo, C. Ye, C. Chen, Q. Lu, G. Li, P. Jiang, S. Chen, P. Zhu, M. Ma, Phosphorus induced electron localization of single iron sites for boosted CO_2 electroreduction reaction, Angewandte Chemie, 133 (2021) 23806-23810.
[84] S. Liu, M. Jin, J. Sun, Y. Qin, S. Gao, Y. Chen, S. Zhang, J. Luo, X. Liu, Coordination environment engineering to boost electrocatalytic CO_2 reduction

performance by introducing boron into single-Fe-atomic catalyst, Chemical Engineering Journal, 437 (2022) 135294.
[85] Y. Li, W. Shan, M.J. Zachman, M. Wang, S. Hwang, H. Tabassum, J. Yang, X. Yang, S. Karakalos, Z. Feng, G. Wang, G. Wu, Atomically Dispersed Dual-Metal Site Catalysts for Enhanced CO_2 Reduction: Mechanistic Insight into Active Site Structures, Angewandte Chemie International Edition, 61 (2022) e202205632.
[86] H. Cheng, X. Wu, M. Feng, X. Li, G. Lei, Z. Fan, D. Pan, F. Cui, G. He, Atomically Dispersed Ni/Cu Dual Sites for Boosting the CO_2 Reduction Reaction, ACS Catalysis, 11 (2021) 12673-12681.
[87] Y. Gao, B. Liu, D. Wang, Microenvironment Engineering of Single/Dual-atom Catalysts for Electrocatalytic Application, Advanced Materials, n/a (2023) 2209654.
[88] Q. Hao, H.-x. Zhong, J.-z. Wang, K.-h. Liu, J.-m. Yan, Z.-h. Ren, N. Zhou, X. Zhao, H. Zhang, D.-x. Liu, Nickel dual-atom sites for electrochemical carbon dioxide reduction, Nature Synthesis, 1 (2022) 719-728.
[89] J. Hou, Z. Fan, R. Luo, Y. Zhang, B. Zhang, P. Zhai, Y. Zhang, C. Wang, J. Gao, W. Zhou, L. Sun, Oxygen-Bridged Indium-Nickel Atomic Pair as Dual-Metal Active Sites Enabling Synergistic Electrocatalytic CO_2 Reduction, Angewandte Chemie International Edition, n/a (2023) e202216326.
[90] G. Kresse, J. Furthmüller, Efficient iterative schemes for ab initio total-energy calculations using a plane-wave basis set, Physical review B, 54 (1996) 11169.
[91] G. Kresse, J. Furthmüller, Efficiency of ab-initio total energy calculations for metals and semiconductors using a plane-wave basis set, Computational materials science, 6 (1996) 15-50.
[92] P.E. Blöchl, Projector augmented-wave method, Physical Review B, 50 (1994) 17953-17979.
[93] J.P. Perdew, K. Burke, M. Ernzerhof, Generalized gradient approximation made simple, Physical review letters, 77 (1996) 3865.
[94] Y.P. Zhu, C. Guo, Y. Zheng, S.-Z. Qiao, Surface and interface engineering of noble-metal-free electrocatalysts for efficient energy conversion processes, Acc. Chem. Res., 50 (2017) 915-923.
[95] G. Prieto, H. Tüysüz, N. Duyckaerts, J. Knossalla, G.-H. Wang, F. Schüth, Hollow nano-and microstructures as catalysts, Chem. Rev., 116 (2016) 14056-14119.
[96] X. Wang, J. Feng, Y. Bai, Q. Zhang, Y. Yin, Synthesis, properties, and applications of hollow micro-/nanostructures, Chem. Rev., 116 (2016) 10983-11060.

[97] Z.-X. Cai, Z.-L. Wang, Y.-J. Xia, H. Lim, W. Zhou, A. Taniguchi, M. Ohtani, K. Kobiro, T. Fujita, Y. Yamauchi, Tailored catalytic nanoframes from metal–organic frameworks by anisotropic surface modification and etching for the hydrogen evolution reaction, Angew. Chem. Int. Ed., 60 (2021) 4747-4755.
[98] J. Nai, Y. Tian, X. Guan, L. Guo, Pearson's principle inspired generalized strategy for the fabrication of metal hydroxide and oxide nanocages, J. Am. Chem. Soc., 135 (2013) 16082-16091.
[99] Y. Liu, J. Goebl, Y. Yin, Templated synthesis of nanostructured materials, Chem. Soc. Rev., 42 (2013) 2610-2653.
[100] J. Nai, J. Zhang, X.W. Lou, Construction of single-crystalline prussian blue analog hollow nanostructures with tailorable topologies, Chem, 4 (2018) 1967-1982.
[101] Z. Li, M. Song, W. Zhu, W. Zhuang, X. Du, L. Tian, MOF-derived hollow heterostructures for advanced electrocatalysis, Coord. Chem. Rev., 439 (2021) 213946.
[102] L. Feng, K.-Y. Wang, G.S. Day, M.R. Ryder, H.-C. Zhou, Destruction of metal–organic frameworks: Positive and negative aspects of stability and lability, Chem. Rev., 120 (2020) 13087-13133.
[103] X. Li, Q.-L. Zhu, MOF-based materials for photo-and electrocatalytic CO_2 reduction, EnergyChem, 2 (2020) 100033.
[104] Y.-C. Zhang, C. Han, J. Gao, L. Pan, J. Wu, X.-D. Zhu, J.-J. Zou, NiCo-based electrocatalysts for the alkaline oxygen evolution reaction: a review, ACS Catal., 11 (2021) 12485-12509.
[105] J. Wang, W. Cui, Q. Liu, Z. Xing, A.M. Asiri, X. Sun, Recent progress in cobalt-based heterogeneous catalysts for electrochemical water splitting, Adv. Mater., 28 (2016) 215-230.
[106] F. Dionigi, Z. Zeng, I. Sinev, T. Merzdorf, S. Deshpande, M.B. Lopez, S. Kunze, I. Zegkinoglou, H. Sarodnik, D. Fan, A. Bergmann, J. Drnec, J.F.d. Araujo, M. Gliech, D. Teschner, J. Zhu, W.-X. Li, J. Greeley, B.R. Cuenya, P. Strasser, In-situ structure and catalytic mechanism of NiFe and CoFe layered double hydroxides during oxygen evolution, Nat. Commun., 11 (2020) 2522.
[107] Z.-F. Huang, J. Song, K. Li, M. Tahir, Y.-T. Wang, L. Pan, L. Wang, X. Zhang, J.-J. Zou, Hollow cobalt-based bimetallic sulfide polyhedra for efficient all-pH-value electrochemical and photocatalytic hydrogen evolution, J. Am. Chem. Soc., 138 (2016) 1359-1365.
[108] B. Qiu, L. Cai, Y. Wang, Z. Lin, Y. Zuo, M. Wang, Y. Chai, Fabrication of nickel–

cobalt bimetal phosphide nanocages for enhanced oxygen evolution catalysis, Adv. Funct. Mater., 28 (2018) 1706008.
[109] J. Shan, C. Ye, S. Chen, T. Sun, Y. Jiao, L. Liu, C. Zhu, L. Song, Y. Han, M. Jaroniec, Y. Zhu, Y. Zheng, S.-Z. Qiao, Short-range ordered iridium single atoms integrated into cobalt oxide spinel structure for highly efficient electrocatalytic water oxidation, J. Am. Chem. Soc., 143 (2021) 5201-5211.
[110] J. Song, C. Wei, Z.-F. Huang, C. Liu, L. Zeng, X. Wang, Z.J. Xu, A review on fundamentals for designing oxygen evolution electrocatalysts, Chemical Society Reviews, 49 (2020) 2196-2214.
[111] J.J. Tian, C.S. Cao, D.D. Ma, S.G. Han, Y.C. He, X.T. Wu, Q.L. Zhu, Killing two birds with one stone: selective oxidation of small organic molecule as anodic reaction to boost CO_2 Electrolysis, Small Struct., 3 (2022) 2100134.
[112] C. Cao, D.D. Ma, J. Jia, Q. Xu, X.T. Wu, Q.L. Zhu, Divergent paths, same goal: a pair-electrosynthesis tactic for cost-efficient and exclusive formate production by metal–organic-framework-derived 2D electrocatalysts, Adv. Mater., 33 (2021) 2008631.
[113] B. Zhu, Z. Liang, R. Zou, Designing advanced catalysts for energy conversion based on urea oxidation reaction, Small, 16 (2020) 1906133.
[114] J.N. Hausmann, P.V. Menezes, G. Vijaykumar, K. Laun, T. Diemant, I. Zebger, T. Jacob, M. Driess, P.W. Menezes, In-liquid plasma modified nickel foam: NiOOH/NiFeOOH active site multiplication for electrocatalytic alcohol, aldehyde, and water oxidation, Adv. Energy Mater., 12 (2022) 2202098.
[115] S.G. Han, M. Zhang, Z.H. Fu, L. Zheng, D.D. Ma, X.T. Wu, Q.L. Zhu, Enzyme-inspired microenvironment engineering of a single-molecular heterojunction for promoting concerted electrochemical CO_2 reduction, Adv. Mater., 34 (2022) 2202830.
[116] L. Jiao, W. Wei, X. Li, C.-B. Hong, S.-G. Han, M.I. Khan, Q.-L. Zhu, Value-added formate production from selective ethylene glycol oxidation based on cost-effective self-supported MOF nanosheet arrays, Rare Met., 41 (2022) 3654-3661.
[117] K. Xiang, D. Wu, X. Deng, M. Li, S. Chen, P. Hao, X. Guo, J.L. Luo, X.Z. Fu, Boosting H_2 generation coupled with selective oxidation of methanol into value-added chemical over cobalt hydroxide@hydroxysulfide nanosheets electrocatalysts, Adv. Funct. Mater., 30 (2020) 1909610.
[118] X. Long, J. Li, S. Xiao, K. Yan, Z. Wang, H. Chen, S. Yang, A strongly coupled graphene and FeNi double hydroxide hybrid as an excellent electrocatalyst for the oxygen evolution reaction, Angew. Chem. Int. Ed., 53 (2014) 7584-7588.

[119] L. Zhang, J. Liang, L. Yue, K. Dong, J. Li, D. Zhao, Z. Li, S. Sun, Y. Luo, Q. Liu, Benzoate anions-intercalated NiFe-layered double hydroxide nanosheet array with enhanced stability for electrochemical seawater oxidation, Nano Research Energy, 1 (2022) e9120028.

[120] L. Ren, P. Wang, Y. Han, C. Hu, B. Wei, Synthesis of $CoC_2O_4 \cdot 2H_2O$ nanorods and their thermal decomposition to Co_3O_4 nanoparticles, Chem. Phys. Lett., 476 (2009) 78-83.

[121] D.M. Mangiante, R.D. Schaller, P. Zarzycki, J.F. Banfield, B. Gilbert, Mechanism of ferric oxalate photolysis, ACS Earth Space Chem., 1 (2017) 270-276.

[122] C.-F. Li, J.-W. Zhao, L.-J. Xie, J.-Q. Wu, Q. Ren, Y. Wang, G.-R. Li, Surface-adsorbed carboxylate ligands on layered double hydroxides/metal–organic frameworks promote the electrocatalytic oxygen evolution reaction, Angew. Chem. Int. Ed., 60 (2021) 18129-18137.

[123] Z. Li, X. Zhang, Y. Kang, C.C. Yu, Y. Wen, M. Hu, D. Meng, W. Song, Y. Yang, Interface engineering of Co-LDH@MOF heterojunction in highly stable and efficient oxygen evolution reaction, Adv. Sci., 8 (2021) 2002631.

[124] S. Lee, L. Bai, X. Hu, Deciphering iron-dependent activity in oxygen evolution catalyzed by nickel–iron layered double hydroxide, Angew. Chem. Int. Ed., 59 (2020) 8072-8077.

[125] J. Xiao, S. Yang, Bio-inspired synthesis of NaCl-type $Co_xNi_{1-x}O$ ($0 \leq x < 1$) nanorods on reduced graphene oxide sheets and screening for asymmetric electrochemical capacitors, J. Mater. Chem., 22 (2012) 12253-12262.

[126] Z. Zhao, H. Wu, H. He, X. Xu, Y. Jin, A high-performance binary Ni–Co hydroxide-based water oxidation electrode with three-dimensional coaxial nanotube array structure, Adv. Funct. Mater., 24 (2014) 4698-4705.

[127] M.S. Burke, M.G. Kast, L. Trotochaud, A.M. Smith, S.W. Boettcher, Cobalt–iron (oxy) hydroxide oxygen evolution electrocatalysts: the role of structure and composition on activity, stability, and mechanism, J. Am. Chem. Soc., 137 (2015) 3638-3648.

[128] X. Cui, W. Guo, M. Zhou, Y. Yang, Y. Li, P. Xiao, Y. Zhang, X. Zhang, Promoting effect of Co in Ni_mCo_n (m+n=4) bimetallic electrocatalysts for methanol oxidation reaction, ACS Appl. Mater. Interfaces, 7 (2015) 493-503.

[129] J. Jia, L. Zhao, Y. Chang, M. Jia, Z. Wen, Understanding the growth of NiSe nanoparticles on reduced graphene oxide as efficient electrocatalysts for methanol oxidation reaction, Ceram. Int., 46 (2020) 10023-10028.

[130] A.A. Dubale, Y. Zheng, H. Wang, R. Hübner, Y. Li, J. Yang, J. Zhang, N.K. Sethi, L. He, Z. Zheng, W. Liu, High-Performance bismuth-doped nickel aerogel electrocatalyst for the methanol oxidation reaction, Angew. Chem. Int. Ed., 59 (2020) 13891-13899.
[131] X. Wang, L. Yu, B.Y. Guan, S. Song, X.W. Lou, Metal–Organic Framework Hybrid-Assisted Formation of Co_3O_4/Co-Fe Oxide Double-Shelled Nanoboxes for Enhanced Oxygen Evolution, Adv. Mater., 30 (2018) 1801211.
[132] Y. Lin, H. Wan, D. Wu, G. Chen, N. Zhang, X. Liu, J. Li, Y. Cao, G. Qiu, R. Ma, Metal–Organic Framework Hexagonal Nanoplates: Bottom-up Synthesis, Topotactic Transformation, and Efficient Oxygen Evolution Reaction, J. Am. Chem. Soc., 142 (2020) 7317-7321.
[133] W. Cheng, Z.P. Wu, D. Luan, S.Q. Zang, X.W.D. Lou, Synergetic Cobalt-Copper-Based Bimetal-Organic Framework Nanoboxes toward Efficient Electrochemical Oxygen Evolution, Angew. Chem. Int. Ed., 60 (2021) 26397-26402.
[134] C. Wang, W. Chen, D. Yuan, S. Qian, D. Cai, J. Jiang, S. Zhang, Tailoring the nanostructure and electronic configuration of metal phosphides for efficient electrocatalytic oxygen evolution reactions, Nano Energy, 69 (2020) 104453.
[135] J. Li, W. Huang, M. Wang, S. Xi, J. Meng, K. Zhao, J. Jin, W. Xu, Z. Wang, X. Liu, Q. Chen, L. Xu, X. Liao, Y. Jiang, K.A. Owusu, B. Jiang, C. Chen, D. Fan, L. Zhou, L. Mai, Low-Crystalline Bimetallic Metal–Organic Framework Electrocatalysts with Rich Active Sites for Oxygen Evolution, ACS Energy Lett., 4 (2019) 285-292.
[136] F. Lyu, Y. Bai, Z. Li, W. Xu, Q. Wang, J. Mao, L. Wang, X. Zhang, Y. Yin, Self-Templated Fabrication of CoO–MoO_2 Nanocages for Enhanced Oxygen Evolution, Adv. Funct. Mater., 27 (2017) 1702324.
[137] S. Wan, J. Qi, W. Zhang, W. Wang, S. Zhang, K. Liu, H. Zheng, J. Sun, S. Wang, R. Cao, Hierarchical Co(OH)F Superstructure Built by Low-Dimensional Substructures for Electrocatalytic Water Oxidation, Adv. Mater., 29 (2017) 1700286.
[138] Z. Zhang, X. Li, C. Zhong, N. Zhao, Y. Deng, X. Han, W. Hu, Spontaneous Synthesis of Silver-Nanoparticle-Decorated Transition-Metal Hydroxides for Enhanced Oxygen Evolution Reaction, Angew. Chem. Int. Ed., 59 (2020) 7245-7250.
[139] W. Li, J. Liu, P.F. Guo, H.Z. Li, B. Fei, Y.H. Guo, H.G. Pan, D.L. Sun, F. Fang, R.B. Wu, Co/CoP Heterojunction on Hierarchically Ordered Porous Carbon as a Highly Efficient Electrocatalyst for Hydrogen and Oxygen Evolution, Adv. Energy Mater., 11 (2021) 2102134.
[140] P. Li, M. Wang, X. Duan, L. Zheng, X. Cheng, Y. Zhang, Y. Kuang, Y. Li, Q. Ma,

Z. Feng, W. Liu, X. Sun, Boosting oxygen evolution of single-atomic ruthenium through electronic coupling with cobalt-iron layered double hydroxides, Nat. Commun., 10 (2019) 1711.
[141] L.J. Enman, M.B. Stevens, M.H. Dahan, M.R. Nellist, M.C. Toroker, S.W. Boettcher, Operando X-ray absorption spectroscopy shows iron oxidation is concurrent with oxygen evolution in cobalt–iron (oxy)hydroxide electrocatalysts, Angew. Chem. Int. Ed., 57 (2018) 12840-12844.
[142] F. Meng, C. Dai, Z. Liu, S. Luo, J. Ge, Y. Duan, G. Chen, C. Wei, R.R. Chen, J. Wang, Methanol electro-oxidation to formate on iron-substituted lanthanum cobaltite perovskite oxides, eScience, 2 (2022) 87-94.
[143] Y. Wu, Y. Yi, Z. Sun, H. Sun, T. Guo, M. Zhang, L. Cui, K. Jiang, Y. Peng, J. Sun, Bimetallic Fe-Ni phosphide carved nanoframes toward efficient overall water splitting and potassium-ion storage, Chem. Eng. J., 390 (2020) 124515.
[144] H. Liu, J. Guan, S. Yang, Y. Yu, R. Shao, Z. Zhang, M. Dou, F. Wang, Q. Xu, Metal–Organic-Framework-Derived Co_2P Nanoparticle/Multi-Doped Porous Carbon as a Trifunctional Electrocatalyst, Adv. Mater., 32 (2020) 2003649.
[145] L. Yan, B. Zhang, J. Zhu, Y. Li, P. Tsiakaras, P.K. Shen, Electronic modulation of cobalt phosphide nanosheet arrays via copper doping for highly efficient neutral-pH overall water splitting, Appl. Catal., B, 265 (2020) 118555.
[146] K. Xiang, D. Wu, X. Deng, M. Li, S. Chen, P. Hao, X. Guo, J.L. Luo, X.Z. Fu, Boosting H_2 generation coupled with selective oxidation of methanol into value-added chemical over cobalt hydroxide@ hydroxysulfide nanosheets electrocatalysts, Adv. Funct. Mater., 30 (2020) 1909610.
[147] M. Li, X. Deng, K. Xiang, Y. Liang, B. Zhao, J. Hao, J.L. Luo, X.Z. Fu, Value-Added Formate Production from Selective Methanol Oxidation as Anodic Reaction to Enhance Electrochemical Hydrogen Cogeneration, ChemSusChem, 13 (2020) 914-921.
[148] Z.-Y. Yu, C.-C. Lang, M.-R. Gao, Y. Chen, Q.-Q. Fu, Y. Duan, S.-H. Yu, Ni–Mo–O nanorod-derived composite catalysts for efficient alkaline water-to-hydrogen conversion via urea electrolysis, Energy Environ. Sci., 11 (2018) 1890-1897.
[149] C. Hu, L. Zhang, J. Gong, Recent progress made in the mechanism comprehension and design of electrocatalysts for alkaline water splitting, Energy & Environmental Science, 12 (2019) 2620-2645.
[150] Y. Jiao, Y. Zheng, M. Jaroniec, S.Z. Qiao, Design of electrocatalysts for oxygen- and hydrogen-involving energy conversion reactions, Chemical Society Reviews, 44

(2015) 2060-2086.
[151] M.K. Debe, Electrocatalyst approaches and challenges for automotive fuel cells, Nature, 486 (2012) 43-51.
[152] Q. Yang, H. Liu, P. Yuan, Y. Jia, L. Zhuang, H. Zhang, X. Yan, G. Liu, Y. Zhao, J. Liu, S. Wei, L. Song, Q. Wu, B. Ge, L. Zhang, K. Wang, X. Wang, C.-R. Chang, X. Yao, Single Carbon Vacancy Traps Atomic Platinum for Hydrogen Evolution Catalysis, Journal of the American Chemical Society, (2022).
[153] Q. Wang, Z. Zhang, C. Cai, M. Wang, Z.L. Zhao, M. Li, X. Huang, S. Han, H. Zhou, Z. Feng, L. Li, J. Li, H. Xu, J.S. Francisco, M. Gu, Single Iridium Atom Doped Ni_2P Catalyst for Optimal Oxygen Evolution, Journal of the American Chemical Society, 143 (2021) 13605-13615.
[154] Y.L. Wu, X. Li, Y.S. Wei, Z. Fu, W. Wei, X.T. Wu, Q.L. Zhu, Q. Xu, Ordered macroporous superstructure of nitrogen-doped nanoporous carbon implanted with ultrafine Ru nanoclusters for efficient pH-universal hydrogen evolution reaction, Advanced Materials, 33 (2021) 2006965.
[155] D.H. Kweon, M.S. Okyay, S.-J. Kim, J.-P. Jeon, H.-J. Noh, N. Park, J. Mahmood, J.-B. Baek, Ruthenium anchored on carbon nanotube electrocatalyst for hydrogen production with enhanced Faradaic efficiency, Nature communications, 11 (2020) 1-10.
[156] H. Ma, Z. Chen, Z. Wang, C.V. Singh, Q. Jiang, Interface Engineering of Co/CoMoN/NF Heterostructures for High-Performance Electrochemical Overall Water Splitting, Adv Sci (Weinh), 9 (2022) e2105313.
[157] Y. Guo, J. Tang, Z. Wang, Y.-M. Kang, Y. Bando, Y. Yamauchi, Elaborately assembled core-shell structured metal sulfides as a bifunctional catalyst for highly efficient electrochemical overall water splitting, Nano Energy, 47 (2018) 494-502.
[158] X. Yan, J. Biemolt, K. Zhao, Y. Zhao, X. Cao, Y. Yang, X. Wu, G. Rothenberg, N. Yan, A membrane-free flow electrolyzer operating at high current density using earth-abundant catalysts for water splitting, Nature Communications, 12 (2021) 1-9.
[159] H.H. Hwu, J.G. Chen, Surface Chemistry of Transition Metal Carbides, Chemical Reviews, 105 (2005) 185-212.
[160] S.T. Oyama, Preparation and catalytic properties of transition metal carbides and nitrides, Catalysis Today, 15 (1992) 179-200.
[161] X.F. Lu, L. Yu, J. Zhang, X.W. Lou, Ultrafine dual-phased carbide nanocrystals confined in porous nitrogen-doped carbon dodecahedrons for efficient hydrogen evolution reaction, Advanced Materials, 31 (2019) 1900699.

[162] H.B. Wu, B.Y. Xia, L. Yu, X.-Y. Yu, X.W.D. Lou, Porous molybdenum carbide nano-octahedrons synthesized via confined carburization in metal-organic frameworks for efficient hydrogen production, Nature communications, 6 (2015) 1-8.
[163] Y. Gu, A. Wu, Y. Jiao, H. Zheng, X. Wang, Y. Xie, L. Wang, C. Tian, H. Fu, Two-dimensional porous molybdenum phosphide/nitride heterojunction nanosheets for pH-universal hydrogen evolution reaction, Angewandte Chemie International Edition, 60 (2021) 6673-6681.
[164] Y. Luo, Z. Wang, Y. Fu, C. Jin, Q. Wei, R. Yang, In situ preparation of hollow Mo_2C–C hybrid microspheres as bifunctional electrocatalysts for oxygen reduction and evolution reactions, Journal of Materials Chemistry A, 4 (2016) 12583-12590.
[165] B. Geng, F. Yan, L. Liu, C. Zhu, B. Li, Y. Chen, Ni/MoC heteronanoparticles encapsulated within nitrogen-doped carbon nanotube arrays as highly efficient self-supported electrodes for overall water splitting, Chemical Engineering Journal, 406 (2021) 126815.
[166] L. Zhang, Y. Zhu, Z. Nie, Z. Li, Y. Ye, L. Li, J. Hong, Z. Bi, Y. Zhou, G. Hu, Co/MoC nanoparticles embedded in carbon nanoboxes as robust trifunctional electrocatalysts for a Zn–air battery and water electrocatalysis, ACS Nano, 15 (2021) 13399-13414.
[167] T. Ouyang, Y.Q. Ye, C.Y. Wu, K. Xiao, Z.Q. Liu, Heterostructures composed of N-doped carbon nanotubes encapsulating cobalt and β-Mo_2C nanoparticles as bifunctional electrodes for water splitting, Angewandte Chemie, 131 (2019) 4977-4982.
[168] Z. Zhuang, Y. Li, Z. Li, F. Lv, Z. Lang, K. Zhao, L. Zhou, L. Moskaleva, S. Guo, L. Mai, MoB/g-C_3N_4 interface materials as a schottky catalyst to boost hydrogen evolution, Angew. Chem., 130 (2018) 505-509.
[169] A. Wu, Y. Xie, H. Ma, C. Tian, Y. Gu, H. Yan, X. Zhang, G. Yang, H. Fu, Integrating the active OER and HER components as the heterostructures for the efficient overall water splitting, Nano Energy, 44 (2018) 353-363.
[170] D. Friebel, M.W. Louie, M. Bajdich, K.E. Sanwald, Y. Cai, A.M. Wise, M.-J. Cheng, D. Sokaras, T.-C. Weng, R. Alonso-Mori, Identification of highly active Fe sites in (Ni, Fe) OOH for electrocatalytic water splitting, Journal of the American Chemical Society, 137 (2015) 1305-1313.
[171] B. Singh, M.B. Gawande, A.D. Kute, R.S. Varma, P. Fornasiero, P. McNeice, R.V. Jagadeesh, M. Beller, R. Zbořil, Single-Atom (Iron-Based) Catalysts: Synthesis and Applications, Chemical Reviews, 121 (2021) 13620-13697.

[172] N. Clament Sagaya Selvam, S.J. Kwak, G.H. Choi, M.J. Oh, H. Kim, W.-S. Yoon, W.B. Lee, P.J. Yoo, Unveiling the impact of Fe incorporation on intrinsic performance of reconstructed water oxidation electrocatalyst, ACS Energy Letters, 6 (2021) 4345-4354.

[173] S. Anantharaj, S. Kundu, S. Noda, "The Fe Effect": A review unveiling the critical roles of Fe in enhancing OER activity of Ni and Co based catalysts, Nano Energy, 80 (2021) 105514.

[174] M. Li, Y. Zhu, H. Wang, C. Wang, N. Pinna, X. Lu, Ni strongly coupled with Mo_2C encapsulated in nitrogen-doped carbon nanofibers as robust bifunctional catalyst for overall water splitting, Advanced Energy Materials, 9 (2019) 1803185.

[175] G. Yang, Y. Jiao, H. Yan, Y. Xie, A. Wu, X. Dong, D. Guo, C. Tian, H. Fu, Interfacial engineering of MoO_2-FeP heterojunction for highly efficient hydrogen evolution coupled with biomass electrooxidation, Advanced Materials, 32 (2020) 2000455.

[176] T. Ouyang, A.-N. Chen, Z.-Z. He, Z.-Q. Liu, Y. Tong, Rational design of atomically dispersed nickel active sites in β-Mo_2C for the hydrogen evolution reaction at all pH values, Chemical communications, 54 (2018) 9901-9904.

[177] S. Liu, Z. Wang, S. Zhou, F. Yu, M. Yu, C.Y. Chiang, W. Zhou, J. Zhao, J. Qiu, Metal–organic-framework-derived hybrid carbon nanocages as a bifunctional electrocatalyst for oxygen reduction and evolution, Advanced Materials, 29 (2017) 1700874.

[178] J. Meng, C. Niu, L. Xu, J. Li, X. Liu, X. Wang, Y. Wu, X. Xu, W. Chen, Q. Li, Z. Zhu, D. Zhao, L. Mai, General Oriented Formation of Carbon Nanotubes from Metal–Organic Frameworks, J. Am. Chem. Soc., 139 (2017) 8212-8221.

[179] F. Wang, Z.S. Liu, H. Yang, Y.X. Tan, J. Zhang, Hybrid zeolitic imidazolate frameworks with catalytically active TO_4 building blocks, Angewandte Chemie, 123 (2011) 470-473.

[180] Y. Han, F. Wang, J. Zhang, Design and syntheses of hybrid zeolitic imidazolate frameworks, Coordination Chemistry Reviews, 471 (2022) 214759.

[181] C. Avci, J. Ariñez-Soriano, A. Carné-Sánchez, V. Guillerm, C. Carbonell, I. Imaz, D. Maspoch, Post-Synthetic Anisotropic Wet-Chemical Etching of Colloidal Sodalite ZIF Crystals, Angew. Chem. Int. Ed., 54 (2015) 14417-14421.

[182] B.Y. Xia, Y. Yan, N. Li, H.B. Wu, X.W.D. Lou, X. Wang, A metal–organic framework-derived bifunctional oxygen electrocatalyst, Nature energy, 1 (2016) 1-8.

[183] Z. Yan, G. He, P.K. Shen, Z. Luo, J. Xie, M. Chen, MoC–graphite composite as a Pt electrocatalyst support for highly active methanol oxidation and oxygen reduction reaction, Journal of Materials Chemistry A, 2 (2014) 4014-4022.
[184] K. Wang, S. Liu, J. Zhang, Z. Hu, Q. Kong, Y. Xu, X. Huang, A One-Stone-Two-Birds Strategy to Functionalized Carbon Nanocages, ACS Nano, (2022).
[185] C.C. Hou, L. Zou, Q. Xu, A hydrangea-like superstructure of open carbon cages with hierarchical porosity and highly active metal sites, Advanced Materials, 31 (2019) 1904689.
[186] T. Ouyang, Y.-Q. Ye, C.-Y. Wu, K. Xiao, Z.-Q. Liu, Heterostructures Composed of N-Doped Carbon Nanotubes Encapsulating Cobalt and β-Mo_2C Nanoparticles as Bifunctional Electrodes for Water Splitting, Angew. Chem. Int. Ed., 58 (2019) 4923-4928.
[187] M.A.R. Anjum, M.H. Lee, J.S. Lee, Boron-and nitrogen-codoped molybdenum carbide nanoparticles imbedded in a BCN network as a bifunctional electrocatalyst for hydrogen and oxygen evolution reactions, ACS Catal., 8 (2018) 8296-8305.
[188] M. Li, Y. Zhu, H. Wang, C. Wang, N. Pinna, X. Lu, Ni Strongly Coupled with Mo_2C Encapsulated in Nitrogen-Doped Carbon Nanofibers as Robust Bifunctional Catalyst for Overall Water Splitting, Adv. Energy Mater., 9 (2019) 1803185.
[189] J. Jiang, Q. Liu, C. Zeng, L. Ai, Cobalt/molybdenum carbide@N-doped carbon as a bifunctional electrocatalyst for hydrogen and oxygen evolution reactions, J. Mater. Chem. A, 5 (2017) 16929-16935.
[190] C. Chen, A. Wu, H. Yan, Y. Xiao, C. Tian, H. Fu, Trapping $[PMo_{12}O_{40}]^{3-}$ clusters into pre-synthesized ZIF-67 toward MoxCoxC particles confined in uniform carbon polyhedrons for efficient overall water splitting, Chem. Sci., 9 (2018) 4746-4755.
[191] X. Li, X. Wang, J. Zhou, L. Han, C. Sun, Q. Wang, Z. Su, Ternary hybrids as efficient bifunctional electrocatalysts derived from bimetallic metal–organic-frameworks for overall water splitting, J. Mater. Chem. A, 6 (2018) 5789-5796.
[192] Q. Hu, X. Liu, B. Zhu, L. Fan, X. Chai, Q. Zhang, J. Liu, C. He, Z. Lin, Crafting MoC_2-doped bimetallic alloy nanoparticles encapsulated within N-doped graphene as roust bifunctional electrocatalysts for overall water splitting, Nano Energy, 50 (2018) 212-219.
[193] U. Ali, Y. Yu, J. Guo, Y. Liu, Z. Mu, S. Xing, Facile route to achieve Co@Mo_2C encapsulated by N-doped carbon as efficient electrocatalyst for overall water splitting in alkaline media, J. Electrochem. Soc., 167 (2020) 044520.
[194] J.-X. Feng, J.-Q. Wu, Y.-X. Tong, G.-R. Li, Efficient hydrogen evolution on Cu

nanodots-decorated Ni3S2 nanotubes by optimizing atomic hydrogen adsorption and desorption, J. Am. Chem. Soc., 140 (2018) 610-617.
[195] S. Jin, Z. Hao, K. Zhang, Z. Yan, J. Chen, Advances and challenges for the electrochemical reduction of CO_2 to CO: from fundamentals to industrialization, Angewandte Chemie, 133 (2021) 20795-20816.
[196] D.D. Zhu, J.L. Liu, S.Z. Qiao, Recent Advances in Inorganic Heterogeneous Electrocatalysts for Reduction of Carbon Dioxide, Advanced Materials, 28 (2016) 3423-3452.
[197] C. Costentin, M. Robert, J.-M. Savéant, Catalysis of the electrochemical reduction of carbon dioxide, Chemical Society Reviews, 42 (2013) 2423-2436.
[198] Y. Wang, H. Su, Y. He, L. Li, S. Zhu, H. Shen, P. Xie, X. Fu, G. Zhou, C. Feng, Advanced electrocatalysts with single-metal-atom active sites, Chemical reviews, 120 (2020) 12217-12314.
[199] S.-G. Han, D.-D. Ma, Q.-L. Zhu, Atomically Structural Regulations of Carbon-Based Single-Atom Catalysts for Electrochemical CO_2 Reduction, Small Methods, 5 (2021) 2100102.
[200] Y. Wang, Y. Liu, W. Liu, J. Wu, Q. Li, Q. Feng, Z. Chen, X. Xiong, D. Wang, Y. Lei, Regulating the coordination structure of metal single atoms for efficient electrocatalytic CO_2 reduction, Energy & Environmental Science, 13 (2020) 4609-4624.
[201] W. Ni, Z. Liu, Y. Zhang, C. Ma, H. Deng, S. Zhang, S. Wang, Electroreduction of carbon dioxide driven by the intrinsic defects in the carbon plane of a single Fe–N_4 site, Advanced Materials, 33 (2021) 2003238.
[202] X. Wang, Z. Chen, X. Zhao, T. Yao, W. Chen, R. You, C. Zhao, G. Wu, J. Wang, W. Huang, J. Yang, X. Hong, S. Wei, Y. Wu, Y. Li, Regulation of Coordination Number over Single Co Sites: Triggering the Efficient Electroreduction of CO_2, Angewandte Chemie International Edition, 57 (2018) 1944-1948.
[203] J. Chen, Z. Li, X. Wang, X. Sang, S. Zheng, S. Liu, B. Yang, Q. Zhang, L. Lei, L. Dai, Y. Hou, Promoting CO_2 Electroreduction Kinetics on Atomically Dispersed Monovalent Zn^I Sites by Rationally Engineering Proton-Feeding Centers, Angewandte Chemie International Edition, 61 (2022) e202111683.
[204] E. Zhang, T. Wang, K. Yu, J. Liu, W. Chen, A. Li, H. Rong, R. Lin, S. Ji, X. Zheng, Y. Wang, L. Zheng, C. Chen, D. Wang, J. Zhang, Y. Li, Bismuth Single Atoms Resulting from Transformation of Metal–Organic Frameworks and Their Use as Electrocatalysts for CO2 Reduction, J. Am. Chem. Soc., 141 (2019) 16569-16573.

[205] Q. Wang, K. Liu, J. Fu, C. Cai, H. Li, Y. Long, S. Chen, B. Liu, H. Li, W. Li, Atomically dispersed s-block magnesium sites for electroreduction of CO_2 to CO, Angewandte Chemie International Edition, 60 (2021) 25241-25245.
[206] W. Guo, X. Tan, J. Bi, L. Xu, D. Yang, C. Chen, Q. Zhu, J. Ma, A. Tayal, J. Ma, Y. Huang, X. Sun, S. Liu, B. Han, Atomic Indium Catalysts for Switching CO_2 Electroreduction Products from Formate to CO, Journal of the American Chemical Society, 143 (2021) 6877-6885.
[207] Y. Li, C. Chen, R. Cao, Z. Pan, H. He, K. Zhou, Dual-atom Ag_2/graphene catalyst for efficient electroreduction of CO_2 to CO, Applied Catalysis B: Environmental, 268 (2020) 118747.
[208] X. Gu, Y. Jiao, B. Wei, T. Xu, P. Zhai, Y. Wei, J. Zuo, W. Liu, Q. Chen, Z. Yang, F. Zhao, X. Wang, L. Wang, Y. Gong, Boron bridged $NiN_4B_2C_x$ single-atom catalyst for superior electrochemical CO_2 reduction, Materials Today, (2022).
[209] T. Zhang, X. Han, H. Liu, M. Biset-Peiró, J. Li, X. Zhang, P. Tang, B. Yang, L. Zheng, J.R. Morante, Site-Specific Axial Oxygen Coordinated FeN_4 Active Sites for Highly Selective Electroreduction of Carbon Dioxide, Advanced Functional Materials, (2022) 2111446.
[210] Y. Li, B. Wei, M. Zhu, J. Chen, Q. Jiang, B. Yang, Y. Hou, L. Lei, Z. Li, R. Zhang, Y. Lu, Synergistic Effect of Atomically Dispersed Ni–Zn Pair Sites for Enhanced CO_2 Electroreduction, Advanced Materials, 33 (2021) 2102212.
[211] W. Ren, X. Tan, W. Yang, C. Jia, S. Xu, K. Wang, S.C. Smith, C. Zhao, Isolated diatomic Ni-Fe metal–nitrogen sites for synergistic electroreduction of CO_2, Angewandte Chemie International Edition, 58 (2019) 6972-6976.
[212] J. Pei, T. Wang, R. Sui, X. Zhang, D. Zhou, F. Qin, X. Zhao, Q. Liu, W. Yan, J. Dong, L. Zheng, A. Li, J. Mao, W. Zhu, W. Chen, Z. Zhuang, N-Bridged Co–N–Ni: new bimetallic sites for promoting electrochemical CO_2 reduction, Energy & Environmental Science, 14 (2021) 3019-3028.
[213] X. Wang, J. Xie, M.A. Ghausi, J. Lv, Y. Huang, M. Wu, Y. Wang, J. Yao, Rechargeable Zn–CO_2 Electrochemical Cells Mimicking Two-Step Photosynthesis, Advanced Materials, 31 (2019) 1807807.
[214] J. Gu, C.-S. Hsu, L. Bai, H.M. Chen, X. Hu, Atomically dispersed Fe^{3+} sites catalyze efficient CO_2 electroreduction to CO, Science, 364 (2019) 1091-1094.
[215] F. Pan, B. Li, E. Sarnello, S. Hwang, Y. Gang, X. Feng, X. Xiang, N.M. Adli, T. Li, D. Su, Boosting CO_2 reduction on Fe-NC with sulfur incorporation: Synergistic

electronic and structural engineering, Nano Energy, 68 (2020) 104384.
[216] X.-M. Hu, H.H. Hval, E.T. Bjerglund, K.J. Dalgaard, M.R. Madsen, M.-M. Pohl, E. Welter, P. Lamagni, K.B. Buhl, M. Bremholm, Selective CO_2 reduction to CO in water using earth-abundant metal and nitrogen-doped carbon electrocatalysts, ACS catalysis, 8 (2018) 6255-6264.
[217] X. Li, Y. Zeng, C.-W. Tung, Y.-R. Lu, S. Baskaran, S.-F. Hung, S. Wang, C.-Q. Xu, J. Wang, T.-S. Chan, Unveiling the in situ generation of a monovalent Fe (I) site in the single-Fe-atom catalyst for electrochemical CO_2 reduction, ACS Catalysis, 11 (2021) 7292-7301.
[218] J. Chen, T. Wang, X. Wang, B. Yang, X. Sang, S. Zheng, S. Yao, Z. Li, Q. Zhang, L. Lei, Promoting Electrochemical CO_2 Reduction via Boosting Activation of Adsorbed Intermediates on Iron Single-Atom Catalyst, Advanced Functional Materials, 32 (2022) 2110174.
[219] T. Wang, X. Sang, W. Zheng, B. Yang, S. Yao, C. Lei, Z. Li, Q. He, J. Lu, L. Lei, Gas diffusion strategy for inserting atomic iron sites into graphitized carbon supports for unusually high-efficient CO_2 electroreduction and high-performance Zn–CO_2 batteries, Advanced Materials, 32 (2020) 2002430.
[220] X. Sun, Y. Tuo, C. Ye, C. Chen, Q. Lu, G. Li, P. Jiang, S. Chen, P. Zhu, M. Ma, Phosphorus induced electron localization of single iron sites for boosted CO_2 electroreduction reaction, Angewandte Chemie International Edition, 60 (2021) 23614-23618.
[221] Z. Li, R. Wu, S. Xiao, Y. Yang, L. Lai, J.S. Chen, Y. Chen, Axial chlorine coordinated iron-nitrogen-carbon single-atom catalysts for efficient electrochemical CO_2 reduction, Chemical Engineering Journal, 430 (2022) 132882.
[222] C. Wang, X. Hu, X. Hu, X. Liu, Q. Guan, R. Hao, Y. Liu, W. Li, Typical transition metal single-atom catalysts with a metal-pyridine N structure for efficient CO_2 electroreduction, Applied Catalysis B: Environmental, 296 (2021) 120331.
[223] B. Zhang, J. Zhang, F. Zhang, L. Zheng, G. Mo, B. Han, G. Yang, Selenium-doped hierarchically porous carbon nanosheets as an efficient metal-free electrocatalyst for CO_2 reduction, Advanced Functional Materials, 30 (2020) 1906194.